Alexander Gruber, BSc

3D Printing of Functional Nano-Substrates for Surface Enhanced Raman Spectroscopy

MASTER'S THESIS

to achieve the university degree of

Diplom-Ingenieur

Master's degree programme:

Technical Physics

submitted to

Graz University of Technology

Supervisor

Assoc. Prof. Dipl.-Ing. Dr.techn. Harald Plank

Institute of Electron Microscopy and Nanoanalysis

Co-Supervisor

Dipl.-Ing. Dr.techn. Harald Fitzek

Institute of Electron Microscopy and Nanoanalysis

Graz, February 2021

AFFIDAVIT

I declare that I have authored this thesis independently, that I have not used other than the declared sources/resources, and that I have explicitly indicated all material which has been quoted either literally or by content from the sources used. The text document uploaded to TUGRAZonline is identical to the present master's thesis.

Date, Signature

Abstract

Raman spectroscopy is a versatile technique that can be used to determine various material properties from the spectrum and polarisation of scattered light. Surface Enhanced Raman Spectroscopy (**SERS**) is an extension of this technique to improve Raman signals up to a gain of 10^{10} for detecting extremely low material concentrations. That technique, however, requires plasmonically active substrates, which are traditionally produced by sputtering very thin Au layers. Although fast, such methods do not allow site specific fabrication with variable footprint shapes and dimension. To overcome that limitations, we here evaluate the applicability of the additive, direct-write technology Focused Electron Beam Induced Deposition (**FEBID**), which allows highly flexible nanofabrication with spatial nanometer resolution. While powerful in the initial fabrication step, FEBID materials contain very high carbon contents, which prevent plasmonic activities. Hence, post-growth procedures are required, which remove the carbon and produce pure metallic structures.

Based on that motivation, this thesis starts with the controlled fabrication of gold-based nano-pads via FEBID, which reveals several gas dynamic effects with implications on the achievable spatial precision. After solving that problem by parameter and design adaptions, such nanostructures are then subjected to an e-beam assisted etching process in low pressure H_2O atmospheres. Although nominally pure, no plasmonic activities are found, which requires a closer look to the chemistry and morphology of the produced gold nano-pads. A systematic approach reveals two influences. First, surface contamination is identified as a limiting factor, which can be reduced to a certain extend. Optimized structures then reveal a plasmonic activity, however, with more than 2 orders of magnitude lower enhancement factors than sputtered SERS substrates. The second influence seems to be a consequence of the rapid fabrication / purification processes, which are far from a thermodynamic equilibrium. Consequently, an annealing period of 21 days is introduced, which changes the morphology into more agglomerated structures, while the original footprint is widely maintained. More importantly, however, the enhancement factors are strongly increased and finally found in the same range as sputtered reference SERS samples.

Therefore, this master thesis delivers the first proof-of-principle concerning the fabrication of SERS substrates via FEBID, which opens up new possibilities due to the area selective character and its high design flexibility.

Kurzfassung

Die Raman-Spektroskopie ist eine vielseitige Technik, mit welcher verschiedene Materialeigenschaften aus dem Spektrum und der Polarisation von Streulicht bestimmt werden können. Die oberflächenverstärkte Raman-Spektroskopie (engl. Surface Enhanced Raman Spectroscopy; **SERS**) ist eine technische Erweiterung, welche Raman-Signale bis zu einem Faktor 10^{10} verstärken können, um extrem geringe Materialkonzentrationen nachzuweisen. Diese Technik erfordert jedoch plasmonisch aktive Substrate, die typischerweise durch Sputtern sehr dünner Au-Schichten hergestellt werden. Obwohl diese Methoden schnell sind, ermöglichen sie keine ortsspezifische Herstellung mit variablen Grundflächen-Formen und -Abmessungen. Um diese Einschränkungen zu überwinden, evaluieren wir hier die Anwendbarkeit der additiven Direktschreibtechnologie Focused Electron Beam Induced Deposition (engl. Focused Electron Beam Induced Deposition; **FEBID**), die eine hochflexible Nanofabrikation mit räumlicher Nanometerauflösung ermöglicht. Obwohl leistungsstark im ersten Herstellungsschritt, weisen FEBID Materialien jedoch sehr hohe Kohlenstoffgehalte auf, welche plasmonische Aktivitäten verhindern. Daher sind Verfahren nach dem Wachstum erforderlich, bei denen der Kohlenstoff entfernt und reine Metallstrukturen erzeugt werden.
Basierend auf dieser Motivation beginnt diese Arbeit mit der kontrollierten Herstellung von Nano-Pads auf Goldbasis mittels FEBID, welche verschiedene gasdynamische Effekte mit Auswirkungen auf die erreichbare räumliche Präzision aufzeigt. Nachdem dieses Problem durch Parameter- und Designanpassungen gelöst wird, werden derartige Nanostrukturen einem elektronenstrahlunterstützten Ätzprozess in H_2O-Niederdruckatmosphären unterzogen. Obwohl nominell rein, werden dennoch keine plasmonischen Aktivitäten gefunden, was eine genauere Untersuchung der Chemie und Morphologie der hergestellten Gold-Nano-Pads erfordert. Ein systematischer Ansatz zeigt zwei Einflüsse. Zunächst wird die Oberflächenverunreinigung als begrenzender Faktor identifiziert, welcher bis zu einem gewissen Grad reduziert werden kann. Optimierte Strukturen zeigen dann eine plasmonische Aktivität, jedoch mit mehr als 2 Größenordnungen niedrigeren Verstärkungsfaktoren als gesputterte SERS-Substrate. Der zweite Einfluss scheint eine Folge der schnellen Herstellungs- / Reinigungsprozesse zu sein, die weit von einem thermodynamischen Gleichgewicht entfernt sind. Infolgedessen wird eine Ruhezeit von 21 Tagen eingeführt, welche die Morphologie in stärker agglomerierten Strukturen verwandelt, während die ursprüngliche Grundform weitgehend beibehalten wird. Noch wichtiger ist jedoch, dass die Verstärkungsfaktoren nun stark erhöht sind und sich schließlich im gleichen Bereich wie gesputterte Referenz-SERS-Proben befinden.
Daher liefert diese Masterarbeit den ersten Proof-of-Principle zur Herstellung von SERS-Substraten über FEBID, der aufgrund des bereichsselektiven Charakters und seiner hohen Gestaltungsflexibilität neue Möglichkeiten eröffnet.

Acknowledgements

I would like to thank all those who have supported me directly and indirectly in this Master's thesis. First of all, I would like to thank Dr. Gerald Kothleitner, who made this Master's thesis possible for me as the head of the institute. I would also like to thank Dr. Ferdinand Hofer, who was the head of the institute when I started this work.

My very special thanks go to Dr. Harald Plank, who was the supervisor for this project and always supported me in word and deed, the experiences he passed on to me and kept an open ear for problems of any kind.

I would especially like to thank my co-supervisor Dr. Harald Fitzek, who worked with me on the experimental questions and was always able to help me solve a variety of problems.

Furthermore, I would like to thank Dr. Robert Winkler, Dr. David Kuhness, DI Lukas Seewald and DI Anna Weitzer for their advice and cooperation.

My thanks also go to Ing. Sebastian Rauch who took over the plasma cleaning of the samples.

I would also like to thank my thesis colleagues with whom I have had many exciting discussions and my friends who have provided support and a sense of unity, especially during the COVID-19 pandemic, and an end to isolation without which this thesis could not have been completed.

Finally, I would like to thank my whole family for their continued support and trust. Especially my parents Günter and Ulrike and my grandfather Hubert.

Table of Contents

1 Motivation

Raman spectroscopy has immense potential for a wide range of complex problems to be solved. Raman and the complementary method Fourier-transform infrared spectroscopy (**FTIR**), both belong to the molecular spectroscopic methods. They are both based on molecular vibrations, while Raman spectroscopy relies on the polarizability of the electron shells of molecules, FTIR uses the dipole moment of the same. In Raman, the sample is irradiated with laser light and the scattered light is detected, whereas in FTIR a sample is recorded by passing a beam of infrared light through the sample. Raman can be used to study a wide range of organic and inorganic materials, both solid and liquid. At the same time, sample preparation and handling are very simple and time-saving, as even analysis through glass or polymer sample containers is manageable.[1]

It is possible to obtain a spectrum within seconds that corresponds to the chemical fingerprint of the material under investigation and at the same time is non-destructive (multiple measurements possible) and can even be used as a probe via optical fibres as a remote application. This technique provides characteristic fundamental vibrations that are commonly used to determine and classify the molecular structure.[2] From the spectrum (frequency and the corresponding intensity) and the polarisation of the scattered light, various material properties such as crystallinity, crystal orientation, etc. can be determined. Since the Raman scattering has a very small scattering cross-section (approx. 10^{-30} cm²),[3] we need a relatively high concentration of molecules and a high laser intensity to get a detectable signal and of course it is not possible to detect and study single molecules by straightforward application.

Fittingly, there is a solution called surface-enhanced Raman spectroscopy (**SERS**) which critically enhance Raman signals from molecules, adsorbed on rough metal surfaces or defined nanostructures. That approach revealed the potential to eliminate the conflict between novel insights (wanted) and complicated detection (unwanted), leveraging Raman-spectroscopy / -microscopy into an essential characterization technology. In the last few years, FELMI-ZFE has increased its efforts in the development, characterisation and theoretical modelling of intelligent substrates for SERS. These substrates can only be manufactured with plasmonically active materials (Au, Ag) and have so far been produced via e.g. low volume (sputter) coating. That leads to a stochastic distribution of nano-island orientation, -size and shape, enabling a “self-selection” of ideal properties for the subsequently dispensed analyte of interest (see a) in Figure 1). These substrates locally intensify the electric field due to the plasmonic excitation and lead to enhancement factors of up to 10^{10} in ideal cases.[4]

That concepts work well, as long as large area substrates can be used, e.g. for classical Raman applications. However, when a small number of SERS elements should be site-specifically integrated in more complex, multifunctional layouts or even in small devices, the stochastic character prevents predictable and reproducible fabrication of high-performance structures. To overcome that limitation, a method is needed, which allows the controlled fabrication of functional nanostructures on almost any material and surface morphology.

Such a technology is available and intensively used at FELMI-ZFE for more than a decade, namely: Focused Electron Beam Induced Deposition (**FEBID**). This technique uses a nanosized electron beam, which locally decomposes surface adsorbed precursor molecules and enables the fabrication of structures in the sub-15 nm regime.[5] However, most FEBID materials notoriously suffer from very high carbon contents after deposition, which for gold precursor can amount up to 95 at.%, making plasmonic applications impossible.[6] In 2014, Geier et al.[7] introduced a purification approach, which produced pure metallic materials with very high efficiencies and minimal impact on the original morphology.

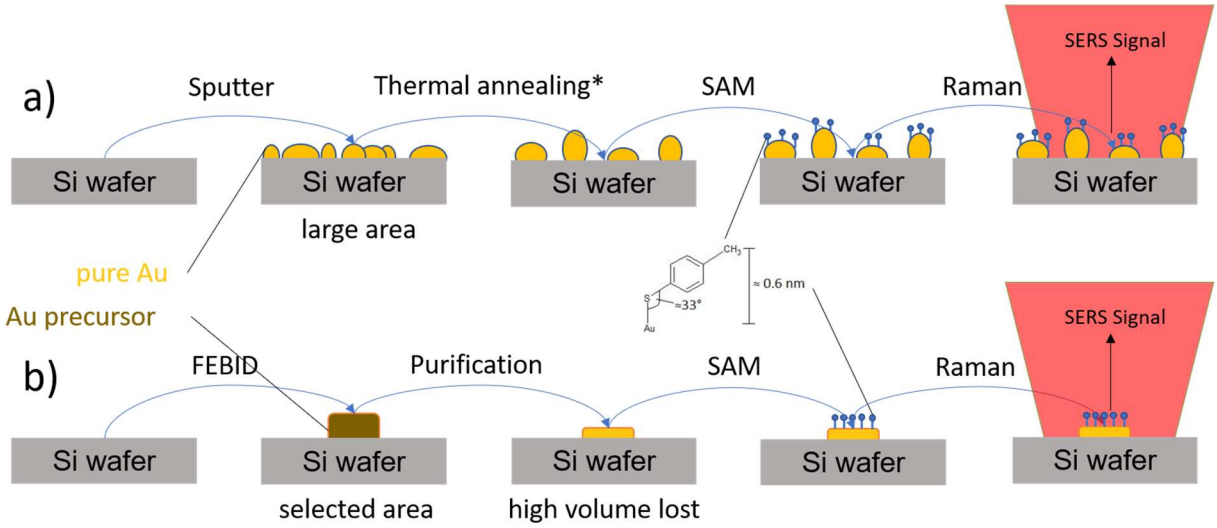

*Figure 1: Schematic procedure for the production of a plasmonically active substrate for SERS by the classical fabrication route (**a**) and via FEBID (**b**). While the former process leads to chemically pure materials, structural dimensions, orientations and distributions are stochastic. FEBID, in contrast, allows controlled fabrication, while the materials require post-growth purification to eliminate carbon impurities, which reduce or even mask the intended plasmonic functionality. *Please note that thermal annealing was not used during this thesis and so after sputtering, the SAMs were applied directly, followed by the Raman measurement.*

Shortly after, Winkler et al.[6] Demonstrated the applicability of the same approach to gold-based FEBID materials and fulfilled the long-lasting promise of plasmonic applications for FEBID based nano-structures. The purpose of this master thesis now brings together both ends and focuses on the controlled FEBID fabrication of gold nanostructures, acting as SERS substrates after our purification routines. In more detail, we evaluate FEBID-related SERS performances, compare them to traditionally prepared gold sputter substrates and identify performance reducing factors (see b) in Figure 1). Hence, this master thesis must be understood as the foundation for further research and development concerning the controlled FEBID fabrication of SERS structures on almost any material and surface morphology.

2 Instrumentation and Basics

2.1 Dual Beam Microscope

A dual beam microscope (**DBM**) combines a focused ion beam (**FIB**) system and a scanning electron microscope (**SEM**) into a single instrument. Although the FIB is mainly used for sample preparation, such as transmission electron microscope (**TEM**) lamellae, it can also be used for imaging, subtractive (nano)fabrication or surface modification, when combined with dedicated gas injection systems. The idea behind DBMs is to avoid using several, separate devices for inspection, characterization, modification and preparation.[8] While Figure 2 shows two different DBMs used for this study, Figure 3 gives an inside look of a DBM to understand the technical setup. The electron column is installed vertically, while the ion column is tilted 52° to allow for simultaneous operation in the eucentric height, where both beams cross. Many other devices can be connected to this system, but especially the gas injection system (**GIS**) and the micromanipulator are worth mentioning.[8] The GIS system can be used in combination with SEM and FIB for advanced deposition of materials in complicated geometries. When used with the electron column, it is called focused electron beam induced deposition (FEBID) and when combined with ions, it is called focused ion beam induced deposition (**FIBID**).
As can also be seen in Figure 2, several detectors are attached to the DBMs. These all differ in their operation, as they are designed to pick up different signals from the interaction of particles with the sample. Probably the most important detector, as there is hardly an electron microscope without it, is the Everhart-Thornley detector (**ETD**). This is a combined secondary/backscattered electron detector that operates under a large solid angle of collection, high signal amplification and low noise. This takes advantage of the fact that an electron with a certain energy from the sample hits a scintillator material of the detector and thereby triggers photons. The photons are guided through a light guide to a photomultiplier. At the first cathode of the multiplier, the photons are converted back into electrons and then accelerated several times in a cascade until they reach the final collector. Due to the amplification, a usable signal can be measured. In order to capture low-energy secondary electrons (**SE**) with a higher geometric effectivity, the scintillator is surrounded by a Faraday cage, which has an adjustable potential from -50 V to +250 V. At negative potential, low-energy electrons can be repelled from the detector and only backscattered electrons (**BSE**) can be detected, or at positive potential a mixture of both. SEs that do not have a direct line of sight to the ETD are detected with lower yield and appear as darker areas in the image, resulting in a familiar spatial representation. The interaction of electrons with the atoms of the sample also produces X-rays, which can be detected by an energy dispersive X-ray detector (**EDX**). This is a spectroscopic technique used for elemental analysis or chemical characterisation of a sample.[9] To detect secondary electrons or ions triggered by ion bombardment of the sample, the continuous dynode electron multiplier (**CDEM**) is used. It is located near the end of the ion column.[10] Even though the **AFSEM®**[11] is not a particle detector, it is used for imaging to obtain information about the topology of the sample surface by means of atomic force microscopy during an *in situ* SEM or DBM investigation. In this way, SEM and AFM images of a sample can be obtained simultaneously.[11]

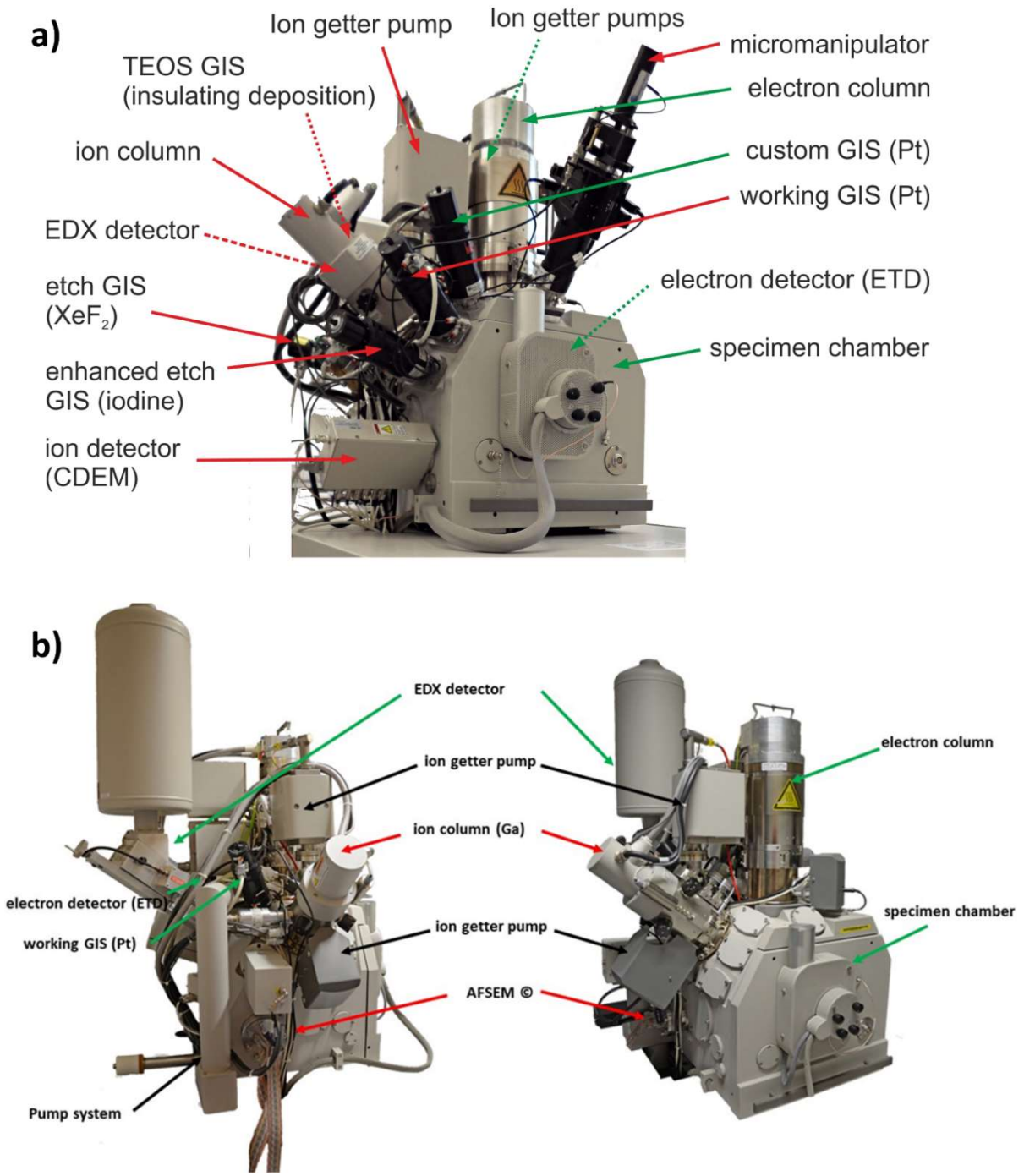

Figure 2: Dual Beam Microscopes at FELMI-ZFE with were used during this thesis. ***a)*** *DBM Nova 200 (FEI, The Netherlands).* ***b)*** *DBM Quanta 3D (FEI, The Netherlands). The coloured arrows mark important components for FEBID and TEM sample preparation.*[12]

As mentioned above, positioning the sample in the eucentric position is of high relevance as the entire system is optimized for operation in that specific spatial position to provide highest possible performance during inspection, characterization, preparation, fabrication and modification. Further information on the important properties of an SEM, such as the possible electron sources, the electron lenses, the detectors and the interaction of electrons with matter, which are important for imaging, can be found in Goldstein and Newbury.[9] A short summary which also provides a good overview of the essential components can be found at Winkler.[13]

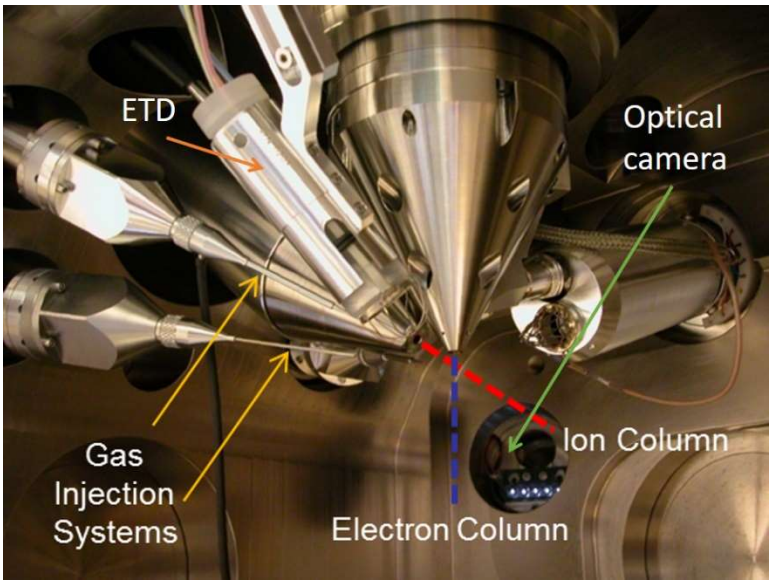

Figure 3: A look inside a Dual Beam Microscope (DBM) with coloured markings showing important components. ***Blue dashed line****: Simplified trajectory of the electrons after they leave the electron column.* ***Red dashed line****: Simplified trajectory of the Ga ions after they leave the ion column.* ***Orange arrow****: Everhardt-Thorley detector (ETD) for electron capture.* ***Yellow arrows****: Gas injection systems (GIS) for injecting different precursor species into the chamber.* ***Green arrow****: optical camera with low magnification for overall spatial orientation.*[12]

2.1.1 Focused Electron Beam Induced Deposition – FEBID

2.1.1.1 Basic Concept

FEBID is a direct-writing technique, which allows feature sizes down to the sub-20 nm regime. In this process, precursor molecules are brought very close to the sample surface by a GIS system and adsorb there. The gas diffuses on the surface and desorb again after a certain residence time. However, if the precursor gas is hit by electrons before it leaves, it dissociates into volatile and non-volatile components. The volatile components are extracted by the vacuum pumps, while the non-volatile components form the actual deposit, as shown in Figure 4.[14]

The parameters that determine the properties or quality of a deposition are the acceleration voltage of the primary electrons and the electron current, the dwell time (**DT**), the point pitch (**PoP**), the number of repetitions of the writing process (passes), the replenishment time (**RT**) and the path or strategy on which the electron beam is guided over the sample surface as explained in more detail in the following.[14]

2.1.1.2 Electron-Induced Dissociation

As already mentioned, the dissociation of the precursor molecule is based on the interaction with electrons. However, there is not one process but a series of electron-molecule interactions. The probability of precursor gas decomposition depends on the dissociation cross section, which is related to the incident electron energy. Most precursors need only a few eV to be split and this range (< 50 eV) is dominated by SE. In this context, there are two dissociations processes that are worth mentioning. One is dissociative electron attachment (**DEA**) and the other is dissociation ionization (**DI**). The energy range for DEA is between 2 and

7 eV, while DI requires values greater than 10 eV. Since the maximum SE yield is at 3 eV, DEA is the dominant process in dissociation. However, DEA usually leads to incomplete dissociation, which results in a high number of non-metallic contaminants in the deposition. The primary electrons (**PE**) hardly participate in the dissociation, because their cross section is much too small.[14,15]

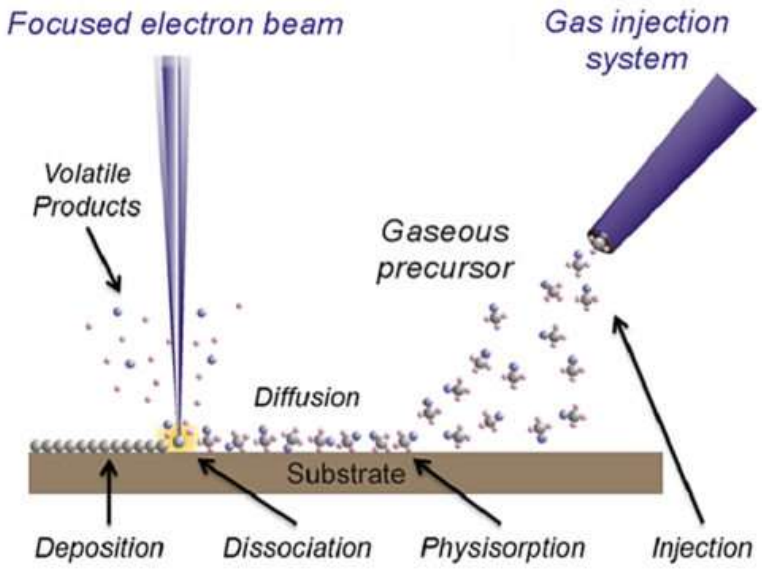

Figure 4: Working scheme of the FEBID process. The precursor reaches the sample surface through the GIS and is broken down into volatile and non-volatile parts by electrons, the latter forming the deposit.[12]

2.1.1.3 Gas Injection System – GIS

At the DBM Nova 200 multiple gas injection systems are mounted to insert various precursor gases (Au, Pt, SiO_2, Co_3Fe). In each of them, a small reservoir of solid or liquid (SiO_2) precursor material is heated up to its boiling point and when the gas valve is opened, the molecules will stream out through a nozzle. Since the vapor pressure of the precursor can be controlled by the reservoir temperature, it is important to heat both GIS for about 30 minutes before deposition and during deposition to ensure reliable operation. The GIS used here is tilted by 52° with respect to the sample surface and has a nozzle in straight tube design. A pre-calibrated pneumatic system brings the nozzle close to the substrate surface to maximize local flux for highest surface coverage. For samples brought to the eucentric height, the lower part of the nozzle is approx. 430 µm above the sample surface, while the front nozzle parts are at a radial distance of approx. 180 µm from the deposition area. To allow the electron beam to run towards the nozzle during deposition of the patterning profile, the scan rotation of the beam must be rotated by 32°. This also ensures that the Y component of the patterning profile is parallel with the projection of the main GIS axis.[13]

2.1.1.4 Precursor Molecules

Meanwhile, there is a broad chemical variety of FEBID precursor to address a comparable wide range of applications from electrically conducting to insulating, magnetic, optical active and even superconductivity. In most cases, the element of interest is bonded to organic groups,

giving most precursor a metal-organic compound character.[16] Typically, those compounds are volatile at temperatures well below 100 °C in high-vacuum conditions, however, at different evaporation rates. Once, the thermodynamic equilibrium is established in the reservoir, the valve releases the gaseous precursor, which adsorb on, diffuse along and desorb from the sample surface. The interaction with the electron beam and its subsequent processes can now induce a chemical fragmentation into volatile and non-volatile components. While non-volatile parts with the target element form the intended deposit, the volatile parts are pumped away by the vacuum system. Since the material contains large amounts of carbon and other substances and the dissociation is not always complete, the resulting deposit is a matrix of carbon with the desired element in between. Depending on the final application, the deposits have to be further processed before they exploit their full potential, such as highly pure metal-structures for plasmonic applications.[16]

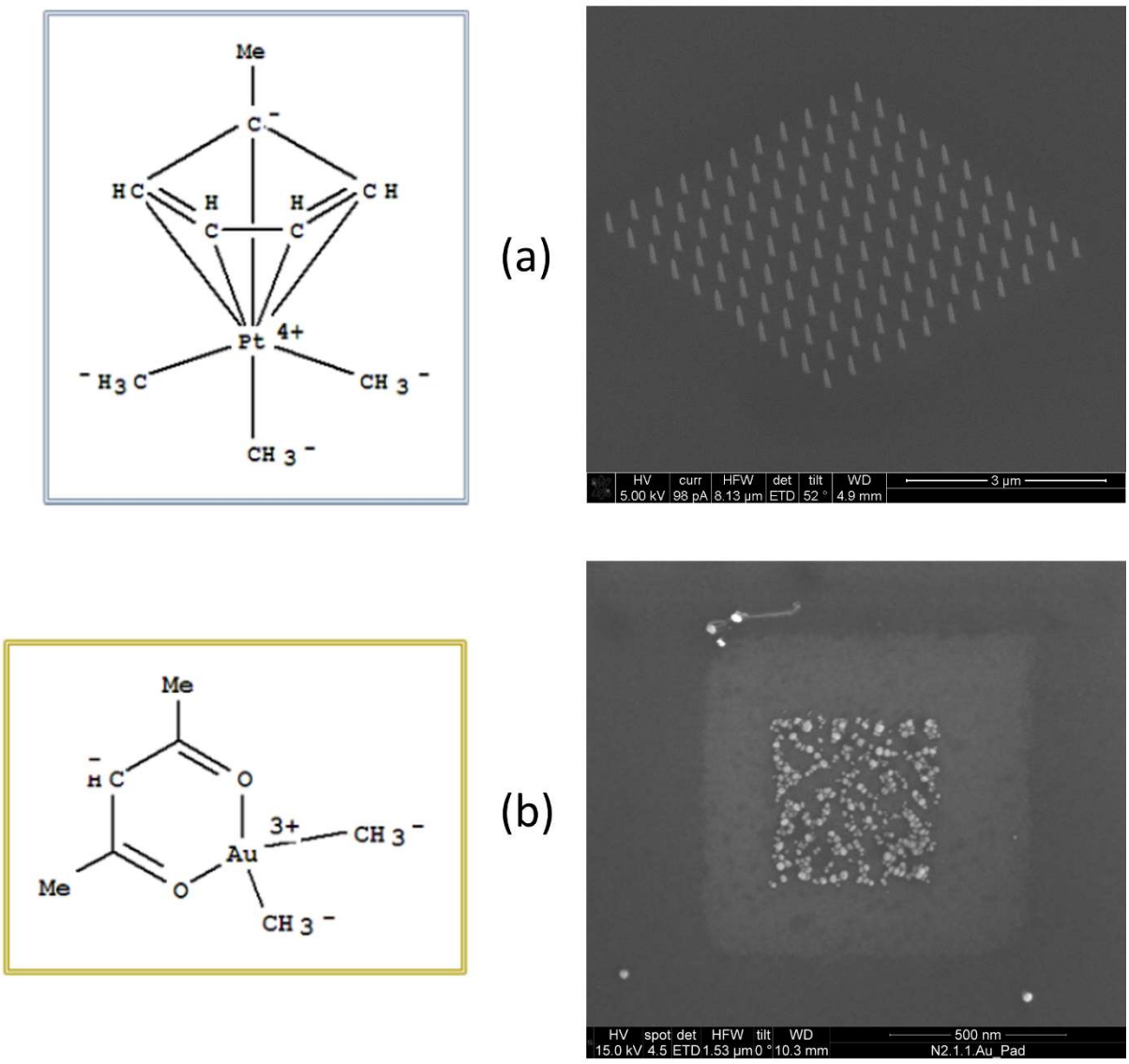

Figure 5: Structural formulae and SEM images of corresponding deposits. ***(a)*** *Structural formula of MeCpPt^{IV}Me$_3$ (left)[17] and an SEM image of a pillar array (right) made from the platinum precursor to optimise the electron beam.* ***(b)*** *Structural formula of Me$_2$-Au(acac) (left)[17] and an SEM image of a plasmonically active pad made from the gold precursor. Please note that the upper SEM image shows pillars directly after deposition, while in the lower image the gold pad has already been purified and has undergone 10 weeks of sample resting in a desiccator.*

For this master's thesis, two precursors were used, namely $MeCpPt^{IV}Me_3$ (trimethyl(methylcyclopentadienyl)-platinum(IV))[17] as platinum precursor for the sharpening field, which is used to optimise the electron beam and Me_2-Au(acac) (dimethylgold^{III} acetylacetonate)[17] as gold precursor for the actual structures of interest.

2.1.1.5 Working Regime

A key aspect of FEBID that must be considered in any deposition is the working regime. It establishes a link between the electrons involved in dissociation and the available precursor molecule and can be adjusted by the process parameters (beam current, dwell time (DT)). In addition to the process parameters, Winkler et al.[18] showed that there are local lateral precursor gas gradients that have strong implications on the morphology of the depositions. These include: gas flux replenishment (**GFR**), surface diffusion replenishment from the deposit (**SDR-D)** and surface replenishment from the surrounding substrate (**SDR-S**). These values can now be assigned to three areas of the working regime, namely the reaction rate limited (**RRL**) regime, the mass transport limited (**MTL**) regime and the diffusion enhanced regime (**DER**), which is difficult to control.[13]

- In the RRL regime, so for very short DTs (which is equivalent to a short refresh time) and low beam currents, there is a certain degree of local precursor depletion after the first patterning loop. Although GFR is constant, the surface diffusion (SDR-D and SDR-S) is different for each patterning point (pixel). For edge points and especially for corner points, the SDR-S component is stronger than the SDR-D components. Points within the pattern can mainly be replenished by GFR and SDR-D components. This dynamic results in increased volumetric growth rates at the edges and corners, leading to a concave ("bowl") shape of the FEBID deposition.[18]
- In the MTL regime, meaning for very high DTs and beam currents, deposition conditions lead to slanted morphologies. Thus, there is a strong localised depletion of precursor gas while at the same time a large number of dissociation electrons are available. In contrast to RRL conditions, the growth is mainly determined by GFR and SDR-D, which leads to a weaker growth rate.[18]
- In the last regime, the DER regime, which actually lies between RRL and MTL in terms of parameters, the observable morphologies are related to short-medium DTs and medium-high beam currents. In this difficult-to-control range, the strength of the contribution of the SDR-S component or the GFR and SDR-D components determines the morphology of the deposits. In particular, for the serpentine patterning strategy, this means a transition from concave shapes to tunnel shapes.[18]

2.1.2 Purification

There are several methods to remove carbon from FEBID structures after deposition to obtain a pure metal complex. Many of these approaches are difficult to establish (e.g. pure hydrogen beam assisted purification) or involve partial destruction of the structures (e.g. oxygen beam assisted purification at elevated temperatures).[16] Geier et al.[19] showed that there is a simple postgrowth purification for the platin precursor $MeCpPt^{IV}Me_3$ where the process takes place at room temperature and H_2O atmosphere at pressures between 10 and 100 Pa. To ensure the necessary prerequisites such as spatially homogeneous pressure distribution, an environmental scanning electron microscope (**ESEM**) is required.[19] In the course of this

master's thesis, the DBM Quanta 3D (FEI, The Netherlands) was taken (Figure 2), which has a low vacuum mode that can be used for purification too. Further information on ESEM can be found at Goldstein and Newbury.[9]
In some ways, electron assisted purification with H_2O atmosphere is similar to the dissociation of gaseous precursor material. In the process, already dissociated or non-dissociated water molecules diffuse into the extremely carbon-rich structures. This diffusion process is only made possible by the high carbon content in depositions and the prevailing room temperature makes this process even more efficient, which is a great advantage of not needing any additional equipment, like a cooling stage. Here, too, the energy of electrons is used to supply the activation energy necessary to generate volatiles (CH_4 and CO)[20] from the carbon in the structure and H_2O, which are then pumped out and leave behind a pure metallic structure. In parallel, *in situ* EDX measurements can be carried out to determine qualitative saturation points. Whereas ex-situ measurements give the proportion of carbon remaining in the structures. Investigations using atomic force microscope (**AFM**) showed that the volume loss for fully purified FEBID structures, with respect to deposition regime, is about 70 vol.%. The great advantage of this purification technique lies in its straight forward approach. The samples do not require any complex preparation, no highly reactive gases are used and even room temperature is sufficient for efficient purification. This process can be carried out in any SEM/DBM with low vacuum or ESEM mode. As for the structures, they remain pore- and crack-free after purification and the original shape is preserved.[7]

In 2016, Winkler et al.[6] showed that this purification approach can also be applied to other precursors, namely the organometallic precursor $Me_2Au(acac)$, which has a carbon content of 95 at. %. The deposited AuC FEBID structures were purified in an ESEM at 10 Pa and H_2O atmosphere at room temperature. The subsequent investigations using AFM, SEM, EDX, TEM and electron energy loss spectroscopy (**EELS**) showed that the structures were completely free of carbon and had a pore and crack free morphology after purification.[6]

Another, though indirect, way to determine the carbon-free state of the structures is AFM, as mentioned before. For this, it must be known at which working regime the deposition took place and how high the corresponding volume loss of the structures must be after purification. This method and the gold precursor $Me_2Au(acac)$ were used in this master thesis.

Although both studies have shown that electron assisted purification with H_2O atmosphere at room temperature is an easily adaptable process that can be applied to different precursors, there are also disadvantages. In this thesis, it is shown that the simultaneous purification of whole arrays in which the individual structures have different vertical sizes results in partial purification, fully purification and over purification of individual structures (section 4.3.1). Furthermore, it will be demonstrated that even if the structures were fully purified, carbon is deposited on the surface (section 4.3.3). Neither of these effects can be considered advantageous with regard to the plasmonic application of FEBID structures.

2.2 Atomic Force Microscope - AFM

An atomic force microscope (AFM), shown in Figure 6, is an instrument for a scanning probe technique, which can be used to form an image of the three-dimensional shape (topography) of a sample surface at a very high resolution on both dry and wet sample surfaces. During the measurement, a nanoscopic needle at the end of a silicon beam (cantilever) is guided in a serpentine-like fashion over the sample surface (scanning). In its most simple mode, the Contact Mode, surface topology leads to small bending of the cantilever, which can be detected

via electric, capacitive or, like in our case, optical sensors. That deviations, caused by atomic forces between tip and surface, act as input, followed by a controlled vertical movement of the scanner unless the original bending situation is restored. The vertical scanner position (Z) is then linked to each XY point, giving a 3-dimensional picture of the surface.

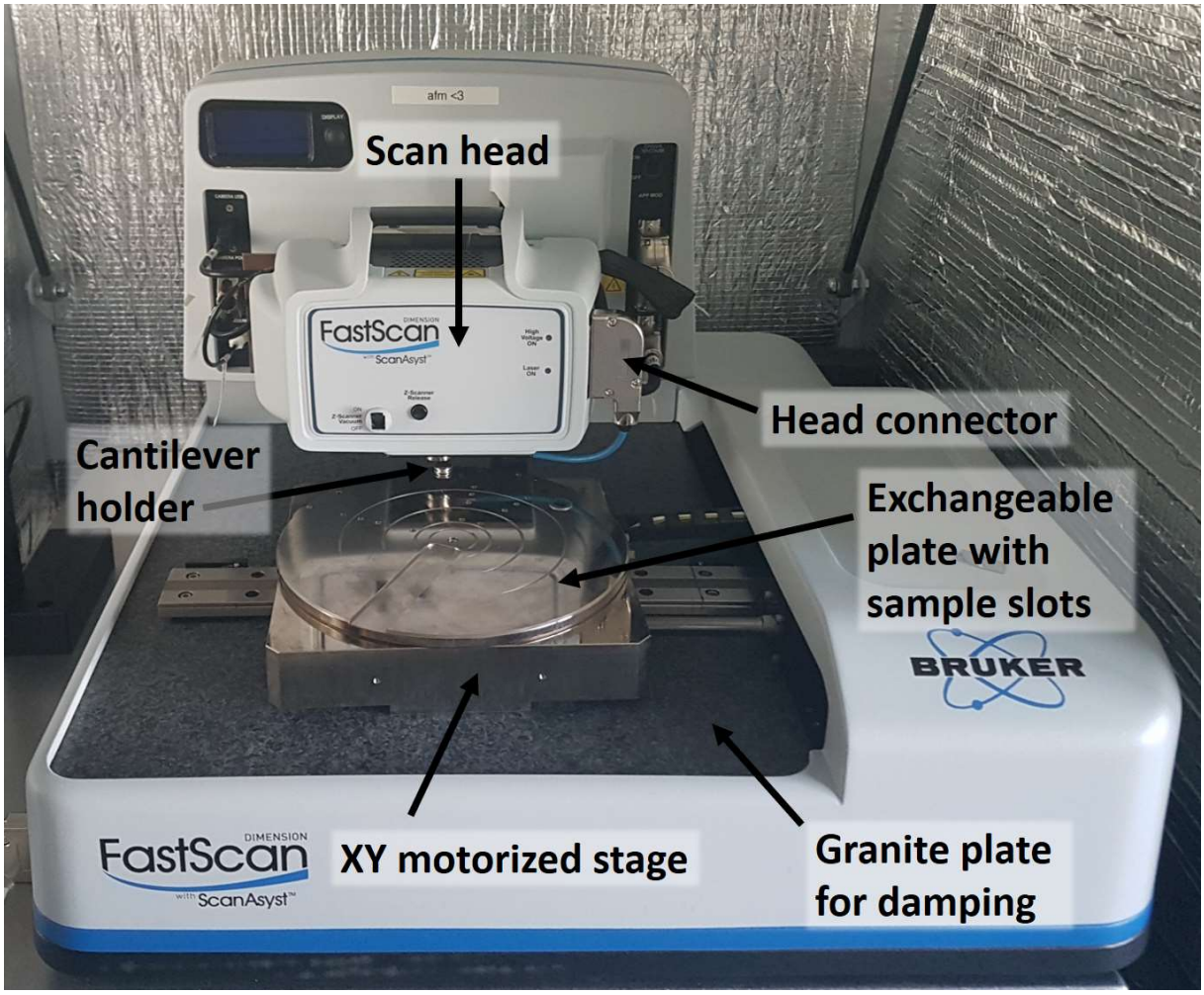

Figure 6: Brucker Fast Scan Bio AFM at FELMI-ZFE. Some of the important parts of the instrument are marked with black arrows. Samples are mounted on the exchangeable plate which is located on a stage that can be moved in XY-direction and allows the sample to be positioned below the scan head. The granite plate underneath is quite heavy and should prevent oscillations. On the bottom of the scan head is the holder for the cantilever with the measuring tip on it and the head connector forms the interface between the scan head and the cantilever holder. The scan head contains, among other things, a vacuum system for the cantilever holder and the optical sensors. The unit shown in the photo is also surrounded by an acoustic and vibration-insulating enclosure.

In Tapping Mode (sometimes Intermittent Mode), the tip is oscillated at the cantilevers resonance frequency with a pre-set amplitude. The tip experiences cyclic forces according to the Lennard-Jones potential ranging from attractive (van der Waals) to repulsive (Pauli principle). Depending on the dominating force, a new coupled resonance frequency establishes, leading to an amplitude decay as the excitation frequency is permanently kept constant. This amplitude decay now acts as input signal, similar to the deflection in Contact Mode, followed by a fast re-adaption of the vertical Z position of the scanner. As Tapping Mode acts like a damped, forced oscillator, a phase lag between excitation and detection occurs,

which carries information about the dominating interaction forces. Both together, amplitude and phase information, allows precise control during AFM scanning, leading to much more gentle scanning than for Contact Mode.[21] Further information on the working principle of all components can be found either in this literature[22] from early days of AFM or in modern form at Garcia.[21]

2.3 Raman Microscope

The Raman measurements during this master thesis were all performed with the LabRAM HR 800 from Horiba, see Figure 7. This is a confocal Raman microscope which basically consists of the following important parts: Laser (632 nm HeNe 20 mW laser by default but can be extended with additional others), Microscope BX 40, 800 mm focal length Spectrograph, a Peltier cooled CCD detector and a computer with the LabSpec6 software for control and acquisition / analysis.[23]

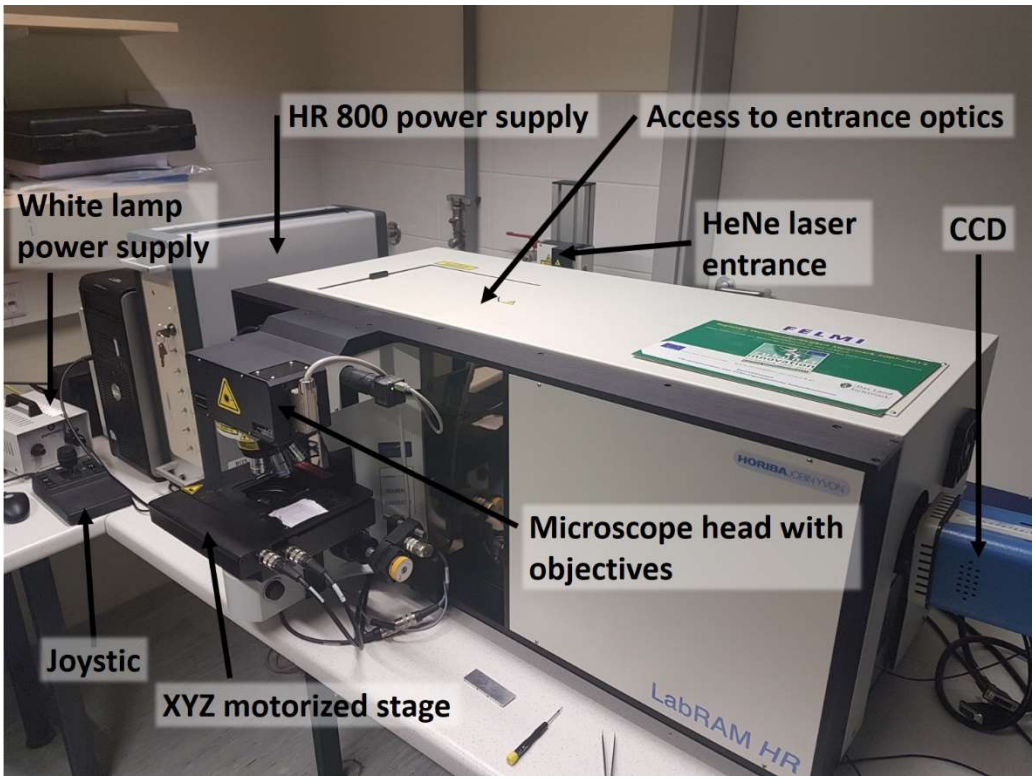

Figure 7: Jobin Yvon LabRam 800HR Raman microscope at FELMI-ZFE. The important parts are marked by black arrows.

So, a Raman microscope consists of an ordinary optical microscope and a Raman spectrometer, which allows a high magnification of the samples and an additional analysis via Raman spectroscopy. However, in order to obtain high spatial resolution (x-,y-,z-direction), confocal Raman spectroscopy is necessary.[24] This is achieved by a pinhole aperture, which controls the degree of confocality, in front of the Raman spectrograph entrance slit, and the slit itself, which limits the spectral resolution.[25] A schematic of a Raman spectrograph and the optical pathway of the HR 800 can be seen in Figure 8.

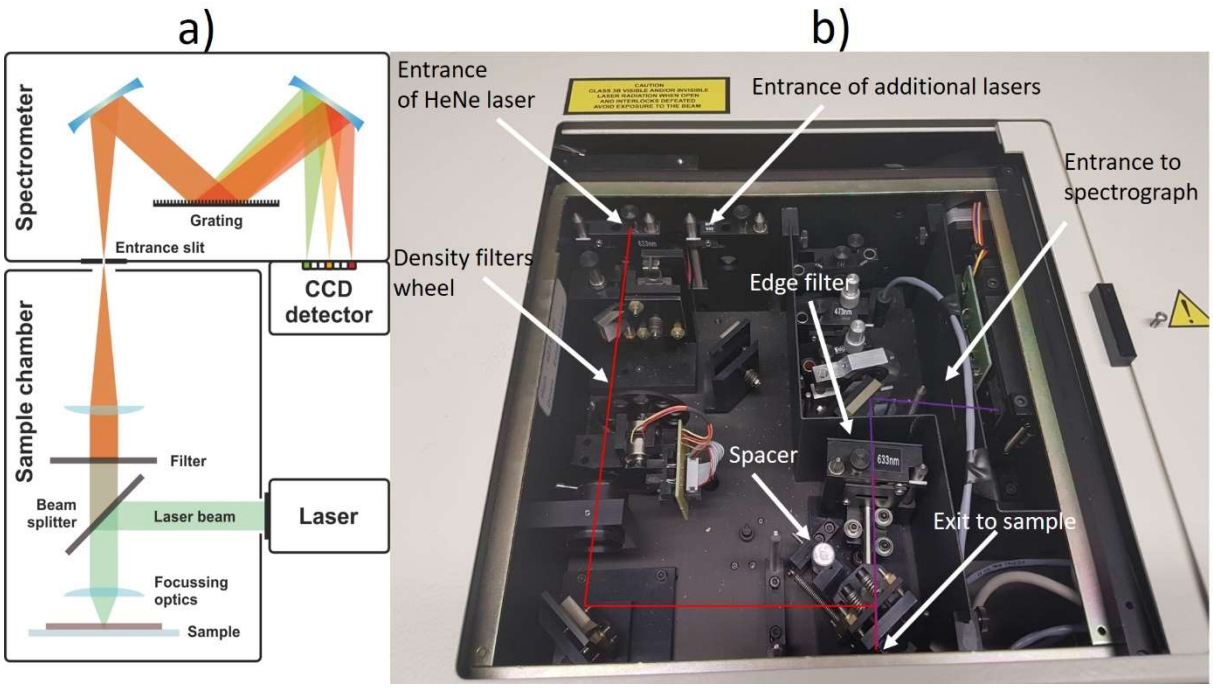

Figure 8: ***a)*** *Schematic of the functioning of a Raman spectrograph.*[26] ***b)*** *Optical pathway of Jobin Yvon LabRam 800HR Raman microscope: laser beam (red path), Raman beam (violet path).*

To get an image of the sample, either the sample itself or the laser can be moved from point to point, which is of course much more complicated than a conventional microscope. The advantage, however, is that only detected light from a small area of the focal point is measured, which means that scattered light above or below it does not contribute to the image. This means that the sample is not illuminated homogeneously in an extended field of view, but a Gaussian laser beam is tightly focused by a microscope objective on a diffraction-limited spot on the sample. The same objective collects and collimates scattered or emitted light coming from this point on the sample and is then focused through a small pinhole onto a detector.[1]

2.3.1 Raman Spectroscopy

Raman spectroscopy is based on the effect of light scattering and is described by electromagnetic waves which are excited by oscillating dipoles in the molecules induced by external radiation (e.g. IR or visible light). Therefore, it only works where the polarizability *α,* which corresponds to the deformability by external forces, of the electron shell of the molecules is changeable during the movement. The resulting dipole moment is a non-resonant exchange supported by an external oscillating electric field.[2]
The wavelength range of the detected Raman scattered light always depends on the incident laser used and will therefore also be either visible or invisible. In both cases, however, several processes are running simultaneously in which the scattered light loses no energy (Rayleigh) or gives off / receives a certain amount of energy (Raman) for the excitation / relaxation of the molecular vibration. Either way, it is a two-photon process in which the incident light is absorbed from the ground state into a "virtual" state and a new photon is re-emitted from that state.[2]

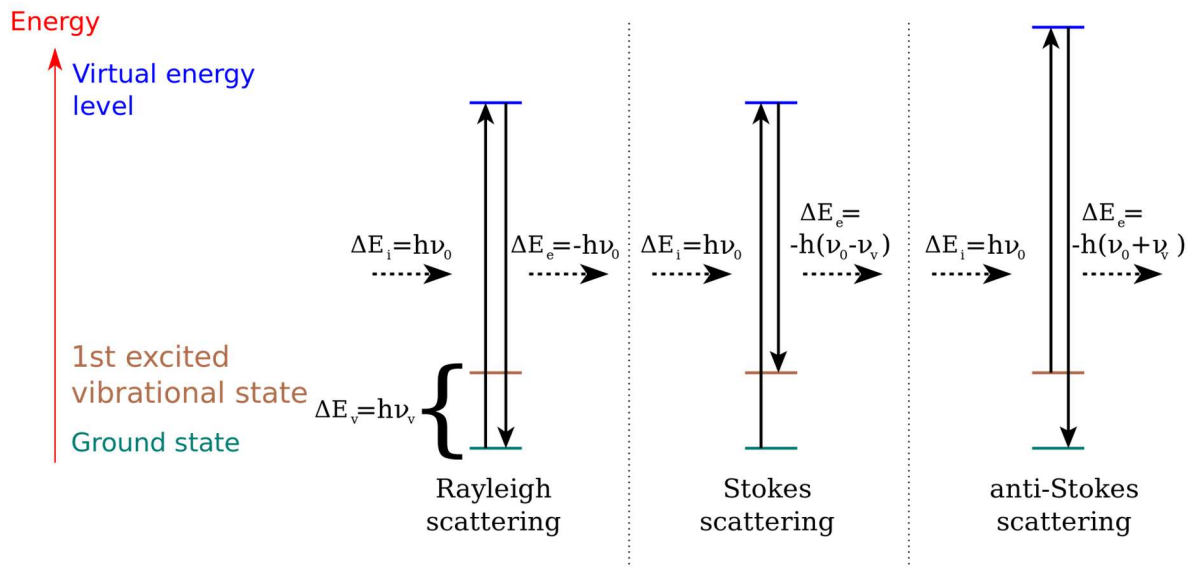

Figure 9: Three different possibilities that occur during Raman spectroscopy: Rayleigh scattering. Stokes scattering, anti-Stokes scattering.[27]

The three possibilities are described in Figure 9 and the following:[2,28]

- Rayleigh scattering: This is elastic scattering of light by molecules and is the dominant process. The intensity is 10^{-3} less than that of the incident beam. The energy, also the wavelength, remains the same and the Rayleigh scattered light must be removed from the spectrum, as it would otherwise overlap the Raman light.

- Stokes Raman scattering: An inelastic scattering process in which the energy of the light is transferred to excite the molecular vibration. The intensity is 10^{-6} less than for incident light and the amount of energy transferred to the molecule cannot be arbitrary but is exactly the energy needed to excite the vibration. The spectrum obtained from the scattered light therefore depends very much on the molecule and corresponds to a "molecular fingerprint". So, this is the most important process for us.

- Anti-Stokes Raman scattering: Also an inelastic scattering process in which the energy of the light is increased to relax the molecular vibration. However, the scattered light has a higher energy than the incident light and this process is much weaker than Stokes Raman scattering. The intensity of Stokes to Anti-Stokes scattering depends on the temperature of the sample and the energy difference between ground and first vibrational state.

2.3.2 Surface Enhanced Raman Spectroscopy - SERS

Surface enhanced Raman spectroscopy is a surface sensitive technique that amplifies the Raman signal from the scattered light of a molecule many times over. In contrast to normal Raman spectroscopy, additional metallic nanostructures are required here which are responsible for the amplification. When observing SERS, therefore, not only the interaction of the photons with the electron shells of the molecules must be considered, but also that between

the light and the conduction band electrons of the metallic structures. The coupling of light with metals and the associated optical properties are called plasmonic.[29]
Plasmons are quasiparticles and describe the oscillations of free electrons that are the consequence of the formation of a dipole in the material due to electromagnetic waves. The natural frequency of these plasmons is mainly determined by the dielectric function of the metal and the surrounding medium. In the case of gold nanoparticles, the natural frequency lies in the range of optical light and can therefore be excited with red laser light, for example. The oscillating field of the laser radiation has a frequency and amplitude which causes the conduction electrons to oscillate and consequently leads to a charge separation which is also called localized surface plasmon resonance (**LSPR**).[29]
Similar to the molecules, the resulting strength of the created dipole depends on the polarizability of the electron shells in the metal and the intensity of the incident electric field strength. The scattered light has the same frequency as the incident light, but the local electric field in the vicinity of the metal particle has been intensified. However, this field drops very quickly ($E(r) \sim r^{-3}$) and is therefore area-selective.[29]

$$\mu_{ind,metall} = \alpha_{metall} E_0(\omega_{inc}) \tag{1}$$

$$\mu_{ind,molecule} = \alpha_{molecule} E_0(\omega_{inc}) \tag{2}$$

μ_{ind} is the induced dipole moment of metals and molecules, α is the polarizability of both and E_0 is the incident electric field.[29]
The SERS intensity depends not only on the incident but also on the outgoing electric field, resp. light, and this is where the Stokes Raman scattering $\mu_{ind}(\omega_{inc} - \omega_{vib})$ comes in.[29]

$$I_{SERS} = I(\omega_{inc}) I(\omega_{inc} - \omega_{vib}) = |E(\omega_{inc})|^2 |E(\omega_{inc} - \omega_{vib})|^2 \tag{3}$$

Here ω_{vib} is the vibration frequency of the molecule. From this equation it can be seen that for $\omega_{inc} \gg \omega_{vib}$ the known $|E(\omega_{inc})|^4$ approximation for the outgoing SERS intensity is obtained, which however applies only well for frequencies in the blue and green but not red or infrared frequency ranges. Furthermore, the sheer orientation of the molecules relative to the surface of the metallic nanostructures is responsible for different SERS intensities, the vibration of a molecules in-plane or out-of-plane being amplified differently. In summary, the enhancement of the local electric field in metallic nano-substrates occurs even without the presence of molecules, but the detection of single or few molecules in Raman spectroscopy is not possible without LSPR.[29]

Enhancement factors (EF): How to measure the magnitude of SERS amplification has been an important question since the discovery of SERS. From the beginning, it was a problem to estimate the number of molecules contributing to the signal and to determine the order of magnitude of the amplification. In view of the postulation of the possible detection of a single

molecule, this was a crucial question. In any case, it has been found that an EF between 10^7 and 10^8 is sufficient for the measurement of single molecule SERS signals.[4]
For many applications, however, it is not necessary to know the enhancement of a single molecule but an average SERS enhancement, which can be used to determine different substrates by their substrate enhancement factor. This can be in the range of 10^4 to 10^6 (10^8 in best conditions) and is strongly dependent on substrate, molecule, laser wavelength, etc.[4]
The average enhancement factor of a substrate is given by:

$$EF = \frac{\frac{I_{SERS}}{N_{SERS}}}{\frac{I_{Ref}}{N_{Ref}}} = \frac{\frac{I_{SERS}}{\mu_S * A * A_{Spot}}}{\frac{I_{Ref}}{c_{Ref} * H_{eff} * A_{Spot}}} = \frac{I_{SERS} * c_{Ref} * H_{eff}}{I_{Ref} * \mu_S * A} \quad (4)$$

with EF the enhancement factor, I_{SERS} intensity of the SERS signal, I_{Ref} intensity of the reference signal, N_{SERS} total number of molecules participating in the signal, N_{Ref} total number of molecules participating in the signal, c_{ref} concentration of the reference solution, μ_S surface density of the molecule, H_{eff} effective height of the scatting volume[4,30] and A the ratio between surface area of nanostructure and the projected area of the laser.[30]

Self-assembled monolayers (SAMs): Metal with clean surfaces have the tendency to adsorb organic molecules, as this reduces the free energy between the metal interface and the environment. When molecules from the gas or solution phase adsorb in regular structures on metallic surfaces and spontaneously organise themselves into crystalline or semi-crystalline structures, they are called self-assembled monolayers (SAMs). All molecules that can form SAMs also have a "headgroup" that prefers certain elements. Alkanethiols, which have a special affinity for noble elements such as gold, are particularly well researched.[31] For this work, 4-MBT (4-methylbenzenethiol) was used to form SAMs.

2.4 Sputtering

In sputtering, solid target materials are bombarded by energetic ionized particles, which are formed by gases or plasmas and further accelerated in electric fields. As consequence, target atoms / clusters are evaporated by the momentum and travel through the same gas / plasma field towards the sample. By that thin layers of the target materials can be brought onto the substrate of interest. Please note, the particle stream of interest can also contain clusters in comparison to the physical vapour deposition, which mainly produces an atomic flux of the target materials. The consequence are slightly rougher coatings, which require post-processing such as thermal annealing. As the latter was indispensably needed for this study, anyway, we exclusively did sputter coating with the instrumentation shown in Figure 10. Please note that the thermal annealing step was not used during this thesis, which means that no further post-processing steps were applied to the samples. As target material high purity gold (99.99 %) was used. This device uses a quartz crystal which is placed in the middle of the sample table to measure the applied film thickness and to stop the process in time.[30]

Figure 10: Leica EM ACE 600 sputter coater at FELMI-ZFE.

2.5 Plasma Cleaning

Plasma cleaning is used as a cleaning step to remove, e.g. possible carbon contamination after purification. For this purpose, gases such as pure oxygen or argon or mixtures are ionised with high-frequency voltages. The gas atoms are excited to a higher energy state and emit a photon when they relax. Since we use pure oxygen in this work, the plasma can be seen as a light blue glow. However, the oxygen plasma also contains atoms, molecules, ions, electrons, free radicals and photons in the UV region. These photons are particularly suitable for breaking down organic compounds of the contamination on the sample. These organic contaminants combine with the oxygen species created in the plasma to form H_2O, CO and CO_2, which are volatile and can be pumped away.[32] For this purpose, the gas discharge apparatus (Gas Entladungs Apperatur - **GEA**) in Figure 11 was used, which is an in-house development. The advantages of this device are the large sample chamber and the simultaneous use as a metal sputter coater.

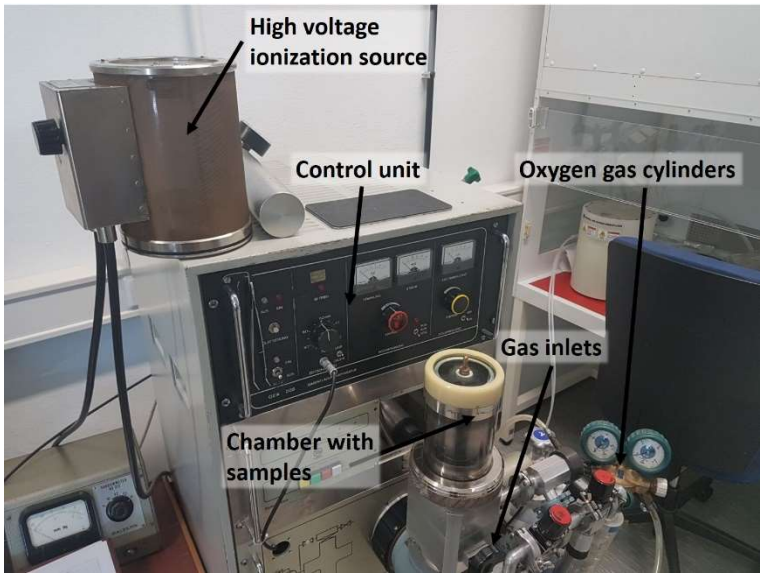

Figure 11: Gas discharge apparatus (GEA) for pure oxygen plasma cleaning at FELMI-ZFE.

3 Previous Work of Relevance

In this chapter, previous work is explained, the results are indispensable and have therefore formed the basis for this thesis. In particular, the master's theses by Winkler[13] in the field of morphology of FEBID structures, Geier[7] on their purification and the dissertation by Fitzek[30] on SERS active sputter substrates.
These studies give a good impression of the parameters that need to be worked with when precise and well-defined deposits with a certain morphology are desired. They show how the carbon can be removed from the deposits and the carbon freedom can be confirmed by means of AFM. Finally, how the plasmonic activity of the FEBID structures and their EFs can be determined using SAMs and Raman spectroscopy.

3.1 Morphology of FEBID Structures

A dedicated study by Winkler et al.[13] in 2013 focused on the influence of precursor dynamics on the morphology of FEBID structures. It was shown that process parameters and patterning strategies lead to different growth styles and thus to a deviation from the desired morphology. Two classic scanning methods are the grid and the serpentine strategy, which can be seen in Figure 12. A feature of the raster strategy (a) is the raised ridge at the starting points of each raster line. The reason given for this is the increased replenishing time compared to other patterning points in the structure, which leads to more pronounced growth. With the serpentine method (b), the surface is not perfect, but it is more even and therefore more suitable.[13]

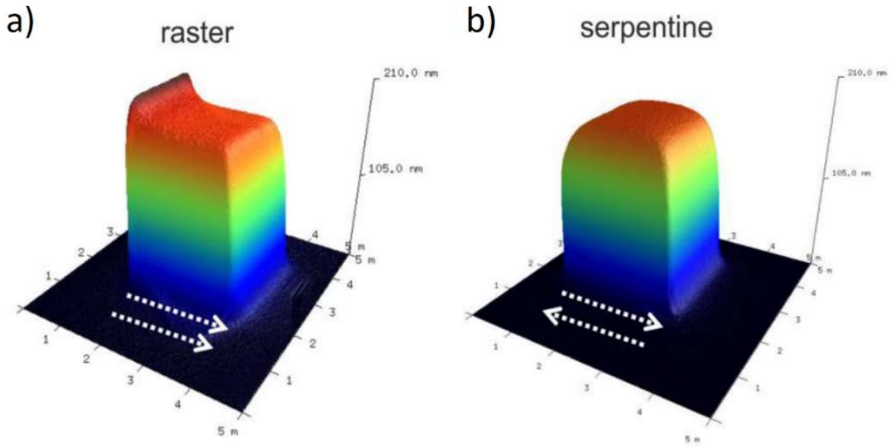

*Figure 12: 3D AFM representation of deposits made via raster **(a)** and serpentine **(b)** patterning method. The deposition parameters used were 5 keV accelerating voltage, 1600 pA beam current, 1 µs DT and 1000 passes. The white dashed arrows indicate the patterning direction.*[13]

After the structure continued to cause problems, the underlying cause was identified, namely that the deposition is finite and thus the electrons can leave the originally intended area. This in turn leads to the effect of unwanted lateral growth of the depositions and to rounding at the top edges. The lateral base enlargement is due to the fact that the electron beam has a certain diameter and SE as well as BSE electrons cause further dissociations which trigger the unwanted growth, especially under MTL conditions.[6]
Furthermore, it turned out that the interaction volume must be treated on the basis of substrate and deposit. In his case, the substrate was SiO_2 with density 1.74 $g.cm^{-3}$ and the deposit was

PtC_5 with density 7.96 $g.cm^{-3}$. At low deposition heights, many electrons enter the low-density substrate and dominate the process at the base as BSE of lateral enlargement. If the interaction volume is completely in the high-density material, the backscattering coefficient increases and the BSE are in a smaller area.
The rounding at the top edges, in turn, is caused by the lack of neighbouring patterning points and the resulting reduction in the number of electrons responsible for the dissociation. Many electrons leave the deposition through the side walls, but compared to a patterning point in the middle or at the corners, many fewer electrons return. The deviations from the ideal desired shape can be reduced by keeping the beam current very low and working in the RRL regime, which leads to enhanced diffusive replenishment.[13] There are four different shapes for the serpentine method when DT and beam current are changed. It is important to mention the "bowl" shape which is to some extent an inverse case of top edge rounding and only occurs at small beam currents and small DT's, as in in the diffusion enhanced regime, and the desired "balanced" shape which has a relatively flat surface and can be generated for a mid-range of parameters, shown in Figure 34.[13]

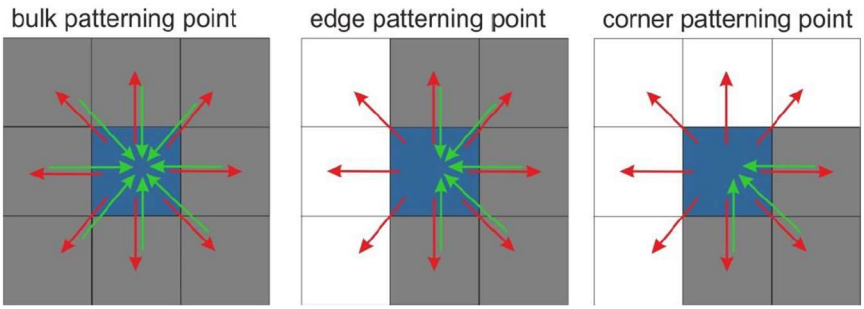

*Figure 13: Schematic representation of the rounding at the top edges; The **blue square** is to represent the current patterning point, while the grey squares are neighbouring patterning points and the white ones are vacuum. The **red arrows** leave the patterning point while the **green arrows** come from another and contribute to the deposition.*[13]

From these findings, it can be concluded that the serpentine patterning strategy in combination with small beam currents is suitable for the most uniform structures possible. This also reduces lateral base broadening and the deviation from the intended morphology. This approach seems to be the most appropriate for this work.

3.2 Purity of FEBID Structures

A new, simple and rapid approach was introduced by Geier et al.[7] in 2014 for the purification of FEBID structures. Using the platinum precursor $MeCpPt^{IV}Me_3$, it was shown that under electron bombardment in H_2O atmosphere, these deposits can be completely freed from the carbon within the structure.
Investigations were carried out how different Pt-C matrices formed either under MLR (polymerised carbon) or RRL (incompletely dissociated precursor molecules) conditions affect the purification properties.[33] In the first case, the currents and DT's are large (1600 pA and 100 µs) and in the second case, the currents and DT's are small (25 pA and 1 µs), both at 5 keV acceleration voltage. The experiments concerning the purification were carried out in an ESEM and in a low-vacuum range of 10 and 100 Pa in an H_2O atmosphere at room

temperature.[7] The purification studies were accompanied by *in situ* and *ex situ* EDXS measurements. Beam current, DT and PoP were varied at several times, to see if the electron beam parameters had an influence on the purification.
Geier et al.[7] were able to prove that for deposits initially made under RRL conditions, a significantly higher carbon content is present, which can be seen in Figure 14. Thus, an as-deposited C/Pt ratio value of ~2.1 for RRL structures and ~1.4 for MLR structures (b). At the same time, it turned out that this difference has no influence on the purification rates (a,c).[7]

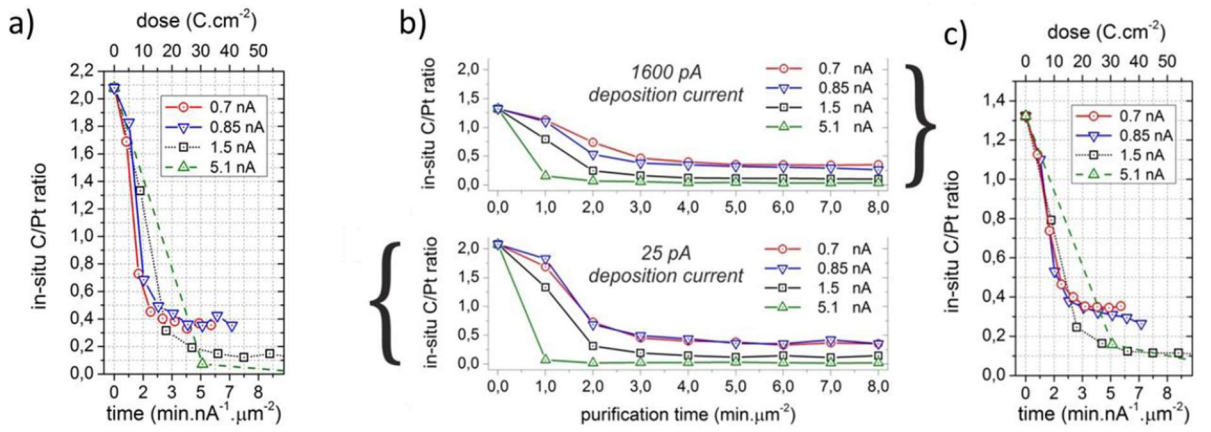

Figure 14: In situ C/Pt time evolution of purification. ***a)*** *Time evolution for initial MLR deposition regime.* ***b)*** *Corresponding C/Pt ratios as a function of purification time for both deposition regimes.* ***c)*** *Time evolution for initial RRL deposition regime. Please note, that both time evolutions have normalised X-axes, which show converging behaviour and thus indicate RRL regime during purification.*[19]

For deposits with an initial thickness of 68 to 75 nm, purification rates better than 5 min.nA^{-1}.µm², corresponding to a dose of about 30 C.cm^{-2}, are possible. With purification parameters of 5 keV accelerating voltage and 5 nA beam current, these structures can be completely purified within 60 seconds. Furthermore, it was shown that for a wide range of DT and beam current, already 10 Pa H_2O pressure is sufficient to ensure RRL conditions, leading to full purification in shortest times (Figure 15).[7]

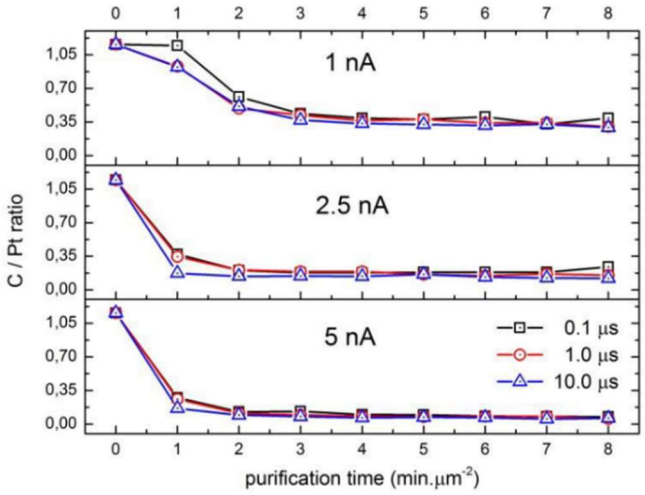

Figure 15: In situ C/Pt time evolution for deposits with an initial thickness of 70 nm purified at different beam currents and DT's.[19]

In addition, investigations via TEM showed that the FEBID structures are indeed carbon-free and that there is a growth increase in the Pt grains. At 5 keV acceleration voltage, structures up to an initial height of 150 nm can be completely purified.
In order to be able to make statements about the morphology and shape fidelity of the structures after purification and how it relates to the volume loss, Geier et al.[7] also carried out AFM measurements of the samples (Figure 16). For a deposition with an initial thickness of 60 nm, it was shown that the structure after purification is pore- and crack-free and at the same time the original footprint is preserved after deposition with a slight shrink of 4 % in lateral dimensions.

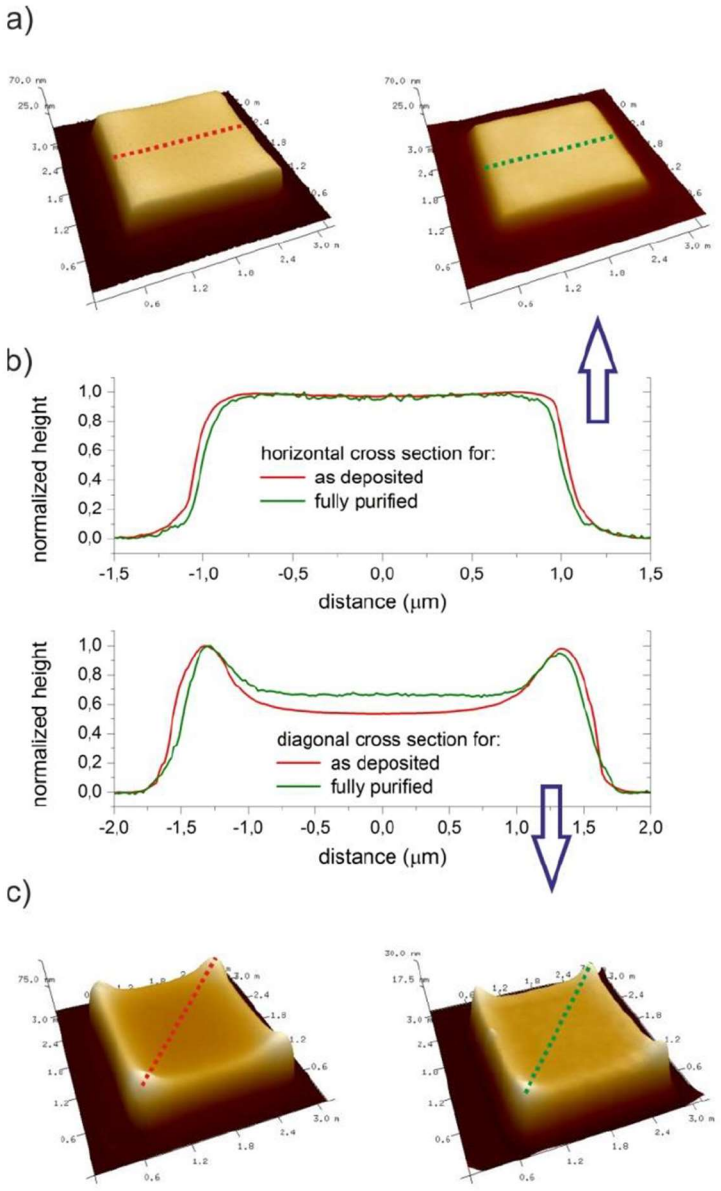

Figure 16: 3D AFM representations of FEBID deposits. ***a)*** *"Balanced" shape deposition before (left) and after (right) purification.* ***b)*** *Normalized cross sections of both structures before and after purification.* ***c)*** *"Bowl" shape deposition before (left) and after (right) purification.*[19]

Furthermore, it was evaluated whether the shrink of the deposit is homogeneous or not. For this purpose, the sample was measured with the AFM after deposition, as partially purified and completely purified, which can be seen in Figure 17.[7]

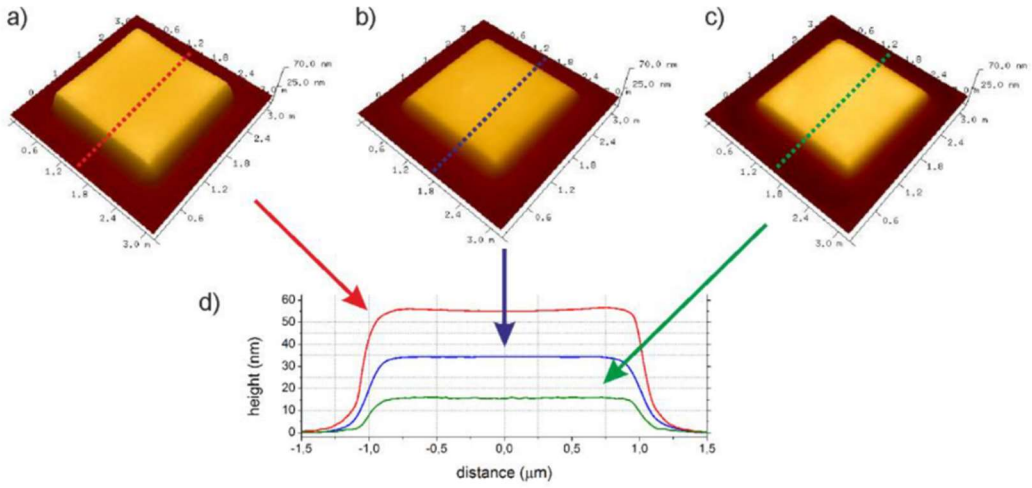

Figure 17: AFM images of a Pt-C deposit. ***a)*** *As deposit.* ***b)*** *Partly purified (5 min, 1 nA, 1 µs DT, 5 nm PoP).* ***c)*** *Completely purified.* ***d)*** *Cross section of all pads marked as doted lines.*[19]

For deposits, initially fabricated under MRL conditions, the relative volume loss was 69±3 vol.% (in theory 70 vol.%)[34] in contrast to 77±3 vol.% for those prepared in RRL conditions. However, that is not surprising as it is well known, that fabrication in MRL conditions lead to higher metal contents, which consequently entails a reduced volume reduction when removing the remaining carbon.Winkler at al.[6] were later able to successfully apply this process to the gold precursor Me_2-Au(acac),[6] which contains up to 95 at.% carbon after deposition,[16] in another paper.[6] The choice of deposition regime has a direct influence on the amount of carbon in the deposits and is reflected in the value of the volume loss after purification, which is important for later AFM measurements. Initial parameters for purification were found and the structures should be pore- and crack-free after purification and show a uniform vertical shrink. In addition, there is a maximum starting height of 150 nm for the FEBID structures, as otherwise complete purification is no longer possible.

3.3 Gold Sputter SERS Substrates

In his PhD thesis,[30] Harald Fitzek compared the enhancement factors of simulated SERS substrates with those of measured factors. For this purpose, plasmonically active substrates had to be created first, which is also of great importance for this master's thesis. In order to obtain nanostructures, that are capable of massively boosting the Raman signal, only materials with appropriate dielectric constants[35] (Au, Ag, Cu) and surface morphologies are relevant.[36] Among the different fabrication possibilities for SERS substrates, sputtering and thermal annealing was used due to the simple character.[37] First, a nominally 2 nm thick gold layer was sputtered onto pre-cleaned glass substrate. Subsequently, thermal annealing was done at 200 °C for 30 min in dry air and then cooled at room temperature. Next, a 10^{-4} molecular methylene blue solution in water was prepared and spin coated onto annealed SERS and glass-only substrates using 4200 / 4200 rpm for 4 / 20 seconds with acceleration rates of 1500 s^{-1} and 800 s^{-1}, respectively. While the glass-only references did hardly yield a Raman signal, The Au SERS substrates gave strong Raman signals with good reproducibility.[30] For the determination of the SERS-EF, however, it was necessary to use a non-fluorescent molecule. Thus, 4-methylbenzenzthiol (**4-MBT**) was chosen due to its SAM characteristics

(Au – SH group binding). That provides a widely homogeneous layer thickness as well as low adsorption[38,39] and strong chemical enhancement,[40] which is why 4-MBT is often used for evaluating performances for different Raman concepts.[30] Due to both, the high overall performance and available literature, we also used 4-MBT as main test analyte in this thesis.

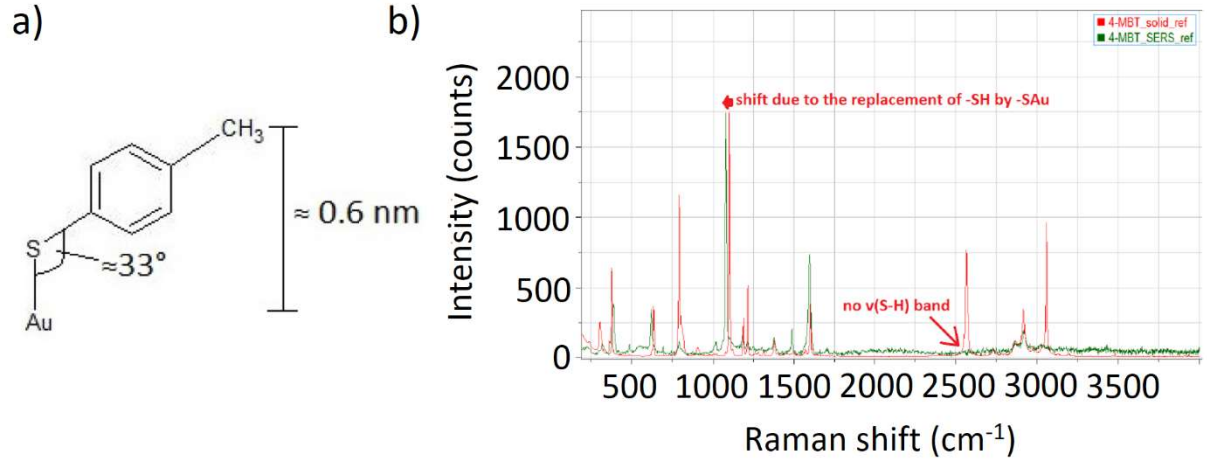

Figure 18: ***a)*** *Schematic representation of 4-MBT bonds to Au by replacing the S-H with an S-Au bond. Bonding angle and height of the molecule can be found in this article.*[38] ***b)*** *Raman spectra of 4-MBT without additional bonding* ***(red)*** *and with shifted peaks after bonding with the gold surface* ***(green)****. After bonding, the S-H band at 2560 cm*$^{-1}$ *is missing and the band at 1100 cm*$^{-1}$ *is slightly shifted due to the S-Au bonding.*[41]

To be sure that the Raman signal is coming from the SAM, it must be possible to distinguish between bonded (a) in Figure 18) and unbonded 4-MBT in the spectrum and a cleaning procedure must be found to remove unbonded layers. The concentration of the molecular solution and the immersion time also had to be determined. Fortunately, the bound molecule can be easily identified as the strongest band in the spectrum (ν(C-S) vibration at 1100 cm^{-1}) is clearly shifted and the band at 2560 cm^{-1} (ν(S-H) vibration) disappears completely, which can be seen in Figure 18 (b).[30] A suitable cleaning solution in the literature,[42,43] in which the sample is held briefly in ethanol after wetting and carefully dried with the CO_2 spray. As with methylene blue, 4-MBT was first applied to the sputtered glass substrate and the necessary concentration for detection in the Raman spectrograph was determined using different concentrations of the molecule in water. The necessary residence time of the sample in the solution was also investigated and both can be found in Figure 19.[30] A 10^{-4} molecular solution at an immersion time of 1 h is sufficient for a closed monolayer. It is important to note that a SAM has a lower reproducibility than layers created with spin coating, which is logical due to the multilayer nature of spin coating. However, in order to determine the EF, a monolayer is necessary and this approach is mandatory. But since there is no way to guarantee a monolayer with every attempt, the potential for errors is naturally very high. Fitzek also noted that Ikeda et al.[40] found a dependence of the chemical amplification of 4-MBT on the orientation of the substrate, which is impossible to control for on sputtered samples.[30] As mentioned before, a switch from glass to Si wafers for better AFM images, which initially did not give good results due to coarser impurities, but an extended cleaning strategy solved this problem and reproducibility of the 4-MBT SAM became comparable to that of glass slides.[30] A guide to the preparation of SAMs of 4-MBT was found and that the determination of the plasmonic activity can be carried out by means of Raman spectroscopy. It is also clear that problems and difficulties of reproducibility of both monolayer and SERS signal are to be expected.

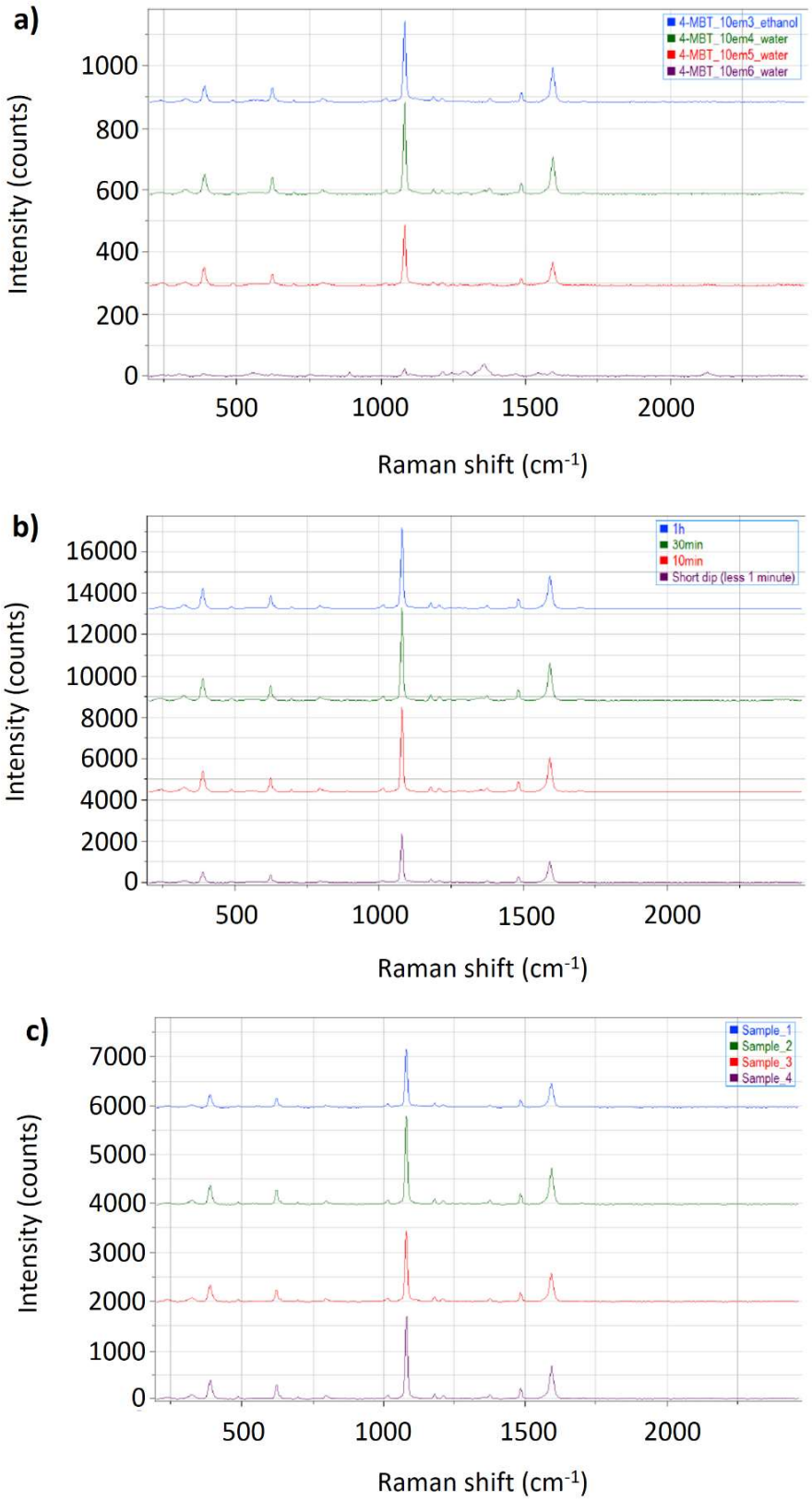

Figure 19: Raman spectra of 4-MBT on sputtered gold with glass substrate. ***a)*** *SERS measurements of substrates from the same batch but in different molecular solutions after spending 1 h and drying with the CO2 spray.* ***b)*** *SERS measurements of substrates from the same batch in a 10^{-4} molar solution of 4-MBT but for different immersion times.* ***c)*** *average SERS spectra of substrates from the same batch measured for reasons of reproducibility of 4-MBT SAM deposition.*[41]

4 Experiments and Results

The aim of this thesis was the controlled fabrication of plasmonically active Au nanostructures via FEBID including their optimization to be comparable with traditionally prepared Au SERS substrates. A graphical representation of this process can be seen in Figure 20. For that, 2.5D nanostructures[1] were fabricated via FEBID on Si-SiO_2 substrates (~4 nm oxide)[19] and regularly checked via AFM with respect to their morphology and to be able to determine the volume loss after purification. The purification of the structures was carried out in a second DBM, which offers a H_2O based low-vacuum mode for our purification approach. The structures were again analysed with the AFM to document possible morphological changes and to determine the volume loss in order to be able to say whether they are carbon-free or not (saturation determination). Verification of the plasmonic activity and the determination of the enhancement factors were done via a standalone Raman microscope in comparison to standard Au SERS substrates. Two molecules were used as evaluation analyte for the plasmonic activity, namely 4-MBT and methylene blue. During this work, not only deposition and purification parameters were varied but also combined with additional ex-situ treatments for different purposes to separate influences and clarify individual observations.

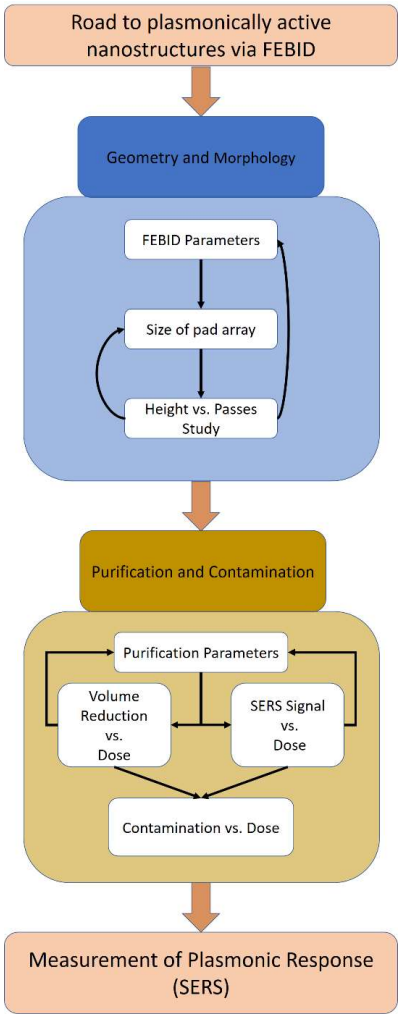

Figure 20: Road to plasmonically active nanostructures via FEBID.

[1] 2.5D structures are structures that serve as the basis for "real" 3D structures. 2.5D structures can be cuboids, pillars, walls and overhangs, among others, which together result in structures that are identified by their three-dimensional character.[45]

4.1 Experimental Details and Procedure

This section informs about applied devices, process procedures and individual parameters. While maintained for most experiments to ensure mutual comparability, specific adaptions were done to clarify individual aspects. Those deviations are mentioned in the related sections.

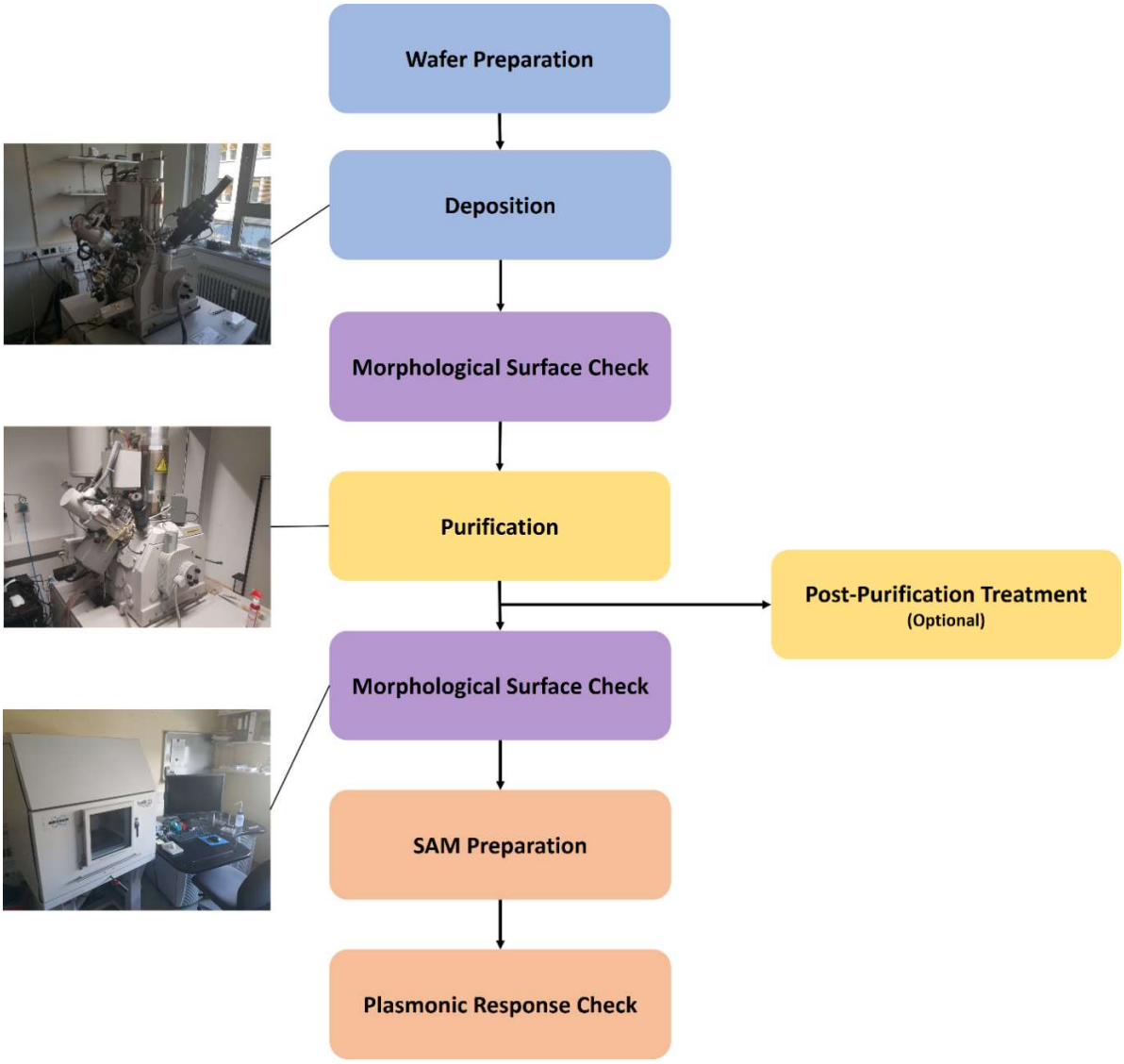

Figure 21: Schematic overview, which is valid for most of the experiments in this thesis. Deviating procedures are explained separately. Fields with the same colour belong together thematically.

Figure 21 shows the general sequence within the experiments during this thesis. The individual parts are now explained below:

1. **Wafer Preparation:** A single stab holder was precleaned with high-purity ethanol and an optical lens tissues. It was then put in a laboratory glass with isopropanol, placed in an ultrasonic bath for 5 minutes and then dried with a CO_2 spray. Afterwards, a self-adhesive carbon tape was applied to fix at the wafer. Special silicon wafers with a 4 nm oxide layer were taken from a wafer carrier box. The pre-cut wafers (approx. 1x1 cm) were detached from the wafer holding disc and placed on the single stab holder.

2. **Deposition:** The deposition of gold for plasmonic structures was done in two ways. As reference samples and for some test series the wafers described above were sputtered with the Leica ACE 600 sputter coater. The following parameters were used:
    a. Layer thickness: 4 nm
    b. Sample height: 1 mm
    c. Current: 15 mA
    d. Pressure / Gas Type: 5×10^{-2} mbar / Ar
    e. Working distance: 30 mm
    f. Tilt: 0.0 °

    The actual gold pads were deposited using the FEBID technique with the DBM Nova 200 (FEI, The Netherlands), which can be seen in Figure 2 (a). After preparation, the wafers were taken immediately to the DBM and blown off with the CO_2 spray before closing the vacuum chamber. After a vacuum range of 10^{-6} mbar was reached, the sample was transferred to the eucentric height of the microscope and both electron (5 keV; 98 pA) and ion (30 keV; 1 nA) beam were focused on a prominent feature in the wafer corner.
    After a quick check of the desired area, to verify whether coarser dirt (larger particles, etc.) is making the area unusable, the sample was moved 1 mm in x and y direction from the sample corner and tilted 52°. Here, square "frames" with a diameter of 10 µm were milled with the ion beam which can be seen in Figure 22 (a,c). These units are indispensable for finding the structures in the light microscope and, due to the simple geometry, the FEBID structures deposited in the center of the frames can be found more easily. Before the deposition of the Au pads, the sample was tilted back to 0° and a sharpening field[2] (5x5 µm; 1 ms DT; 500 nm PoP, 360 s TET) from the platin-precursor ($(CH_3)_3Pt(CpCH_3)$) was deposited between the FIB frames (b,d) to prepare the actual electron beam for the deposition of the Au Pads.
    Before the actual Au pad deposition, which was made from $Me_2Au(acac)$ precursor, the beam parameters were changed to 30 keV / 21 pA due to obtain the most even structures possible with minimal lateral broadening. In the following, the beam astigmatism was minimized by using the sharpening field. After the beam has been optimized, the centre coordinates of each FIB processed frame were determined to allow moving blindly towards frames between depositions to prevent unwanted deposition or contamination. In order to deposit the FEBID structure as centrally as possible in the FIB frame, the edges were searched for using the reduced are image (F7 window) without illuminating the area in the middle.
    The precursor reservoir was heated to 30 °C at least 30 minutes before deposition and then the GIS needle inserted and gas valve opened. In order to reach thermodynamic equilibrium between the precursor and the substrate, additional 15 minutes are waited. Before the GIS opening, the pressure in the chamber was in the range of ~2×10^{-6} mbar and increased by ~5×10^{-6} mbar directly after the opening. By the time of deposition, the pressure had dropped again to a value of ~3×10^{-6} mbar. To get rid of space charge effects, which can have a negative impact on the deposition behaviour, a drift compensation field is deposited approx. 1 µm from the actual structure before the main deposition begins. Such a field can be seen in Figure 25. For the actual deposition of the Au pads, the serpentine strategy was used and a square pattern with 500 nm side

[2] A sharpening field is an array of fine FEBID pillars that are used to optimise the electron beam in terms of its alignment (Lens Alignment, Source Tilt, Stigmator, Focussing).

length drawn up. DT and PoP were set at 1 ms and 10 nm, respectively. At the end of deposition, the GIS valve was closed, the needle withdrawn and the wafer moved to the next sample location.

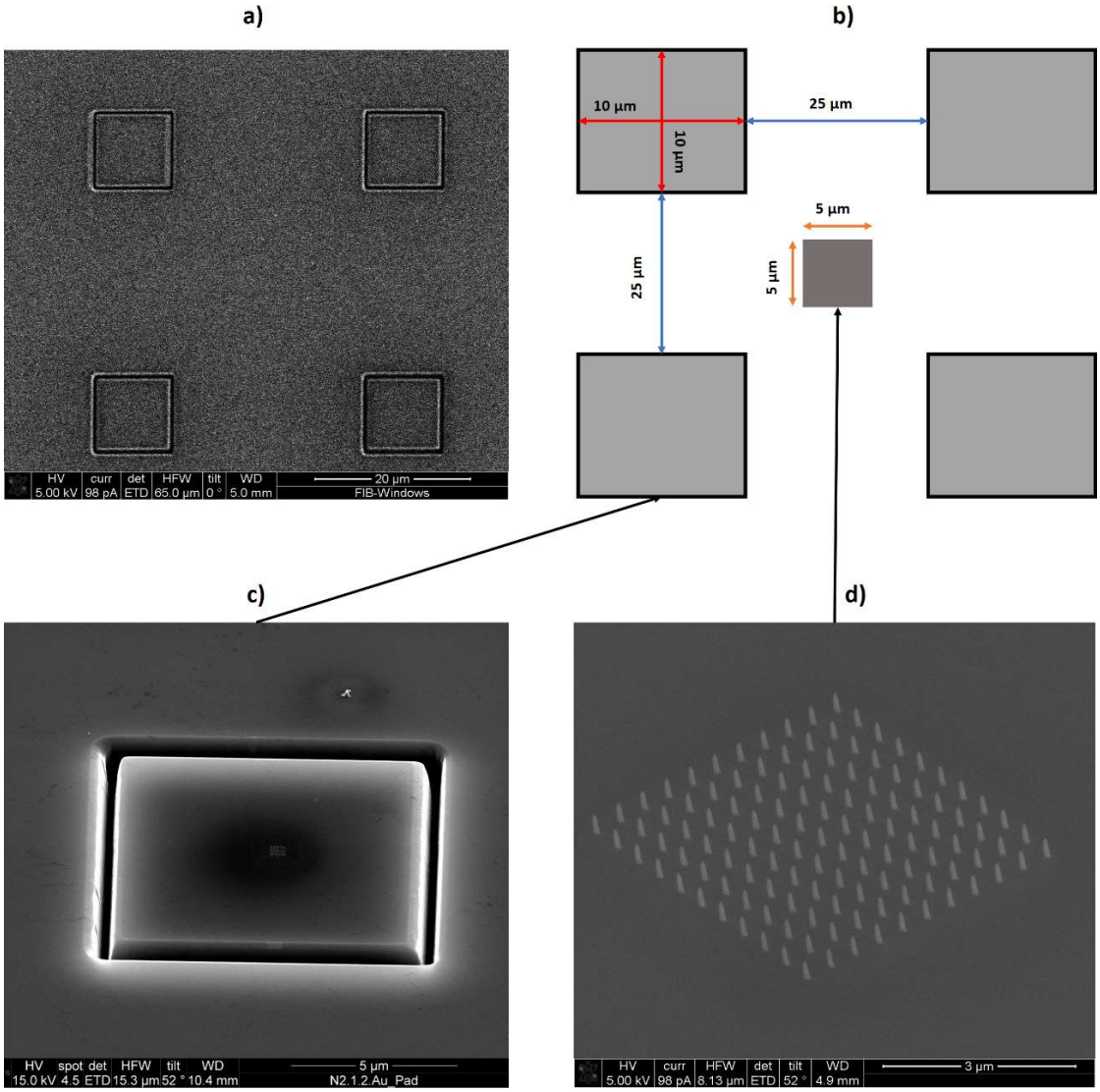

Figure 22: ***a)*** *SEM image of four FIB "frames".* ***b)*** *Matching schematic with the positions of the units, their sizes and distances to each other. The sharpening field is in the centre.* ***c)*** *52° tilted SEM image of one FIB "frame" with a deposition in the middle.* ***d)*** *52° tilted SEM image of the sharpening field array in the centre of the arrangement.*

3. **Morphological Surface Check:** Whether after deposition or purification, the samples remained in the vacuum chamber of the electron microscope, if possible, until investigation. If this was not possible, the samples were always parked in a desiccator in the meantime. The FEBID pads were examined as deposited and after purification. In addition, some pads were examined after post-purification treatments and to detect morphological changes after the sample resting (thermodynamic equilibrium) phase. For verification of the intended geometry, morphology and volume loss an atomic force microscope (Brucker FastScanBio AFM) with TESPA-300 tips from Brucker in TappingMode^{TM} was used. Before each investigation, the cantilever was first placed in the appropriate holder. A light microscope was used to help with positioning and the cantilever was placed so that its edges did not touch the inner frame of the holder

(important for later cantilever tune). Then the holder was connected to the scan head of the AFM, both can be seen in Figure 6. The sample to be examined was placed in one of the holders and rotated underneath the scan head. The cover of the AFM was closed and the experimental procedure was selected in the software and the standard calibration (tip focusing, cantilever tune, laser alignment, etc.) was carried out. Then, with the help of the AFM's light microscope, the scan head was carefully lowered towards the sample surface so that one corner of the wafer was in focus. Subsequently, the FIB "frames" are searched for, which are approx. 1×1 mm away from the said corner and refocused on these again at the highest magnification. The tip is placed in the centre of the square FIB frame, a 500×500 nm scan area is set in the software and the approaching surface procedure is initiated. Then a repulsive working regime was set with the settings for "drive amplitude" and "amplitude setpoint". The values are optimised until no black/white stripes are visible. If there is noise in the amplitude image, the "integral gain" changes the values until it disappears. The scan size is increased to 2×2 µm and the pads are searched for analysis. Different scan sizes were chosen, most frequent 2×2 µm and 4×4 µm at 512 and 1024 pixels. The biggest problems in the investigations are tip convolution issues caused by contamination of the tip, but also the setting of the working regime and keeping it stable during the measurement. Replacing the cantilever in the holder is also a challenge each time because of its tiny size.

4. **Purification:** For the purification, the samples were transferred directly from the AFM or desiccator into the DBM and pumped down to a vacuum better than 10^{-5} mbar. To determine the electron current for purification, a Faraday cup was used, which was mounted directly at the single stab sample holder. Prior to the actual purification, the electron beam (30 keV; 8,7 nA) was optimized and focused on the sharping field. Afterwards, the microscope was switched to low vacuum mode (80 Pa) and the electron beam was optimized again. Similar to the deposition, the center point coordinates of the FIB “frames” were again determined to reduce additional contamination between purification processes. With the help of the internal patterning engine, a square field with a side length of 800 nm, 1 µs DT and 7 nm PoP as well as different dose values were set. Serpentine was also chosen as the patterning strategy. After that, a fast image with 100 ns DT was drawn in at the first pad to see the position of the gold pad. The patterning field was placed over it and the purification was carried out. This procedure was carried out for all pads of a sample and then ejected. If the AFM was not available immediately afterwards, the sample was temporarily stored in the desiccator.

5. **SAM Preparation:** After a second AFM evaluation of the FEBID samples, both deposition and sputter samples were ready for SAM preparation. 265±20 mg of 4-MBT was dissolved in 50 ml ethanol to obtain a 10^{-2} molar solution and then 1 ml was taken and added to 100 ml distilled H_20 to obtain a 10^{-4} molar solution of 4-MBT. The samples were immersed in the solution for one hour and then dried in air (Figure 23).

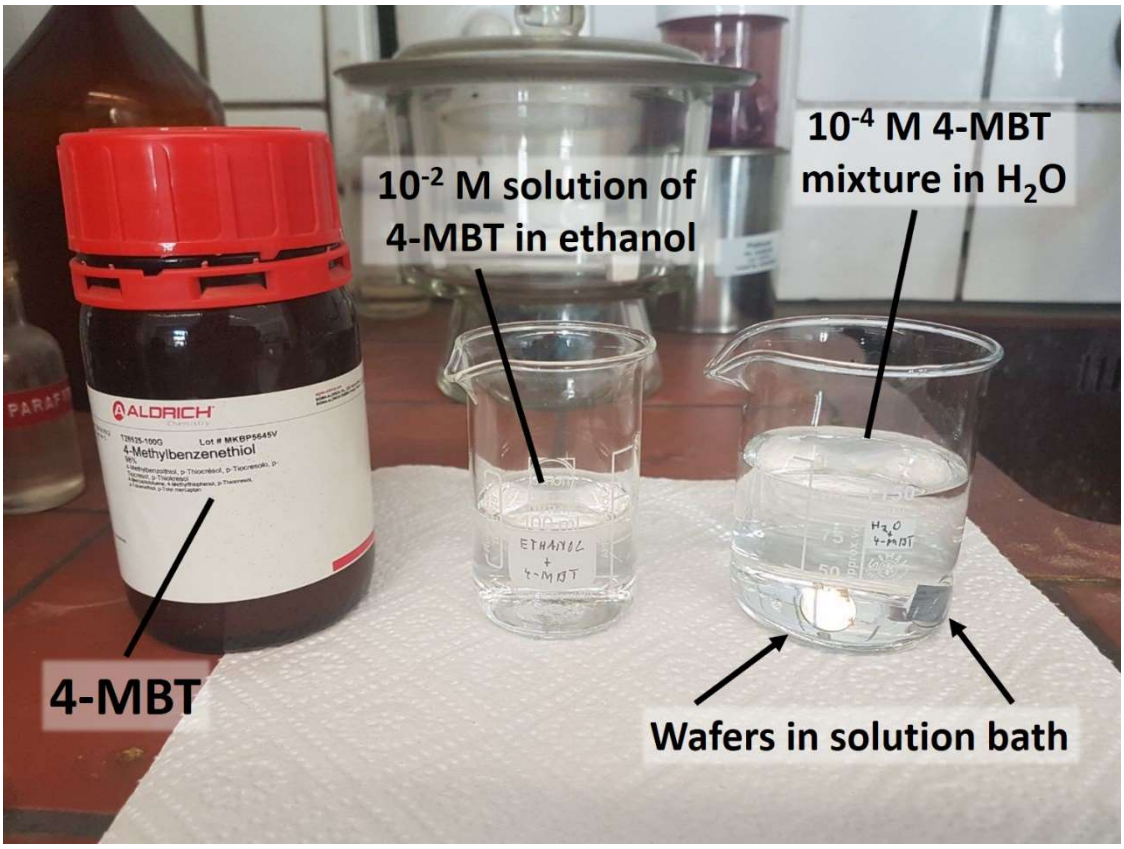

Figure 23: Example setup for wetting the wafers with the desired molecule for SERS measurement.

6. **Plasmonic Response Check:** The plasmonic activity and the determination of the enhancement factors of SERS was performed using a Raman microscope (Jobin Yvon LabRam 800HR\Olympus BX41, Horiba). The laser (633 nm wavelength) used for the measurements was warmed up half an hour before the start of the measurement to achieve a stable operating temperature of the laser, while the samples were still in the solution. Before each measurement, a frequency calibration of the device is carried out with a silicon wafer and then the actual Raman measurements were performed on the sputter and FEBID samples. The following settings were used:
    a. Objective: Olympus LMPLFLN50x (NA = 0.5)
    b. Spectro: 2130 cm^{-1}
    c. Acquisition time: 30 s
    d. Accumulations: 2
    e. Confocal pinhole: 500 µm
    f. Slit: 200 µm

7. **Optional Post-Purification Treatments:** A number of FEBID samples were treated with post purification procedures: Plasma cleaning (2.5) and milling with the ion column of the DBM Nova 200.

4.2 Geometry and Morphology of Au Pads of Different Sizes

This section deals with the geometry and morphology, especially in terms of lateral sizes, surface shapes, deviations from desired forms and reproducibility, of the FEBID gold pads produced during this work.

Getting started with “small” pads with an intended side length of 100 nm, where first the height of each pad in relation to the number of passes is analysed (4.2.1.1). Then, gas flux problems of the precursor material show variations in the height of the structures (4.2.1.2). Arrays with equal passes, but with a different patterning strategy suffer from the same problems with additional uneven morphologies (4.2.1.3). To avoid these morphological problems by the gas flux, the pad design was changed from "small" to "large" pads. While the deposition parameters were kept the same, side lengths were increased to 1 µm (4.2.2.1). To achieve homogeneously flat surface morphologies (also called “balanced” shapes), FEBID parameters were further optimized (4.2.2.2).

4.2.1 “Small” Au Pads

This subsection deals with geometry and morphology issues for the "small" gold pads. In Figure 25 you can see the height vs. passes study and afterwards in Figure 26 the corresponding growth curve. Figure 27 and Figure 28 deal with the cross sections of these pads. A large size array of 64 pads together with the height distribution curve can be found in Figure 29 and Figure 30. Smaller arrays of different sizes, made with the parallel patterning technique and together with the cross sections showing the disturbed morphology, are in Figure 31 and Figure 32.

4.2.1.1 Structural Height vs. Passes

In the first step on the road to plasmonically active nanostructures (Figure 20), suitable parameters, strategies and array sizes must be found that fulfil precisely defined structures with adjustable morphology and reproducibility. For this purpose, we start with a certain set of values that have already resulted in well-defined structures with minimal lateral bass broadening in other experiments (section 3.1). An electron acceleration voltage of 30 keV and a beam current of 21 pA, together with 10 nm PoP and 10 µs DT form the initial values. A square pattern with a side length of 100 nm is selected as the geometric footprint and the serpentine patterning strategy (section 3.1) with "bottom to top" towards the GIS nozzle is applied. From the chosen parameters and the patterning strategy one can already deduce from Figure 24, which morphology is expected for the gold pads. It is important to mention here that these "bowl" shaped pads are built as serial patterning, one after the other.
To find out which number of passes results in a certain pad height, it is necessary to perform a height vs. passes study, which can be seen in Figure 25. As expected, the pads have a lateral broadening at the base. The pads of interest in terms of the expected height after purification are pad 6 and 7. Pad 6 was deposited with 5000 passes and shows a lateral broadening per side of 25 nm, both in the x and y direction. The difference between the deepest point of the bowl and the tips is 14 nm. At pad 7 (10000 passes), the lateral widening already reaches values of 30 nm and the difference in height in the bowl is 20 nm. This shows that with increasing passes, both the widening and the formation of an increasingly prominent "bowl" shape increases with respect to Δz.

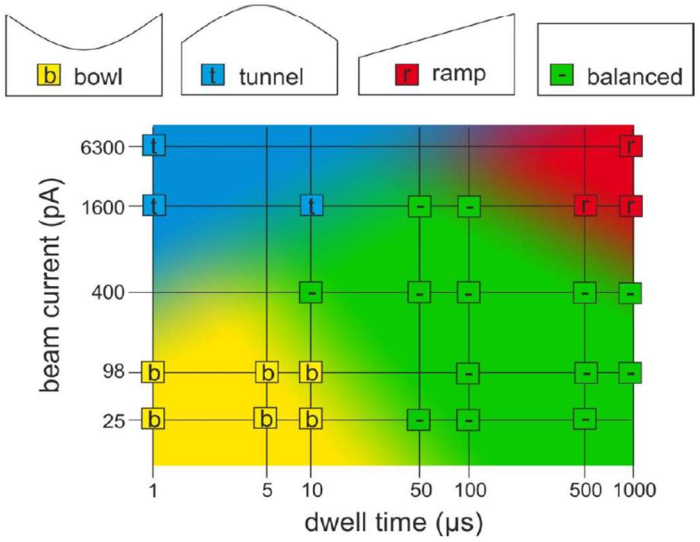

Figure 24: Schematic representation of the four main morphologies of FEBID structures as a function of beam current and dwell time for serpentine patterning. [13]

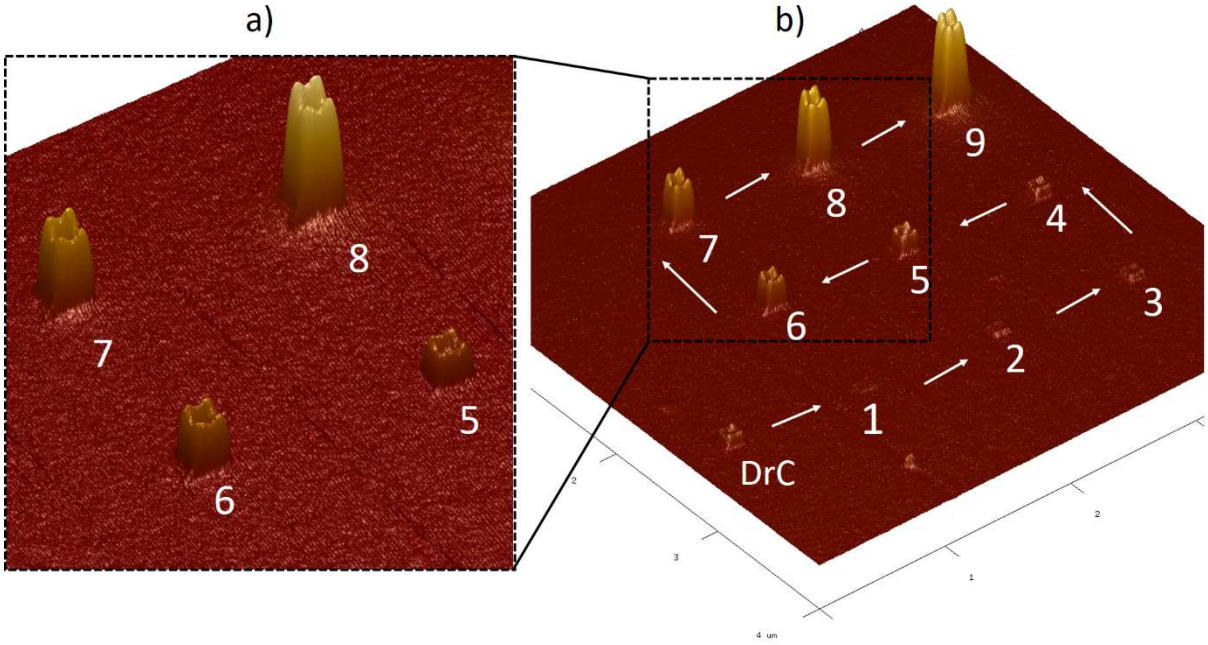

Figure 25: AFM 3D representation of the Height vs. Passes study for "small" Au FEBID pads produced via serial patterning. ***a)*** *Zoom to the area with pads whose passes to height relation is interesting for further calibrations.* ***b)*** *Image of the whole array. The numbers represent the pads and together with the white arrows for the order in which they are made. DrC marks the drift compensation field (4.1).*

In addition, the values determined for the height above the passes were plotted in Figure 26 and so a growth curve was created. This curve shows a strong increase with a simultaneous high rise in the number of passes, which was to be expected. Basically, this investigation has to determine whether the existing deposition parameters meet the requirements and which pass value has to be used for further calibration. One of the criteria is the structure height, because a height of more than 150 nm (see chapter 3.2) would lead to a structure that could only be partially purified.

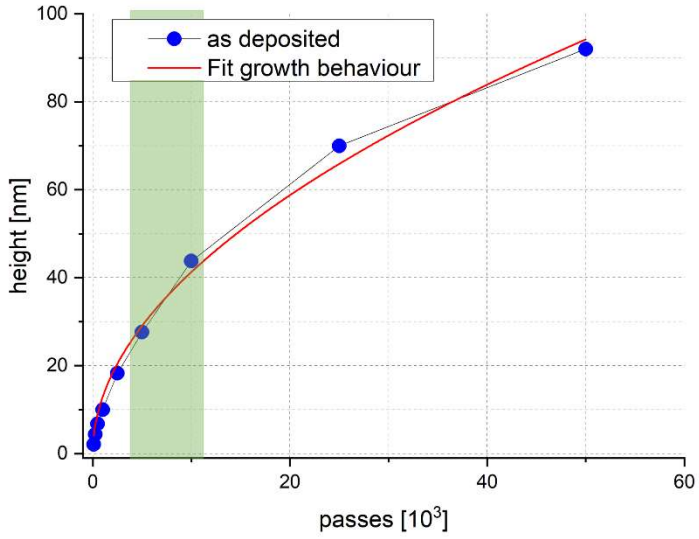

*Figure 26: Growth curve of the Au pads for increasing passes during deposition. Minimum for pad 1 with 100 passes and maximum for pad 9 with 50000 passes. The **red line** is a fit of the growth behaviour of the pads with respect to the passes, described by* $y = ax + b\sqrt{x}$. *The semi-transparent **green field** marks the area of interest with regard to the initial height for purification.*

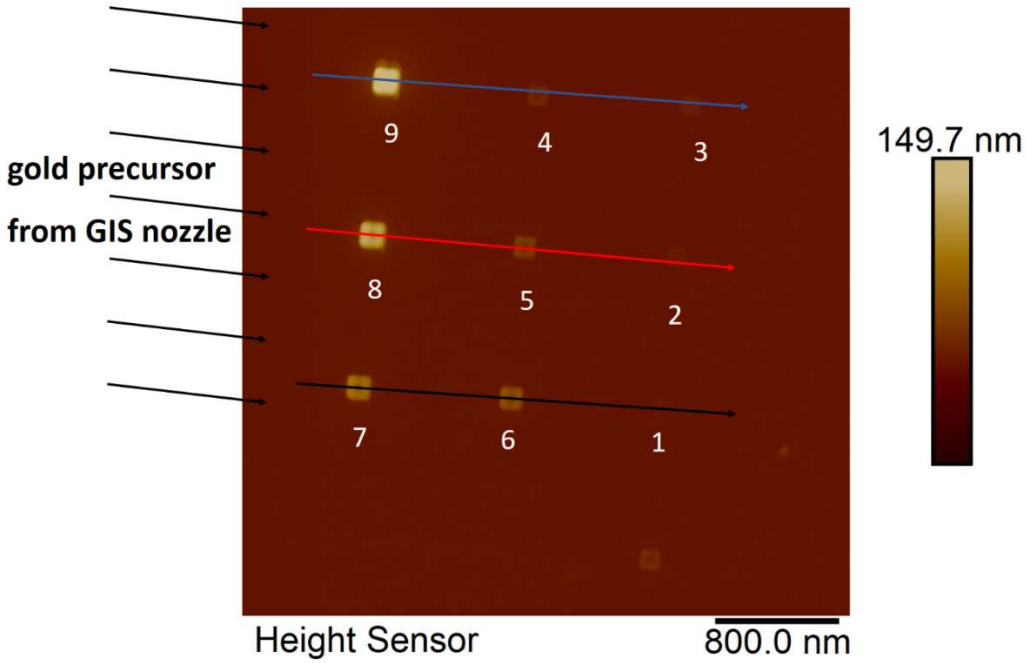

*Figure 27: AFM image of the Height vs. Passes study for "small" Au FEBID pads produced via serial patterning. The short black arrows indicate the direction of the incoming gas flux, while the black, **red** and **blue** arrows indicate the cross section, which is shown Figure 28.*

Another important aspect is the morphology of the individual pads. Figure 27 shows the array with cross section arrows and the direction of incidence of the precursor gas. These cross sections are shown in Figure 28 and again give an impression of the differences in height of the pads in relation to each other, but also of uneven growth for the three largest structures (10000, 25000 and 50000 passes). Since this is hardly recognisable for smaller structures, the

assumption suggests that the precursor density on the structure side facing the GIS is higher and with increasing structure height leads to shadowed regions on the opposite face, which in turn is reflected in the uneven growth, since the "bowl" shape structure is also always a representation of the precursor density distribution at the same time.[13]

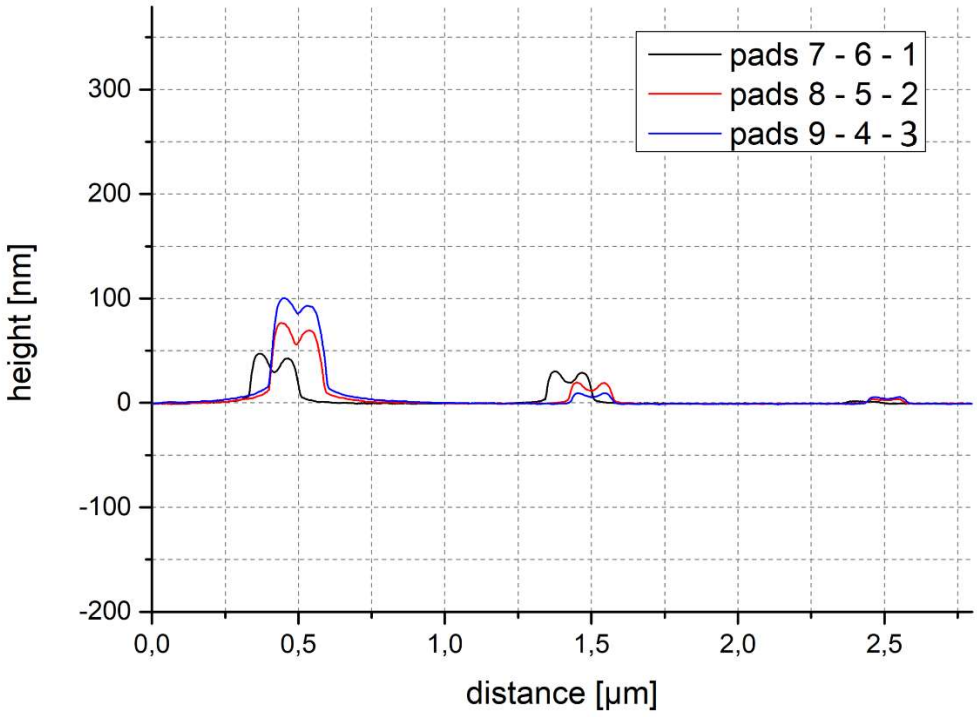

Figure 28: Cross section of the gold pads in Figure 25. The colours of the cross-section lines correspond to the arrows in Figure 27 and indicate the respective pads.

Criteria such as base broadening, morphology, structural height after purification and total exposure time (**TET**) are weighed against each other and pad 7 (10000 passes) is selected for further calibrations. It has an average as deposited height of 45 nm and an expected height of ~10 nm after purification (at approx. 75% volume loss). At this height, it should still be easily distinguishable from the surrounding substrate (silicon wafer). The TET is 10 s and since the next step is to form arrays of variable size with identical gold pads, the production time remains manageable.

4.2.1.2 Height Variation

The reason for forming an array on FEBID pads is that the diameter of the Raman laser is about 1 µm and a contribution to the plasmonically amplified Raman signal of as many pads as possible is desired. With an approximate side length of 3 µm the chance is additionally increased to illuminate a complete covered area with FEBID pads. Since the structures are too small for the resolving power of the light microscope and a 100% positioning of the array in the centre of the FIB “frame” is difficult, a large array is advantageous.

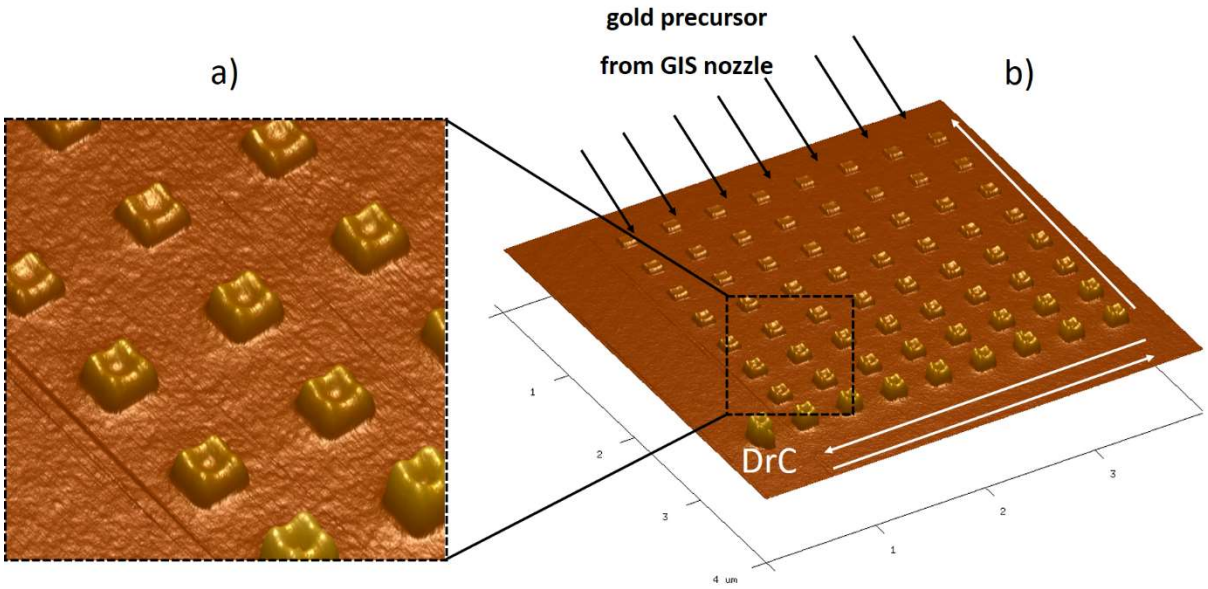

Figure 29: AFM 3D representation of an 8x8 FEBID gold pad array. All pads were made with 10000 passes and have an equal patterning strategy to Figure 25. ***a)*** *Magnification to show both the characteristic shape and the decrease in structural height.* ***b)*** *Image of the whole array. The side-by-side white arrows are intended to indicate the alternating patterning directions at line change, while the single white arrow indicates the general direction of deposition towards the GIS nozzle. DrC marks the drift compensation field (4.1).*

In Figure 29 such an 8x8 pad array can be seen where all pads were made with 10.000 passes. Compared to section 4.2.1.1, the distance between the pads is reduced from 1 µm to 250 nm. TET for the whole array is about 11 minutes. What can be seen at first sight is that there is a dramatic drop in the structural height of the pads towards the GIS nozzle. Das This was not intended, as the order of deposition (serial patterning) has not changed.

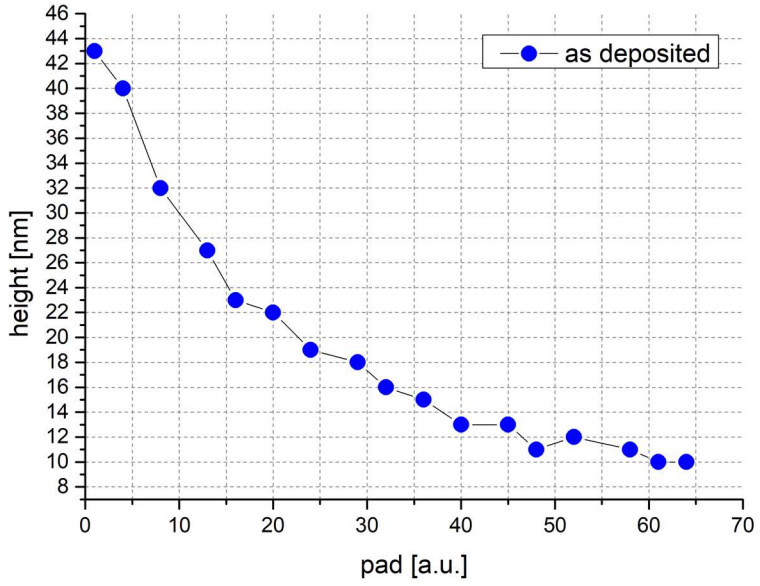

Figure 30: Height vs. pad number diagram of the FEBID gold pads of the 8x8 array (Figure 29). The structures at the beginning of the deposition still show the expected values for height while the strongly reduced growth of the following structures until the end of the deposition is clearly visible.

The fact that this loss of height actually happens very quickly and also runs parallel to the direction of incidence of the precursor gas becomes particularly clear in Figure 30 where the structure height is plotted over the pads deposited with continuous numbering. A major difference, however, is the distance between pads and their number. Since the morphology of the individual structures is in order and no signs of uneven growth can be observed, it is suspected that there are gas dynamics problems which lead to a depletion of precursor material and result in a lower growth of the gold pads. An exit strategy for this trial could be a change in the patterning strategy, which is discussed in the next section.

4.2.1.3 Disturbed Morphology

In the previous section, the serial pattering strategy had problems with the declining trend of the structure height in the direction towards the GIS nozzle. It is possible that precursor gas dynamics problems may arise as a result of the number of pads and their spacing. In order to get the problem under control a different patterning strategy is used, namely parallel patterning. In comparison to serial patterning, where deposition is made consecutively, parallel patterning is done concurrently. In parallel patterning, all relevant patterns are marked and the electron beam will only make one pass per pattern, jump to the next pattern and then start again from the beginning until all passes have been made. The idea behind this is that shadow effects should be avoided and that all structures should grow to the same height.
The results of this experiment can be seen in Figure 31 for a 2×2 array and in Figure 32 for a 3×3 and 4×4 array. Unfortunately, the desired effect did not occur. Although the changed patterning strategy leads to an increase in height of a single freestanding structure and the intended morphology is still noticeable, so the new strategy has led to a completely disturbed morphology.

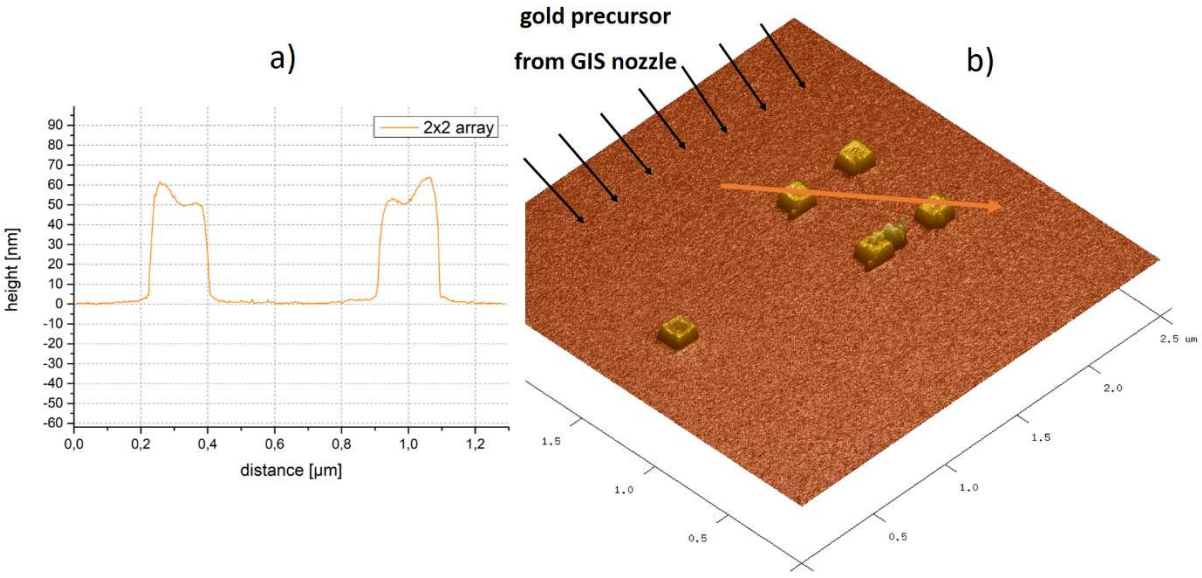

Figure 31: AFM 3D representation of a single pad and an 2x2 pad array made with parallel patterning. ***a)*** *Cross section indicated by the orange arrow. The inward sloping morphology is clearly visible.* ***b)*** *Image of whole array with cross section marker and precursor direction of incidence.*

However, with the 3×3 and 4×4 arrays it can be observed that the structures inside the array are significantly flatter and more uniform (a) and b) in Figure 32), even if they are significantly

smaller than the outer fence. This "morphological" fence, together with the changed patterning strategy, seems to have led to a change in the gas dynamics inside the array, which promotes uniform pad growth. The structure height after purification should be around 4 - 5 nm, thus in the area of the sputtering samples but easily distinguishable in the AFM to the substrate due to their surrounding relatives. It also shows that with increasing array size, the general structural height of the pads becomes smaller (c) in Figure 32).
Even if the structures within the arrays seem promising and reproducible, the problems that come with arrays in general are not satisfactory, which leads to a new idea that leads to the introduction of much larger FEBID gold pads.

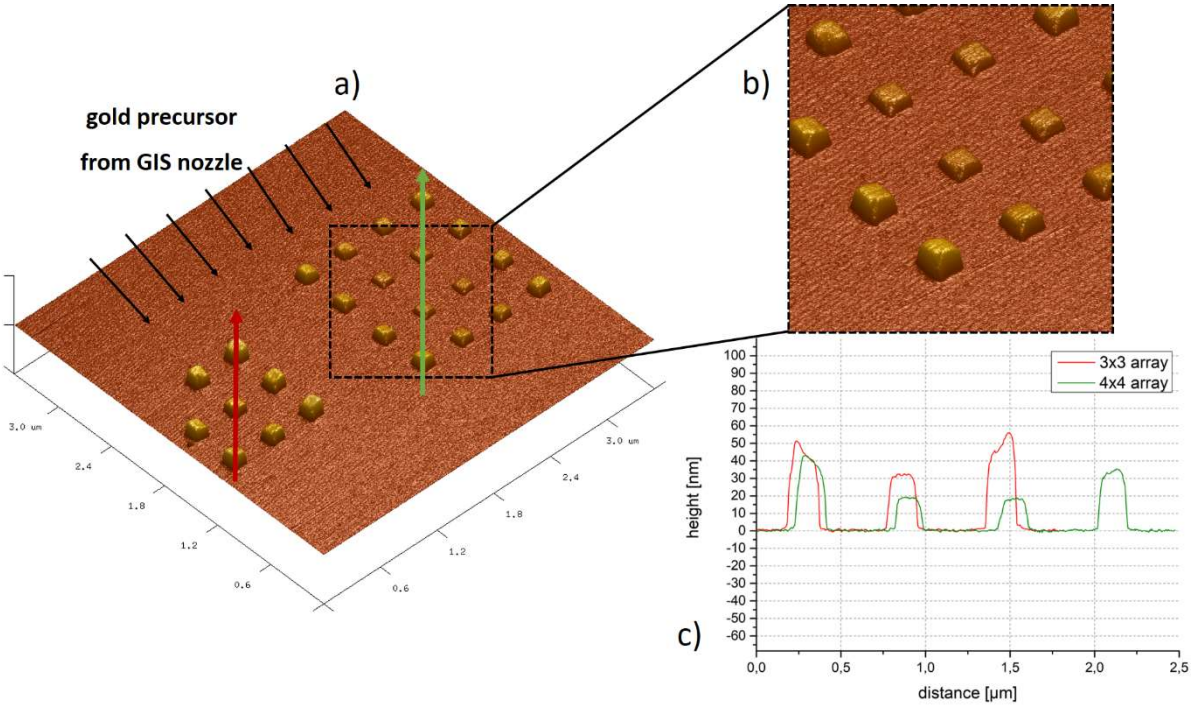

Figure 32: AFM 3D representation of an 3x3 and 4x4 pad array made with parallel patterning. ***a)*** *Image of the whole arrays with coloured arrows marking the cross sections. A pad is missing from the 3x3 array that was accidentally left unmarked during patterning.* ***b)*** *Magnification to show the almost flat and even structures in the middle of the 4x4 array.* ***c)*** *Cross sections of the drawn areas in a). On the one hand, the decreasing morphology on the inside of the outer structures can be seen (morphological fence) and the decrease of the general structure height with increasing array size.*

4.2.2 “Large” Au Pads

The change to larger FEBID gold pads with square footprints but side lengths of 1000 nm and 1500 nm are discussed in this subsection. The "bowl" shape variant is shown in Figure 33 and the "balanced" shape variant in Figure 34.

4.2.2.1 Distinctive “Bowl” Shape

To eliminate the problems that occur with serial or parallel patterning of larger arrays, the strategy came back to single pad fabrication. However, the design slightly changed as we wanted to ensure, that the entire laser spot area should be used. Consequently, the gold pad side lengths are increased from 100 nm (previously called *small*) to 1500 nm (now denoted as *large*), while maintaining its quadratic footprint.

The evaluation of this can be seen in Figure 33. In order not to vary too many parameters during the change, apart from the passes (25000) and the side length, all other process parameters were left unchanged resulting in a TET of 94 minutes. As expected, the gold pad again forms a very distinctive "bowl" shape, which is particularly noticeable in the cross section (a). This shows lateral base broadening of 50 nm on each side, in x and y direction. The height difference between the lowest point of the structure and the tips is 160 nm. On the one hand, the deposition time is very long and therefore not very practical if, for example, a large quantity of these pads is required, and on the other hand, the massive difference in height between the central parts of the structure and the edge or corner parts leads to purification problems with regard to the saturation dose. Even if the structural height were to fall below 100 nm after purification, it is not after deposition and is therefore not a classical nanostructure[3]. Based on these points, it turns out that a flat pad with a lower structural height would fit the requirements better.

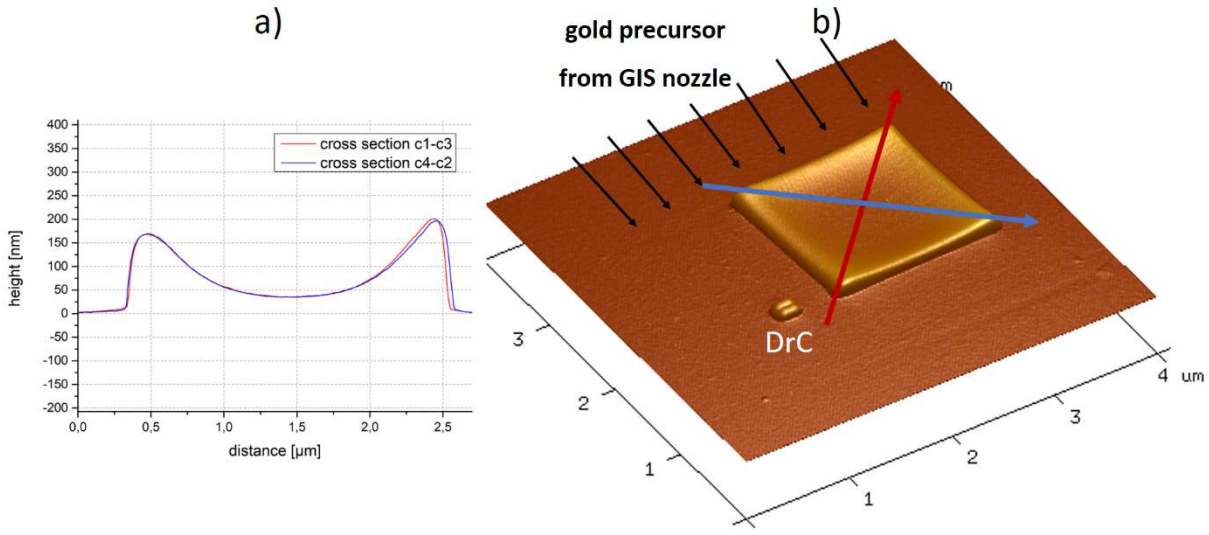

Figure 33: AFM 3D representation of a single large "bowl" shaped pad. ***a)*** *Cross section indicated by the coloured arrows. The bowl shape is clearly visible, as well as the strong difference in height within the structure. The cX values in the legend represent the corners of the structure over which the cross sections run.* ***b)*** *Image of the whole structure with the cross-section arrows and the direction of incidence of the precursor molecule. DrC marks the drift compensation field (4.1).*

4.2.2.2 Balanced Shapes

In the work of Winkler et al.[18] it was already shown that ultra-flat structures are a better choice with regard to the requirements. The desired morphology is called "balanced" and the deposition of such a structure is a matter of adapted DTs, which has been proven in mentioned work and can be seen in Figure 24. One such pad is shown in Figure 34. To obtain it, the DT must be increased from 10 µs to 1000 µs and but since the height is to remain the same, passes are reduced by the same factor from 10000 to 100. In addition, the lateral size is reduced to 1000 nm, which is still closest to the light microscope's resolving power and at the same time corresponds to the approximate diameter of the test laser. The reduced lateral dimensions obviously result in a shorter deposition time, which is ~17 minutes TET.

[3] A classical nanostructure is one in which at least one dimension is below 100 nm.

As can be seen in a), it is indeed a homogeneous and almost flat structure with a slight curvature on the top (Δz = 2.6 nm). For the lateral base broadening, there are 25 nm on each side again in x and y direction and an average height of the structure of 50 nm. The R_q value (root mean square average of height deviations) in a 500x500 nm measuring area in the middle of the pad is 0.4 nm. Structures with this geometry and morphology are easy to reproduce and have a low single-digit nm value in the height variation between the individual structures. In addition, the height of the structure is well below the required limit of the classical definition of nanostructures and can therefore be called FEBID nanostructure even if the lateral extension is more than 1000 nm. The aim of this work was not necessarily to fulfil the definition of a nanostructure, but nevertheless a promising result. In this first part of the road (Figure 20), a satisfactory morphology with a corresponding structure size was found by varying and adjusting various parameters, in particular the DT. For further steps, not only these "balanced" shape pads will be used, but also the small "bowl" variants as described in chapter 4.2.1.3.

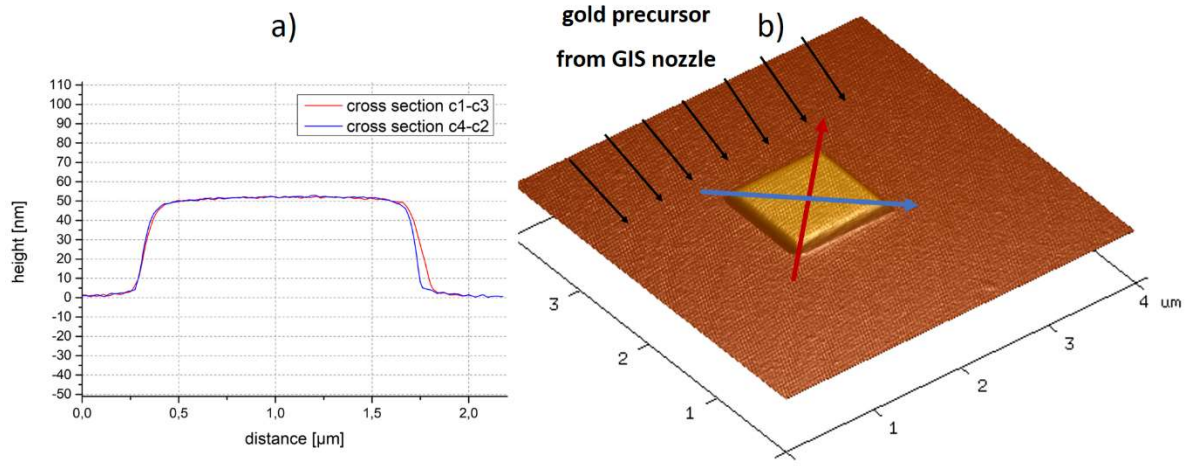

Figure 34: AFM 3D representation of a single large "balanced" shaped pad. ***a)*** *Cross section indicated by the coloured arrows. The desired flat shape at the top is clearly visible. The cX values in the legend represent the corners of the structure over which the cross sections run.* ***b)*** *Image of the whole structure with the cross-section arrows and the direction of incidence of the precursor molecule.*

4.3 Purification and Contamination

After the successful fabrication of FEBID based high-fidelity pads with homogeneous thickness across the entire footprint, we now turn towards the chemical transfer into pure gold pads. In principle, we follow our previous strategy although it requires some adaptions, which is the main content of this chapter. In order to be able to carry out the purification we again need start parameters, which here come from the master thesis of Barbara Geier.[7] Then the loss of volume of the pads after the purification, so the removal of carbon from the deposition, is examined as a function of the applied dose, both for "small" and "large" pads (4.3.1). The test molecules are applied to the purified samples to determine the plasmonic activity of the FEBID gold pads and the intensity of the Raman signal (4.3.2). The results of the Raman measurements are unexpected, and an iterative solution approach is used to find the cause of the results. The assumed causes are checked with gold sputter samples (4.3.3). The theory of carbon contamination has been confirmed and a treatment to reduce or completely remove it, is being applied to sputter and FEBID samples (4.3.4).

4.3.1 Volume Loss

The next big step on the road to plasmonic FEBID pads is purification, so the removal of carbon from the deposits to obtain pure metallic structures. The first important question that arises in the context of this investigation is how the volume loss and the morphology behave with the applied dose. Previous investigations have already been carried out by Geier et al.[19] for a platinum precursor and by Winkler et al.[6] for a gold precursor in which the procedure was adapted from Geier's master's thesis.[7] After deposition, the FEBID samples were transferred into a second DBM for purification and placed on a carrier with a Faraday cup in the middle. The procedure is also explained in more detail in 4.1. The cup was used to measure the electron beam current in the high-vacuum in order to determine the TET for the patterning engine and thus to obtain the applied dose. Although the positioning of the patterning field was done under vision with irradiating the samples as little as possible, the actual purification was done blindly and the results first became visible by AFM examination.

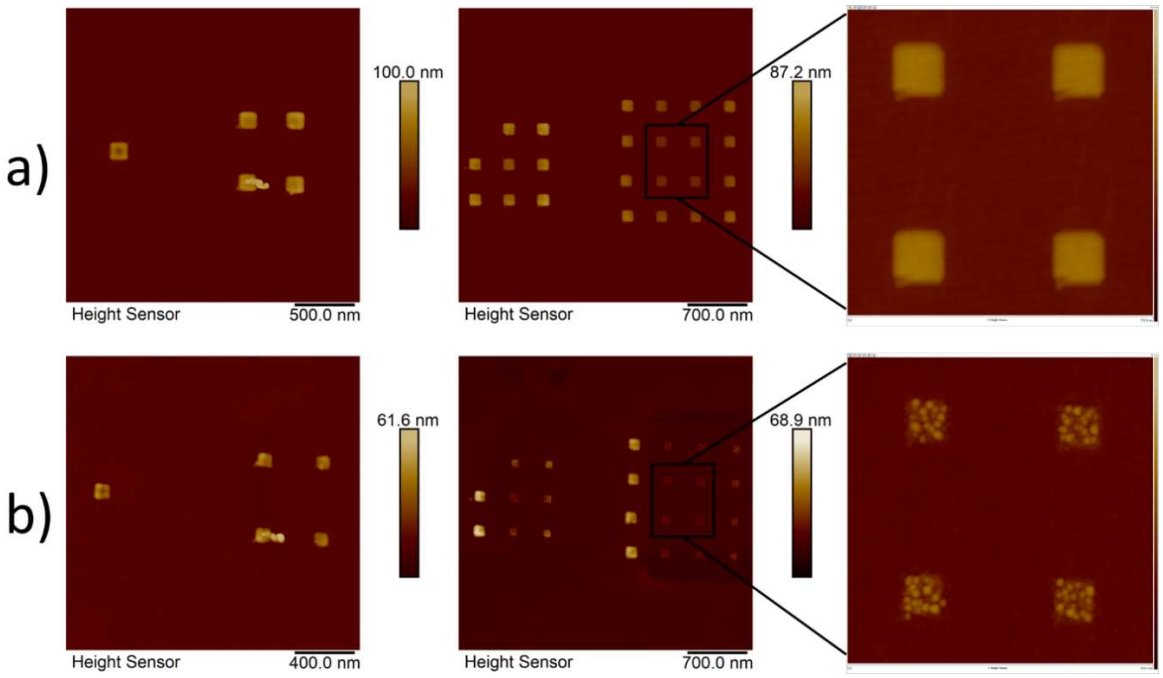

Figure 35: AFM images of "small" Au FEBID pads produced via serial patterning. ***a)*** *Gold pads as deposited.* ***b)*** *Gold pads after purification with a dose of 40 C.cm^{-2}.*

Information about purification parameter are taken from Geier's thesis [7], resulting in a value of 5 keV for the accelerating voltage, a beam current of 5.5 nA, a DT of 1 µs, a PoP of 10 nm and a dose of 40 C.cm^{-2}. The purification curtain is made at a pressure of 30 Pa under ambient conditions. Gold pads that undergone such a purification can be seen in Figure 35 as 2D image and in Figure 36 as 3D representation. These pads were treated in the O_2 plasma cleaner for an additional hour after purification but before AFM examination. This AFM overview shows the arrays before (a) and after purification (b). While the left images always show a single pad and a 2×2 array, the center images give a 3×3 and a 4×4 array, to visualize the dependency of the position of the pad within the array in relation to the structure height and morphology. The 2D height images at the right give a closer look to the 4 inner pads of the 4×4 array, as they revealed the most homogeneous morphology compared to the outer fence structures (see center images). The morphological variation due to the strong carbon loss is clearly evident but also surprising in its characteristics when comparing them to Geier's results.[7]

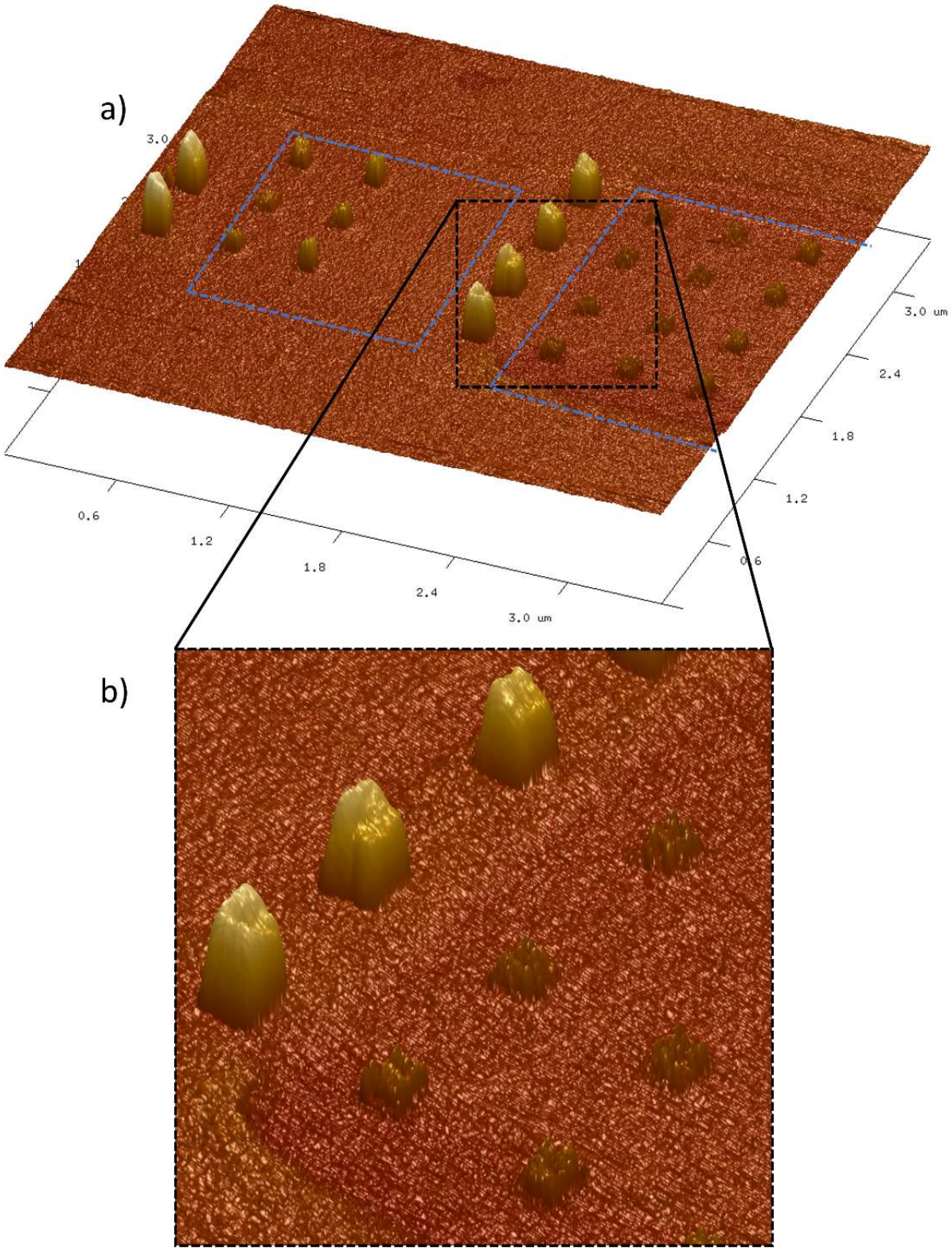

Figure 36: AFM 3D representation of partially purified "small" Au FEBID pads produced via serial patterning. ***a)*** *Here you can see the 3×3 and 4×4 array. Please note that due to a shift of the F7 window, the whole left part of both arrays has been omitted in the purification process and thus a good impression of the size ratios before and after purification can be reproduced on just one sample. The purification area is indicated by* ***blue dashed lines****.* ***b)*** *Zoom in on an area where non-purified (three pads top left) and purified pads are right next to each other, which reveals the massive volume loss.*

In these results it was noted that the structures retain their original footprint and are pore- and crack-free. In a direct comparison of the two AFM images on the right in a) and b), the original footprint is indeed preserved, but the gold grains are clearly visible in b), which proves the changed morphology after purification. The structures in the 2×2 array only show a volume reduction of 52±5 %. The dose of 40 $C.cm^{-2}$ was thus too low for an as deposited height of 55±6 nm, resulting in a partially purified structure. In the third and fourth array, so in the two in which a difference in height between the inner and outer structures as well as morphological changes are already visible, the volume reduction of the inner structure of the 3×3 array is 75±2 % at an initial height of 32±2 nm while one purified pad of the fence has an initial height of 50±5 nm and a volume reduction of 60±5 %. In the 4×4 array, the initial height of the flat structures is 19±1 nm and the volume loss 73±2 %, while again a purified pad at the edge has a loss of 72±2 % with an original height of 36±2 nm. Since the dose was the same for all pads, the difference in the volume distribution after purification of the individual pads can be attributed to height variation between the individual arrays but also within a collection of structures. Even if it seems obvious, it should be mentioned at this point that the saturation dose, which is necessary to get a structure completely free of carbon, is therefore dependent on the original height of the pads. This unfortunately shows another problem with arrays that have structures that are almost identical in lateral dimensions but have a strong variation in structure height depending on the array size and the position of the pads within an array.
However, since arrays larger than 2×2 already have strongly varying values for the pad height, in case the saturation dose was used for the inner structures, the edge structures will only remain as partially purified. If a dose is used that also fully purifies the significantly larger edge structures, also known as the morphological fence, the inner flat and even structures will also show the necessary volume reduction, but they will then be over-purified and contamination or structural changes could be the result. With larger arrays, the inner and outer structures seem to converge in the initial height, which is visible in the values between the 3×3 and 4×4 array.
Due to the fact that there can be large differences in the volume loss of the individual pads within an array and that their small footprint leads to a lower shape stability (e.g.: promoted delamination) compared to the substrate, the approach with the larger pads is used again in order to circumvent the problems already mentioned.
For the further volume reduction vs. dose investigation, the "large" gold pads are now used. Since in the meantime the possibility has arisen to fall back on new purification parameters of another work,[44] which have proved to be promising. An excerpt can be found in Figure 37.

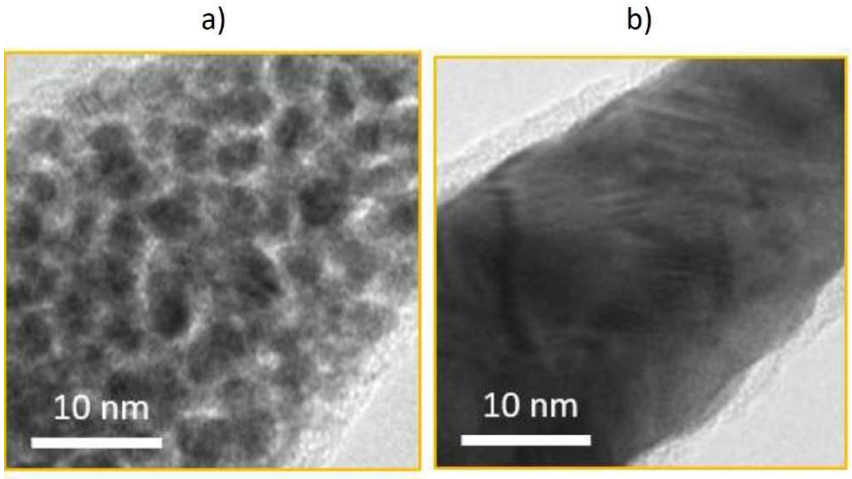

Figure 37: TEM images of a FEBID gold nanopillar. ***a)*** *As deposited.* ***b)*** *After purification with 30 keV, 8.7 nA and 80 Pa H_2O atmosphere at room temperature. The figures are taken from a recent publication by Kuhness et al. with permission of the authors for internal use.*[44]

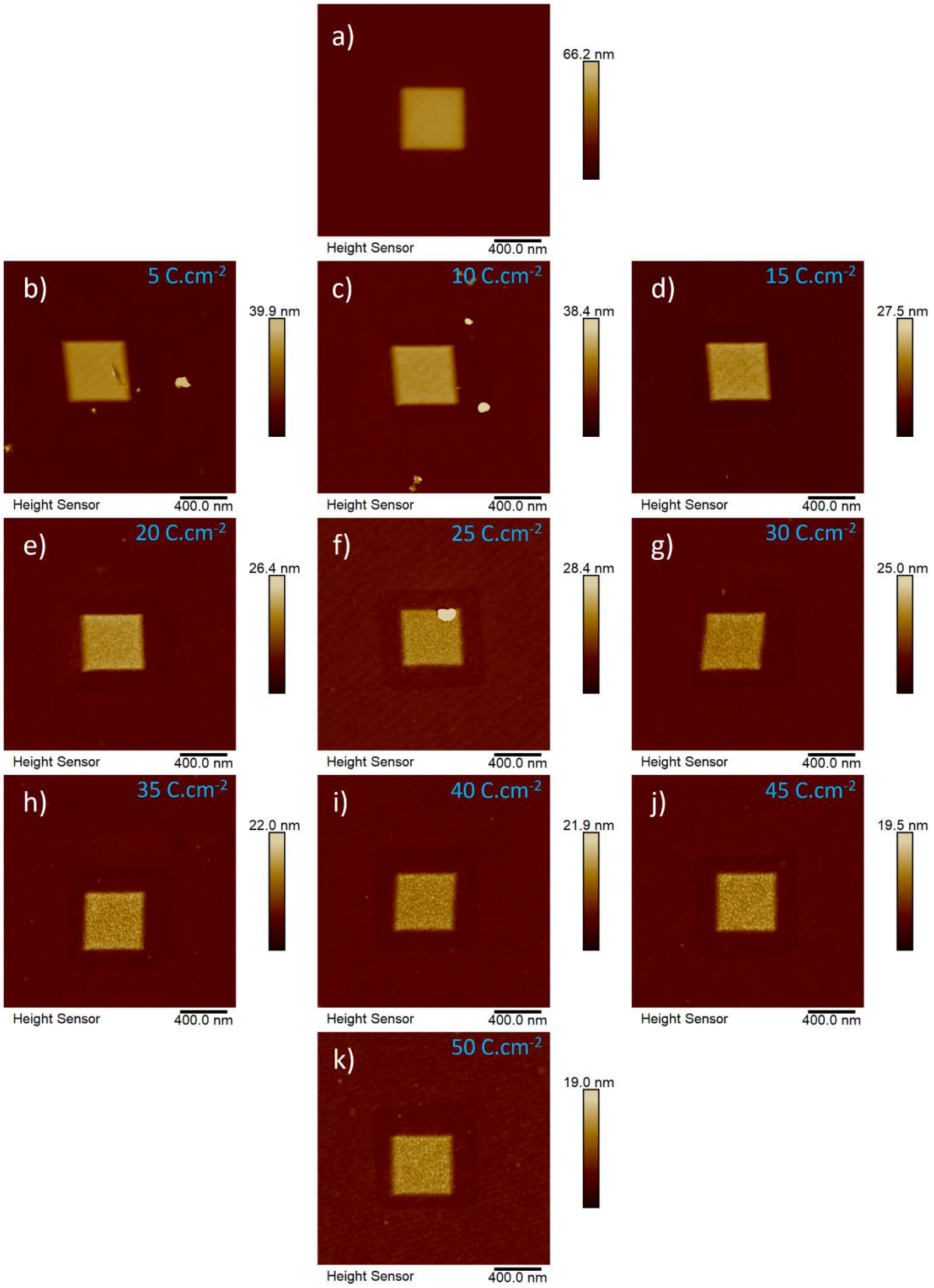

Figure 38: AFM images of "large" gold FEBID pads. ***a)*** *Pad as deposited with 50 passes.* ***b) to k)****: Purified pads with different doses applied: b) 5 C.cm⁻², c) 10 C.cm⁻², d) 15 C.cm⁻², e) 20 C.cm⁻², f) 25 C.cm⁻², g) 30 C.cm⁻², h) 35 C.cm⁻², i) 40 C.cm⁻², j) 45 C.cm⁻², k) 50 C.cm⁻².*

In this mentioned study, the purification of FEBID pillars was complemented by a TEM analysis. In the TEM image of the as deposited structure (a), the gold grains (dark areas) are embedded in a carbon matrix (light areas). In the image after purification (b), the gold grains are now very tightly packed and the matrix has disappeared. However, a bright area is now visible on the outside of the pillar, which has been identified as a carbon contamination layer. This could make it difficult or impossible for a molecule to chemically bind to the gold grains if a FEBID structure is completely covered. More details on this can be found in section 4.3.3.
The following parameters are now used for the purification of the “large pads”: 30 keV acceleration voltage, 8.7 nA initial beam current, 7 nm PoP, 1 µs DT. The purification curtain is made at a pressure of 80 Pa under ambient conditions. In order to be able to use a larger number of pads for a more extensive investigation, the side length is reduced to 500 nm and 50 passes compared to 1000 nm and 100 passes in chapter 4.2.2.2, which reduces the TET to ~2 minutes, but still corresponds to five times the size of a "small" pad. This sufficiently large footprint provides the necessary shape stability. The structural height of the as deposited pads is 35 nm. The doses ranged in 5 - 350 $C.cm^{-2}$ and a section of these can be seen in Figure 38. The first AFM image (a) shows a FEBID gold pad directly after deposition, whereas the remaining images (b-k) show comparable pads after purification with different doses starting at 5 $C.cm^{-2}$, ascending in steps of five, up to 50 $C.cm^{-2}$.
A close examination of the images shows that there is a transition from an even, coherent surface to a rough, gold pad with the rapid formation of growing gold islands. This appearance is similar to a gold sputter probe, but with the advantage that the basic structure of the pad is preserved and it is a surface-selective process. Since the carbon freedom of the structures is determined on the basis of the volume loss, the determination of the saturation is particularly desirable. In Figure 39.a), the saturation curve of FEBID gold pads from Figure 38 can be seen. Since it is known that one can speak of carbon-free structures from a volume loss of 77 %, we can say that this value is reached around 30 - 35 $C.cm^{-2}$ for these structures. It is difficult to compare the volume loss with other works using the same purification technique, as the conditions are very different. In the work of Geier et. al.[19] the FEBID structures showed a volume loss of ~70 %, but these were made from a platinum and not a gold precursor, which have a different carbon content. In the work of Kuhness et. al.[44] only ~50 % was achieved although the same gold precursor was used as in this work, but instead of pads, pillars were deposited with a width of 300 nm and a height of ~1.7 µm were purified, resulting in a partially purified pillar. The values for the roughness of the pads were all determined from a 200×200 nm area in the centre of the pads and can be seen in Figure 39.b). In the area of interest (green field) the highest R_q value (root mean square average of height deviations) of 1.2 nm is obtained for a dose of 35 $C.cm^{-2}$. At higher doses up to 50 $C.cm^{-2}$ the R_q drops again, which can be explained by ripening, but for significantly higher doses (> 100) an increase is again visible, which can be explained by higher electron irradiation and associated cracks and delamination.
Even if the “small” pads can provide the necessary volume reduction, the choice of a dose value for a whole array is a difficult matter and not to be preferred. The “large” pads have been found to be much more practical in terms of purification, pointing to the highest roughness value at the appropriate volume loss. Although the “small” pads will still prove useful in detecting molecules (chapters 4.4.1 and 4.4.2), the focus from here on is on the “large” ("intermediate") pads.

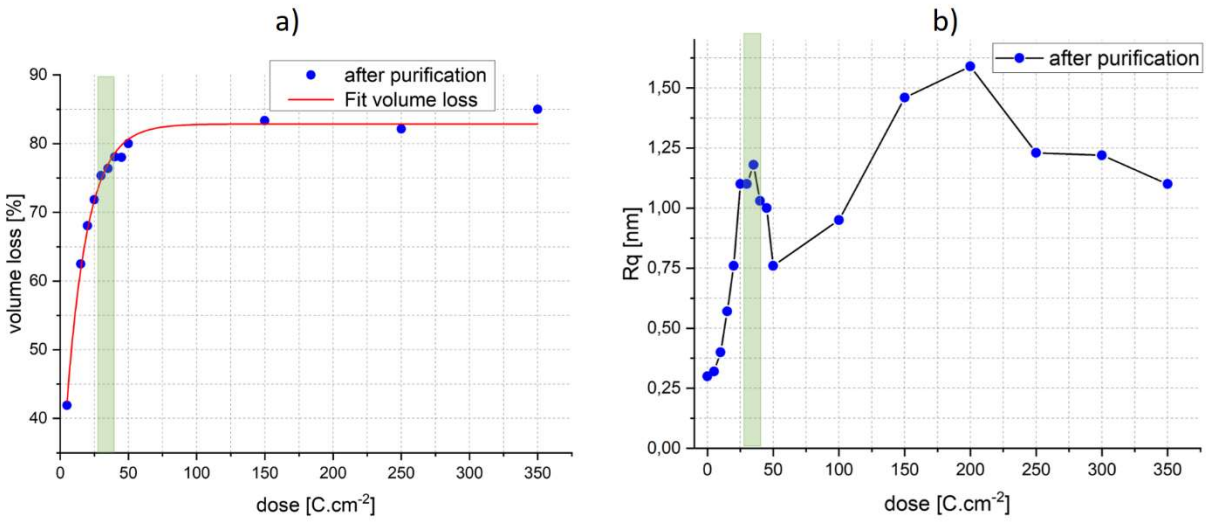

Figure 39: Volume loss and roughness curve of FEBID gold pads with 50 passes and 500 nm in lateral dimensions. ***a)*** *Saturation curve of the volume loss vs. dose study. The* ***red line*** *is a fit of the exponential volume loss of the pads with respect to the applied dose, described by* $y = ae^{-x/t} + y_0$. ***b)*** *Roughness curve of the volume lost vs. dose study. The semi-transparent* ***green field*** *marks the area of interest with regard to volume loss in a) and b).*

4.3.2 Raman Signal

The central question of this work is whether purified FEBID structures are suitable as SERS active substrates. In order to be able to make an additional statement between the Raman signal and the purification dose, the FEBID samples from 4.3.1, which were subjected to a volume reduction vs. dose study (5 - 350 C.cm^{-2}), are used for this purpose. In this way, we can assign the gold pads with a certain purification dose their own plasmonic response in the form of a Raman spectrum and thus say more about their performance and comparability with gold sputter samples.
The FEBID samples, together with a gold sputter sample as a reference, were immersed in a 10^{-4} molar solution of 4-MBT for one hour and then air-dried. In the meantime, the Raman microscope was prepared and, after drying, the samples were irradiated with the laser.
The corresponding measurement can be seen in Figure 40. The Raman spectrum of the gold sputter probe (a) shows the clear and strong signal fingerprint of the molecule. The strongest peaks, which are also relevant for the calculation of the EF, are marked with arrows. The FEBID samples (b), on the other hand, unfortunately show unexpected behaviour. None of the gold pads, regardless of the purified dose, shows a plasmonic response in the form of a Raman signal of 4-MBT. Although it was expected that samples well below and above the saturation dose should show different signal strengths, this result is surprising. Due to the reference measurement in a), problems with the molecular solution can be excluded, as all samples were in the same vessel.
Since previous investigations have shown that at least part of the gold pads within their own structures must be carbon-free and thus the plasmonic should not be suppressed, there must be an explanation for this behaviour. There was already a presumption (see chapter 4.3.1) of a possible external carbon contamination of the structures due to the electron beam assisted purification. It is now hypothesised that this is the reason why the signal effect is drastically reduced. In order to confirm this assumption, further investigations on gold sputter samples will be carried out in the next section.

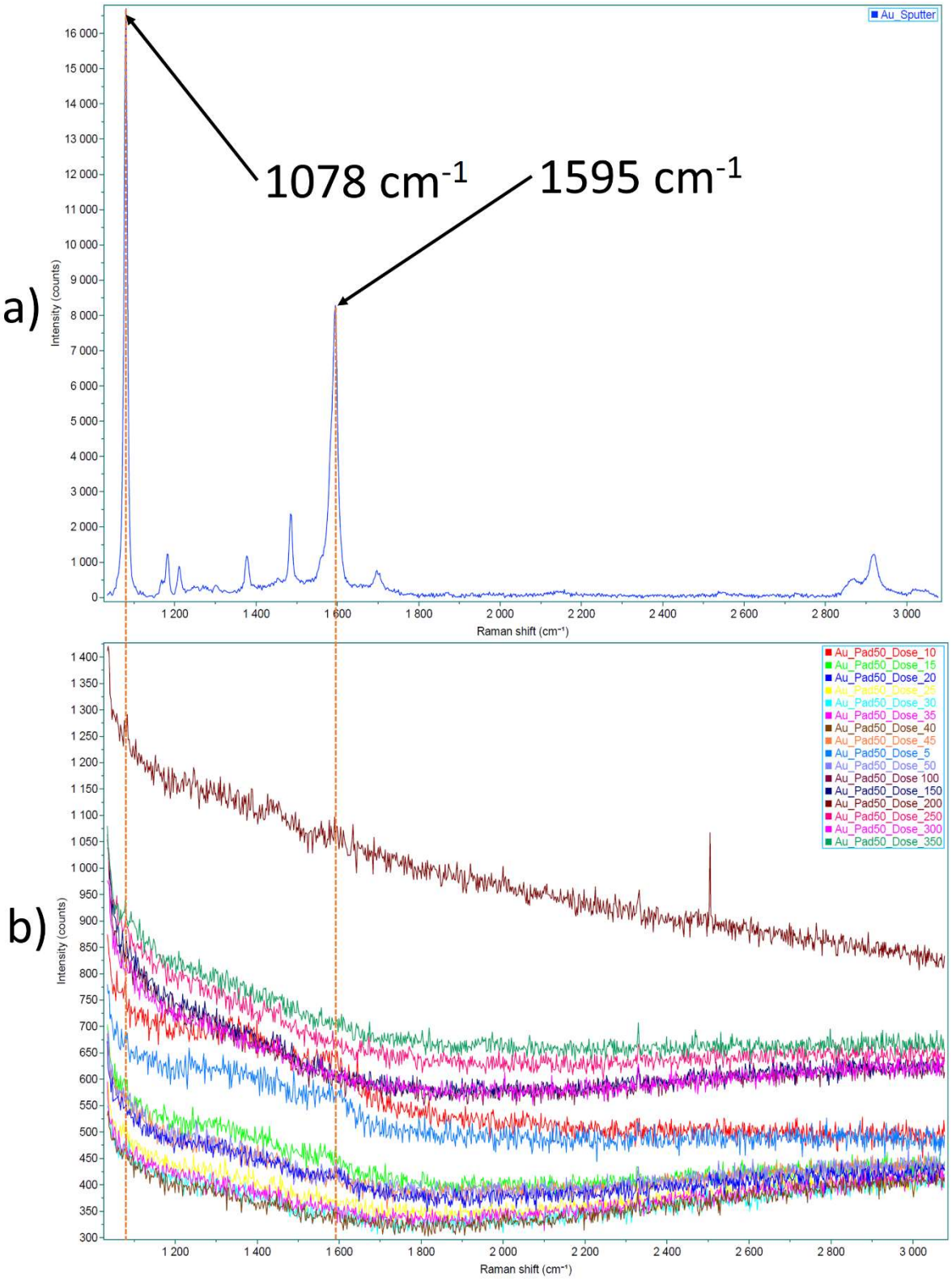

Figure 40: Raman spectra for gold sputter and FEBID samples; a) Raman spectrum of a pure gold sputter sample wetted with a 10^{-4} molar solution of 4-MBT, the characteristic peaks of the molecule are clearly visible. b) Several Raman spectra of FEBID gold pads purified with different doses and subsequently wetted with 4-MBT, no traces of the molecule are visible in the Raman measurement. The expected peaks were marked with semi-transparent orange markers.

4.3.3 Influence of Contamination

To confirm the suspicion of carbon contamination, a series of tests (a) in Figure 41) is carried out with gold sputter samples in which the influence of other sources is also investigated. For this purpose, a wafer with a pure gold sputter layer is produced as a known and functioning initial sample. As a second sample, another wafer is supplemented with FIB window labelling, as used to find the FEBID structures under the light microscope. It is important to note that the FIB marking must be carried out before gold sputtering, otherwise the redeposition by the silicon during ion milling will almost completely contaminate the desired area. On the third sample, in addition to the marking and gold sputtering, various known purification doses are now applied, as they are also used for the FEBID gold pads. The last sample contains all the previous steps and additionally one hour of O_2 plasma cleaning to investigate whether these steps actually remove the contamination.

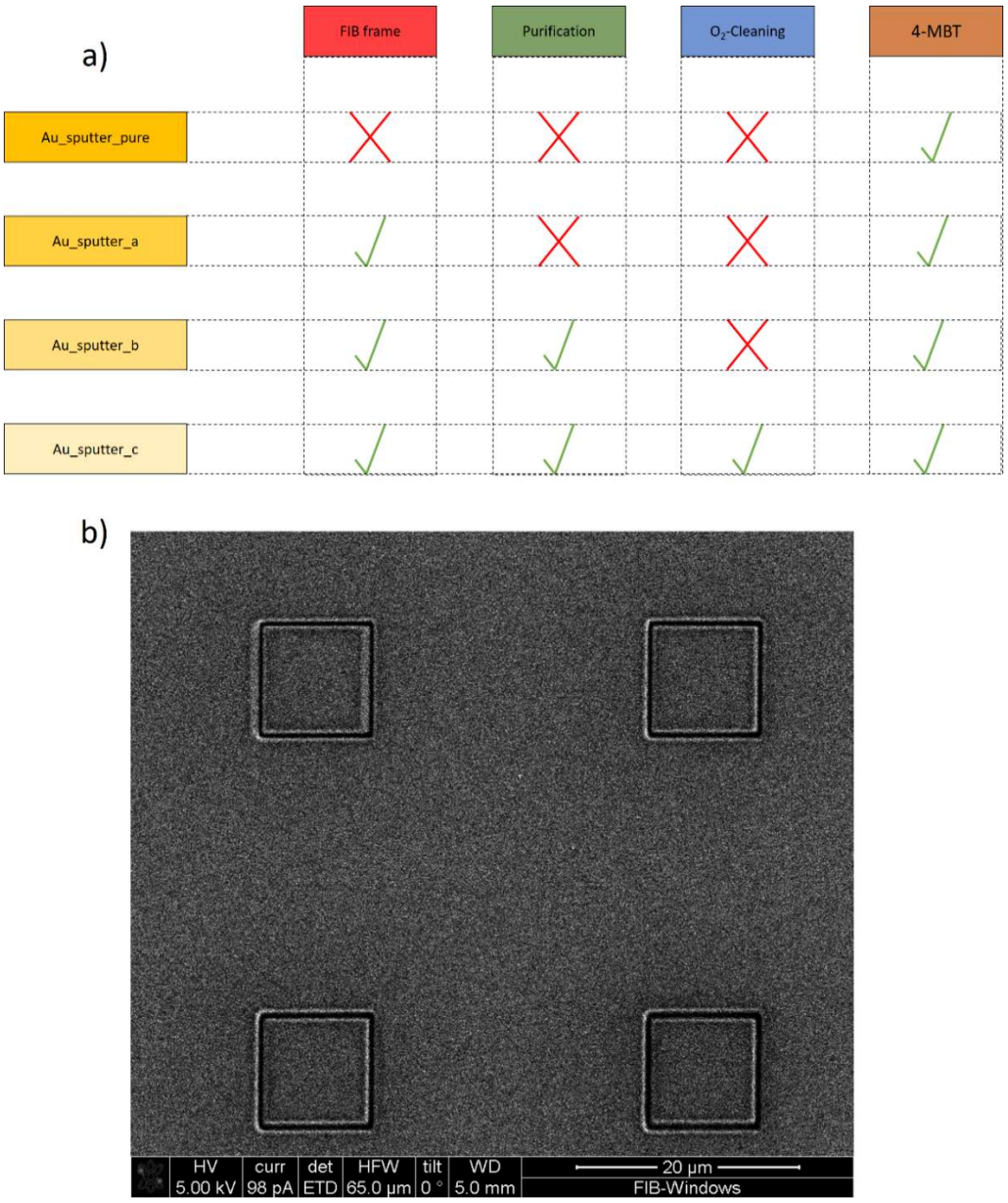

Figure 41: Test series and FIB frame. ***a)*** *Graphical representation of the test series with the gold sputter samples. Tick marks indicate the steps applied per sample.* ***b)*** *SEM image of an array of FIB frames. The processing steps and measurements were carried out in the inner area of the frames.*

All four samples are finally placed in the same vessel for one hour with the 4-MBT molecule solution in order to eliminate possible problems in the preparation of the solution. After drying, the samples were measured in the Raman microscope. Part of this investigation can be seen in Figure 42 by means of a representative spectrum for the individual samples. What can be seen even better in Figure 43 is that the peak intensities for the unprocessed sample and the sample with the FIB marking correspond to expectations. For the sample with the purification dose of 40 C.cm^{-2}, the signal deterioration is clearly visible. The molecule is still measurable but a clear carbon shoulder has formed, which can only come from the electron beam assisted purification. A significant improvement of the signal or reduction of the contamination could not be achieved with plasma cleaning.

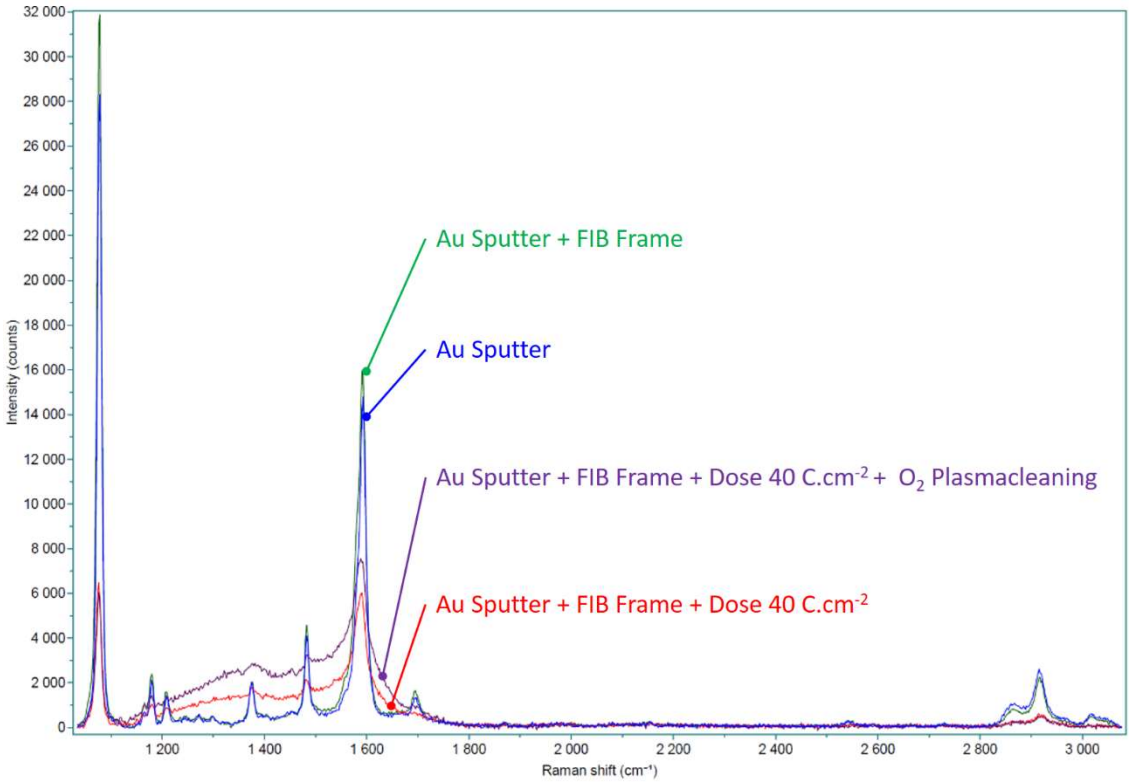

Figure 42: Raman spectra of different gold sputter samples. Blue: Spectrum of pure gold sputter sample. Green: Spectrum of pure gold sputter sample with pre-milled FIB markers. Red: Spectrum of a pure gold sputter sample with pre-milled FIB markers and an applied purification dose of 40 C/cm². Violet: Spectrum of a pure gold sputter sample with pre-milled FIB labels and an applied purification dose of 40 C/cm² and a one-hour O_2 plasma cleaning treatment.

As already shown in 4.3.1 by the measurements of Kuhness et al.,[44] a carbon layer forms on the FEBID samples after purification. Based on these investigations, it can now be confirmed that this is also the case here and that our purification treatment leads to a drastic loss of signal on the FEBID samples. Although the Raman signal is still measurable in the sputter samples, it is already significantly worse. Furthermore, plasma cleaning with pure oxygen has no significant effect on the signal quality and is therefore unsuitable for removing the contamination. *However, since a signal is measurable, not all particles can be covered by carbon, which, consequently, must also hold for the FEBID samples, although this effect is apparently stronger there.* Therefore, it is important to find a way to remove the carbon and an alternative treatment must be sought, which will be explained in the next section.

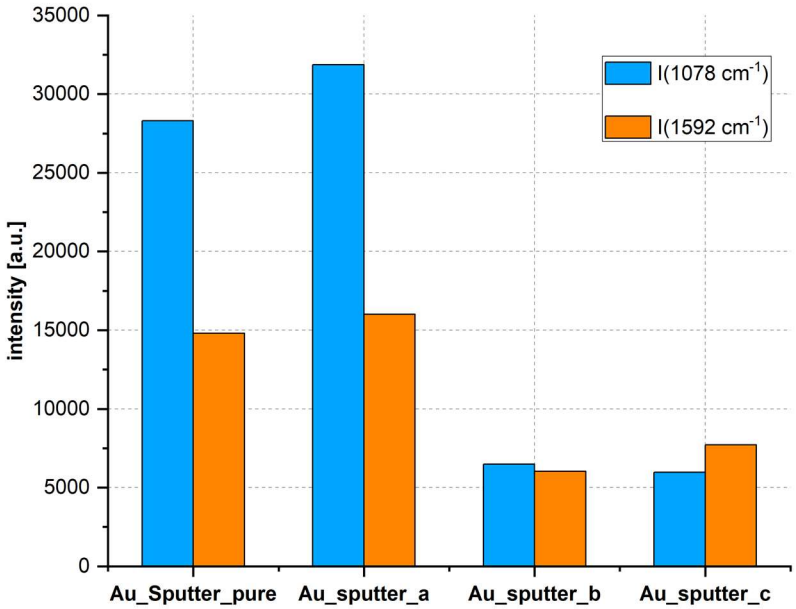

Figure 43: Bar plot of the plasmon peak intensities relevant for the calculation of the enhancement factor. ***Au_Sputter_pure:*** *Intensities of the pure gold sputter sample.* ***Au_Sputter_a:*** *Intensities of the pure gold sputter sample with pre-milled FIB markers.* ***Au_Sputter_b:*** *Intensities of the pure gold sputter sample with pre-milled FIB markers and an applied purification dose of 40 C.cm^{-2}.* ***Au_Sputter_c:*** *Intensities of the pure gold sputter sample with pre-milled FIB labels and an applied purification dose of 40 C.cm^{-2} and a one-hour O_2 plasma cleaning treatment. The test scheme can be seen in Figure 41.*

4.3.4 Contamination Reduction Attempt

As shown in the previous section, we have proven that our purification process can entail a thin, but plasmonic performance reducing carbon layer. In this section, we evaluate the post-formation removal via FIB processing. As already mentioned, this carbon film is responsible for the drastic signal reduction, but it is possible that this coverage is not homogeneous and thus gold grains can always be free, to which a chemical bond of the molecule is possible and a signal contribution is possible. In order to increase the proportion of free gold particles, an attempt is made to remove parts of the carbon layer with ion milling and expose pure gold.

For this purpose, a pure gold sputter sample is prepared as a reference and another sputter sample with FIB frames, which are irradiated with doses between 10 and 70 C.cm^{-2} and then bombarded with gallium ions using the reduced area, fast scan window (F7 window) with a single pass. Plasma cleaning is not used, as it has proven to be of no benefit. The parameters chosen for the ion milling are 30 keV accelerating voltage, 1 pA beam current and 3 nm PoP. For DT, 300 ns (Figure 44) and 100 ns (Figure 45) are used to see if they make a difference in the reduction experiment. The samples were immersed in the molecular solution once before and once after ion milling and measured with the Raman microscope. The two strongest peaks at 1078 cm^{-1} and 1595 cm^{-1} were measured for all doses before and after ion milling and mapped in Figure 46.

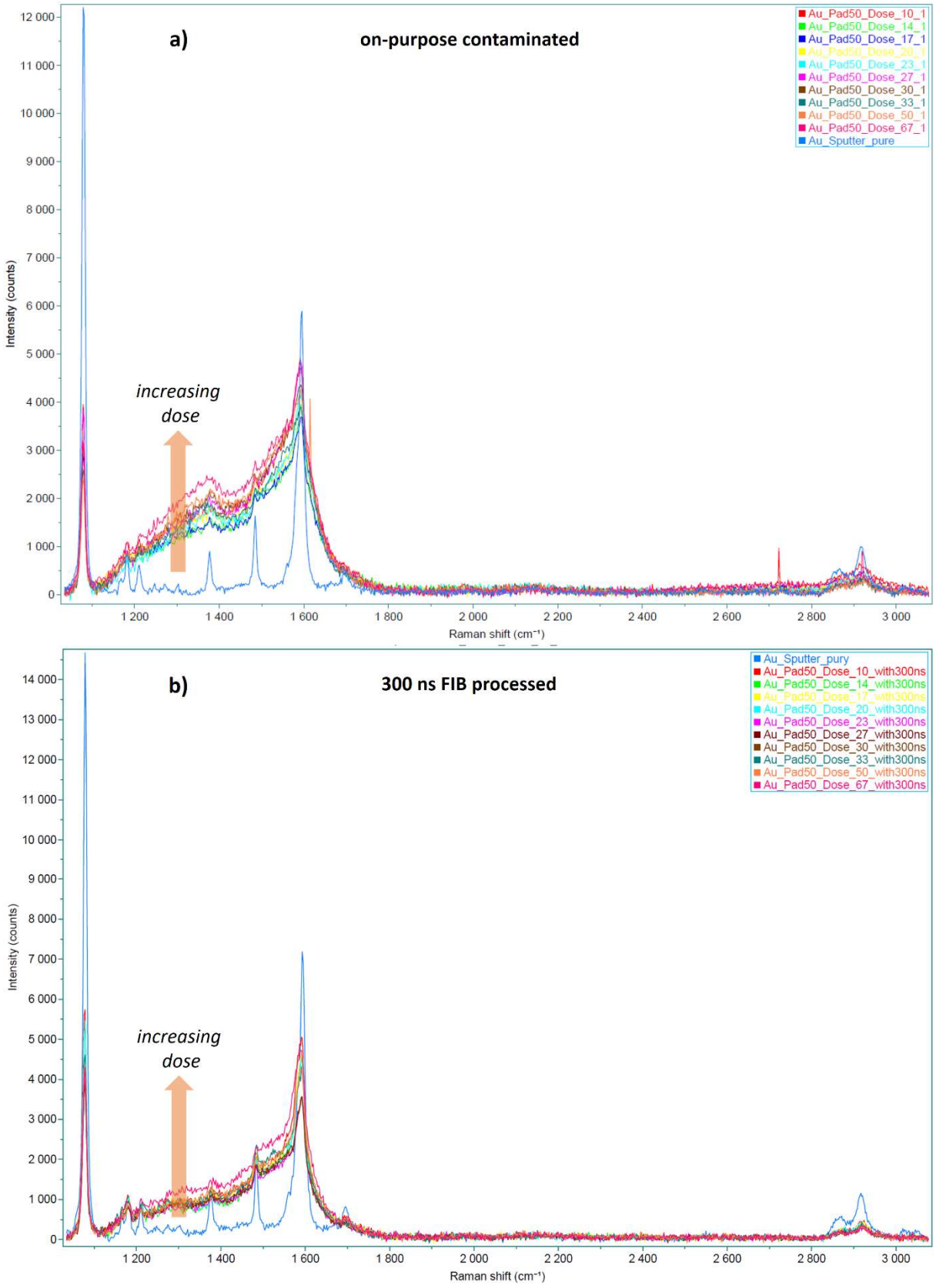

Figure 44: Raman spectra of the pure gold sputter samples. ***a)*** *Spectra of the reference sample (Au_Sputter_pure) and the areas applied with different purification doses on the processed sample.* ***b)*** *Spectra of the reference sample (Au_Sputter_pury) again, but now with the same areas on the processed sample with 300 ns DT ion milling. Intensity vs. dose graph in Figure 46.a).*

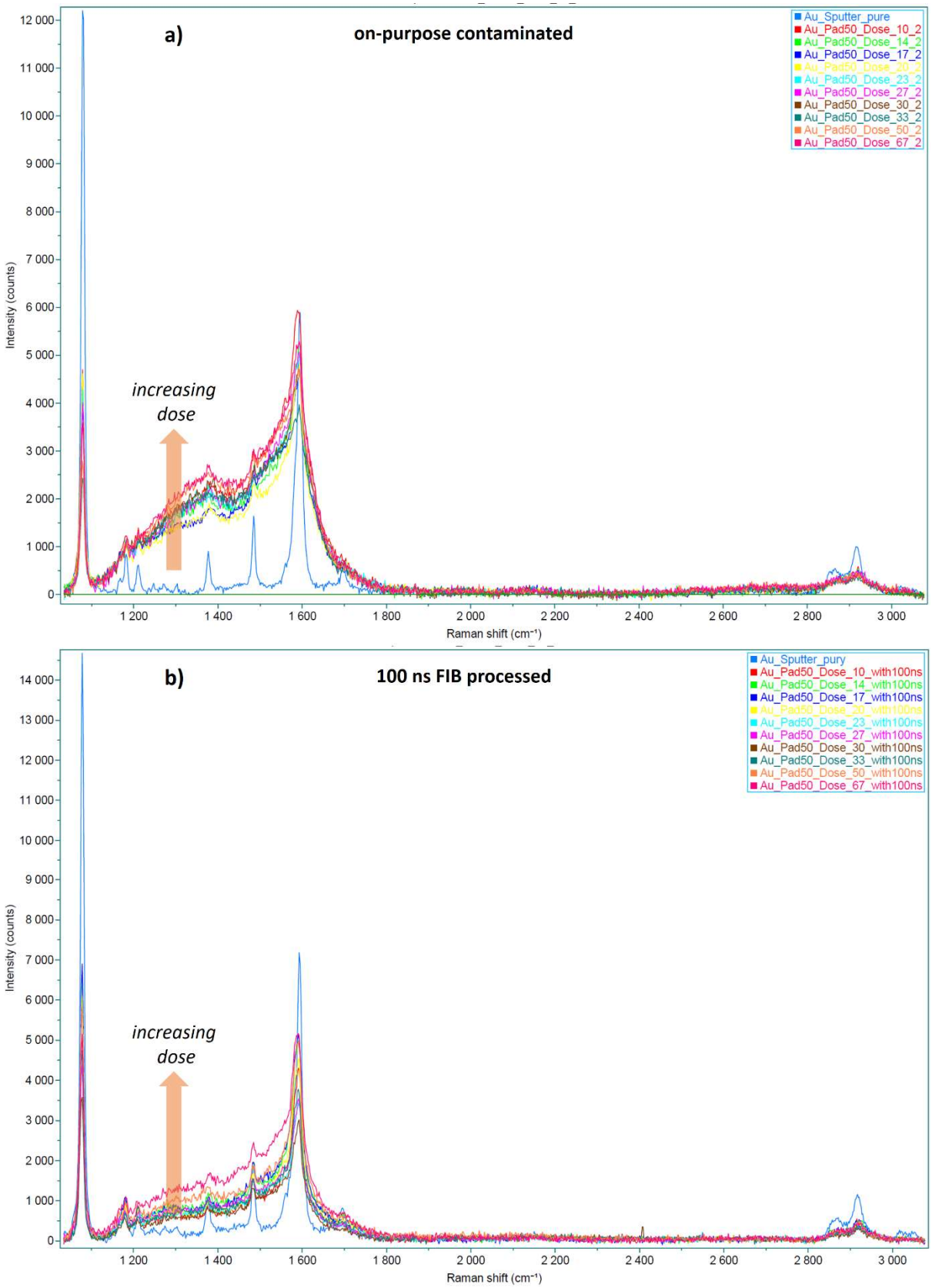

Figure 45: Raman spectra of the pure gold sputter samples. ***a)*** *Spectra of the reference sample (Au_Sputter_pure) and the areas applied with different purification doses on the processed sample.* ***b)*** *Spectra of the reference sample (Au_Sputter_pury) again, but now with the same areas on the processed sample with 100 ns DT ion milling. Intensity vs. dose graph in Figure 46.b).*

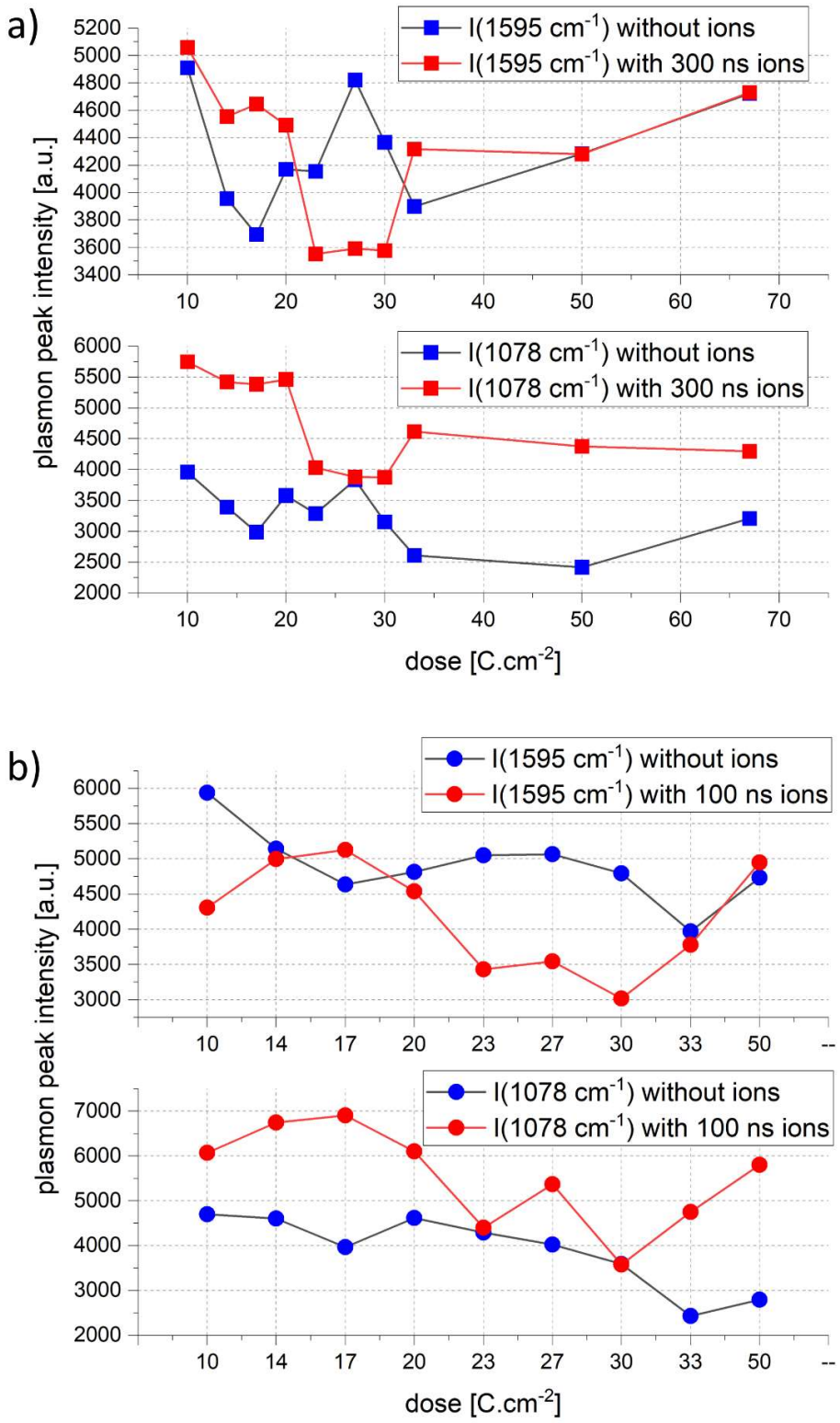

Figure 46: Plasmon peak intensities relevant for the calculation of the enhancement factor as a function of purification dose and ion milling for gold sputter samples. ***a)*** ***Blue squares*** *for the intensity of the plasmonic response with contamination without ion milling and* ***red squares*** *of the same after ion milling with 300 ns DT corresponding to Figure 44.* ***b)*** ***Blue Circles*** *for the intensity of the plasmonic response with contamination without ion milling and* ***red circles*** *of the same after ion milling with 100 ns DT corresponding to Figure 45. Please note that due to a measurement error, the corresponding values are missing from the graphs in b) and therefore the dose scales are shorter.*

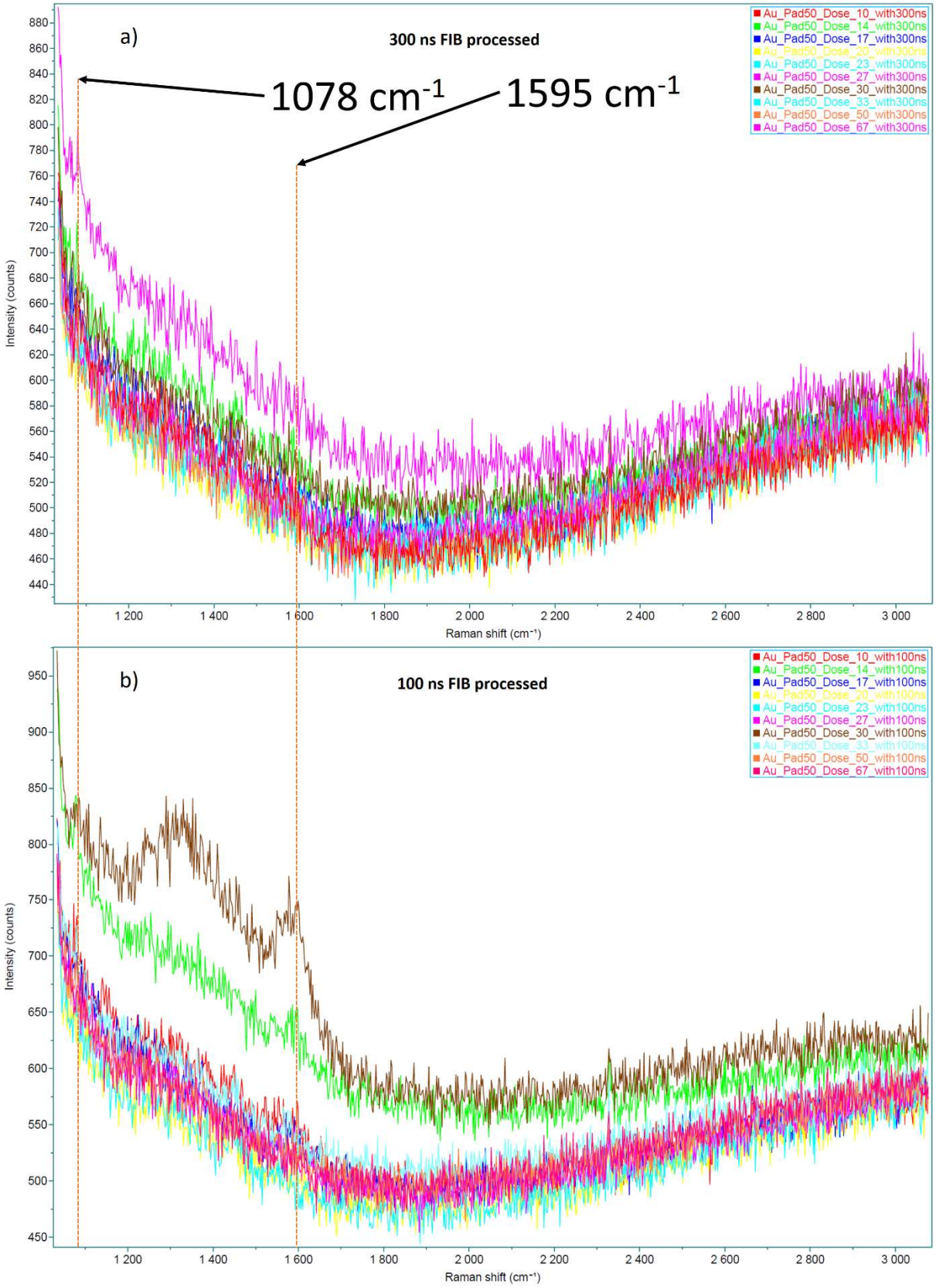

Figure 47: Raman spectra of milled FEBID gold pads. ***a)*** *Spectra of FEBID gold pads with various purification doses applied and with 300 ns DT ion milling.* ***b)*** *Spectra of FEBID gold pads with various purification doses applied and with 100 ns DT ion milling. The expected peaks were marked with* ***orange*** *markers.*

FEBID gold samples were exposed to the same purification doses and also treated with 300 ns and 100 ns ion milling. The Raman spectra are shown in Figure 47. A closer look at Figure 44, Figure 45 and Figure 46 shows that the contamination reduction attempt with ion milling can indeed reduce the carbon contamination and that a shorter dwell time is obviously advantageous for the signal quality. What influence the implantation of gallium ions in the sputter and FEBID samples has, for example the change in the dielectric constant, cannot be said at the moment. A similar result could not be achieved for the FEBID sample. Although a weak peak at 1078 cm^{-1} can be measured at 27 $C.cm^{-2}$ (300 ns DT milling) and 14 $C.cm^{-2}$ (100 ns DT milling), the remaining measurements remain without plasmonic response. Whether this improvement was actually caused by the ion bombardment cannot be confirmed beyond doubt, but what can be said with increased probability is, that electron beam assisted purification very likely leads to additional contamination and this has a dramatic effect on the Raman resp. SERS signal.

4.4 Measurement of Plasmonic Response (SERS)

The last chapter of the results section deals with the final part of the road to plasmonically active nanostructures, namely the successful measurement of the SERS signal (Figure 20). For this purpose, the “small” pads but also the pads from 4.3.1 are used, which with a side length of 500 nm could be described as “intermediate” pads, but for the purposes of simplicity are assigned to the “large” pads.

In the first part, the plasmonic activity of the FEBID structures is detected on the “small” pads using methylene blue and the response is compared with the signal of the surrounding substrate (4.4.1).

Subsequently, the molecule 4-MBT, which is much more difficult to detect than methylene blue, is also applied on the "small" FEBID gold pads and the enhancement factor is determined (4.4.2).

Since the signal on the "small" pads is very weak and could not be detected on the "large" pads, the hoped-for enhancement of the Raman signal for 4-MBT is finally measured due to a new preparation strategy for wetting and sample resting (4.4.3).

Due to their size, the FEBID gold pads cannot be seen in the light microscope of the Raman spectrograph and therefore it is being worked out how the signal enhancement and the mapping function of the instrument can be combined (4.4.4).

4.4.1 Proof of Presence of Methylene-Blue

In the previous section it was shown that a thin carbon layer on the FEBID pads drastically reduces the signal strength. However, the fact that the structures cannot be completely covered by carbon is proven in this chapter.
The detection of methylene blue is the first indication that the FEBID gold structures are plasmonically active and amplify the Raman signal due to SERS. For this purpose, "small" FEDID gold pads, which were deposited using the parallel patterning technique, which are described in sections “Small” Au Pads 4.2.1 and 4.3.1, are immersed in a 10^{-4} molar solution of methylene blue for one hour. Then held in distilled water for ten seconds and pre-dried with the CO_2 spray. An SEM image of the sample area can be seen in Figure 48. The blue dashed

area shows the array that can be seen again on the AFM images in Figure 49. The blue arrow points to the region from which the Raman signal originates from the FEBID structures, while the red dashed line indicates the zone from which the measurement on the substrate is taken (Figure 50).

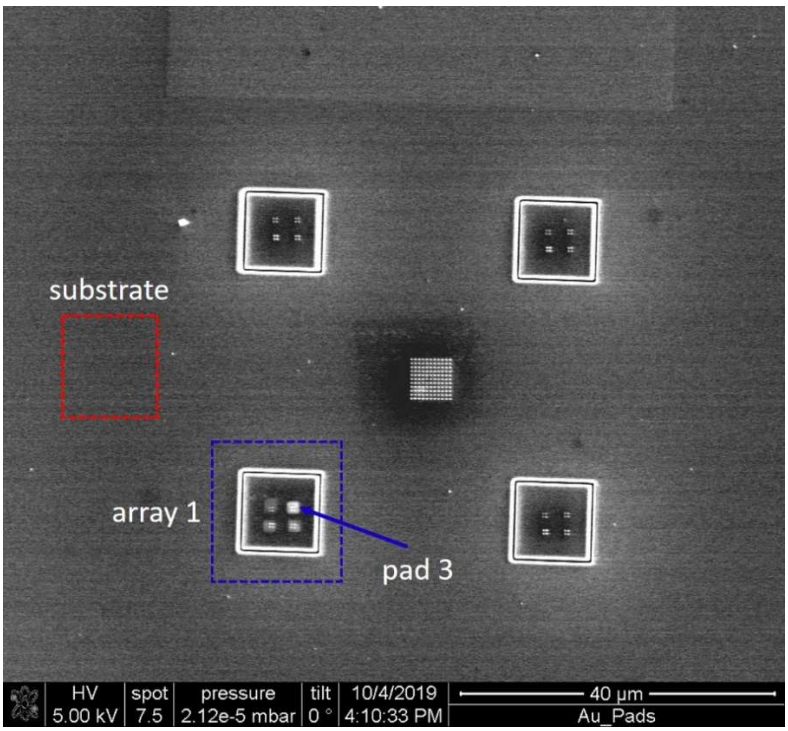

*Figure 48: Sem image of sample area. **Blue dashed window**: Array of gold pads responsible for the SERS signal. **Red dashed window**: Area of the Raman measurement on the substrate.*

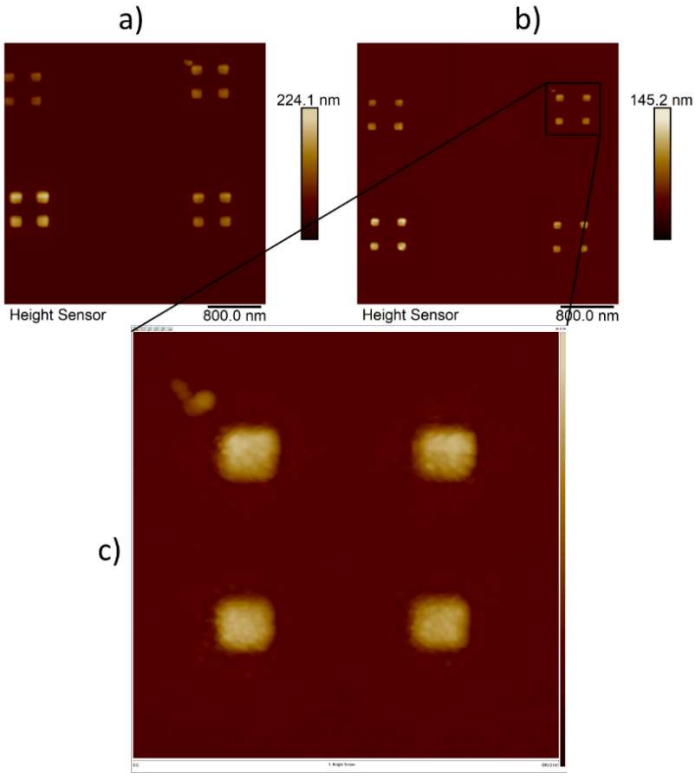

*Figure 49: AFM images of FEBID gold pads to detect methylene blue. **a)** Structure as deposited by parallel patterning. **b)** Gold pads after purification. **c)** Zoom on the relevant array area from which the SERS signal in Figure 50 originates.*

In Figure 49, these pads are shown as directly deposit (a), after purification (b), and zoomed in on the area from which the spectrum was recorded (c) in Figure 50. In this graph you can see both the spectrum coming from the FEBID structures and the spectrum coming from the surrounding substrate. It is immediately obvious that the signal from the pads is about three times stronger, indicating signal enhancement on the FEBID gold pads.

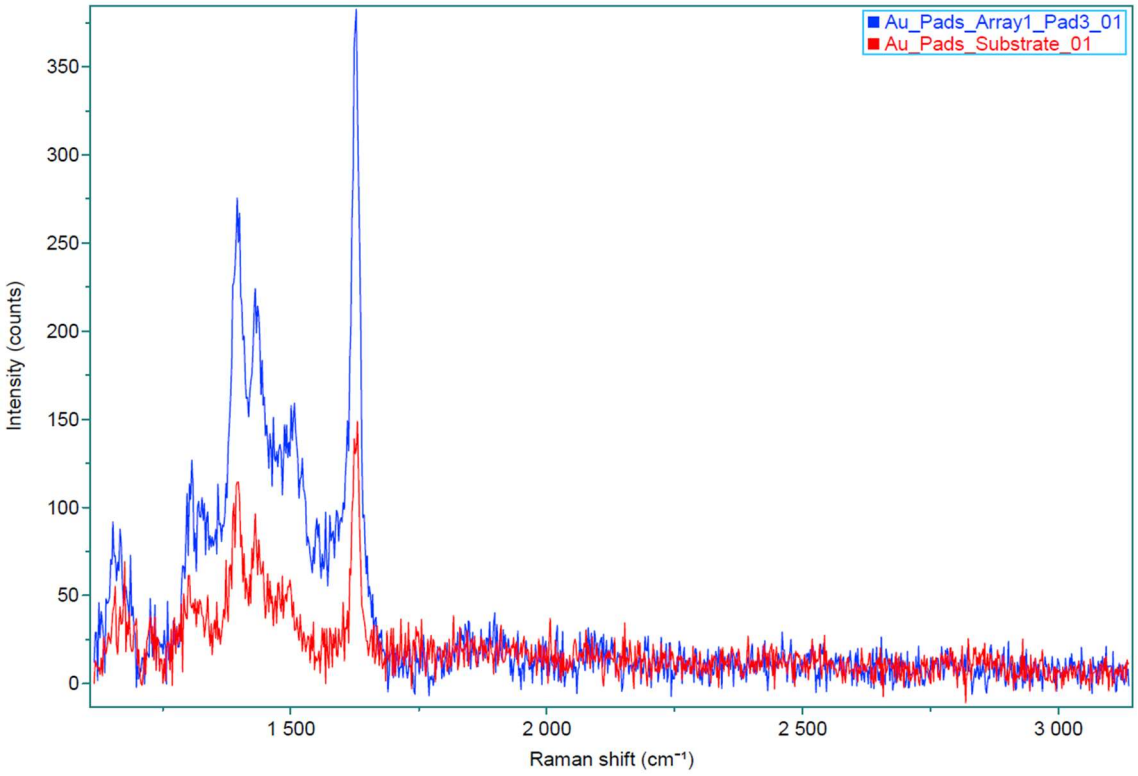

*Figure 50: Spectra of methylene blue. **Blue**: Sers signal of the molecule originating from the FEBID gold structures on the sample. **Red**: Signal of a thicker layer of the molecule on the substrate with no amplification.*

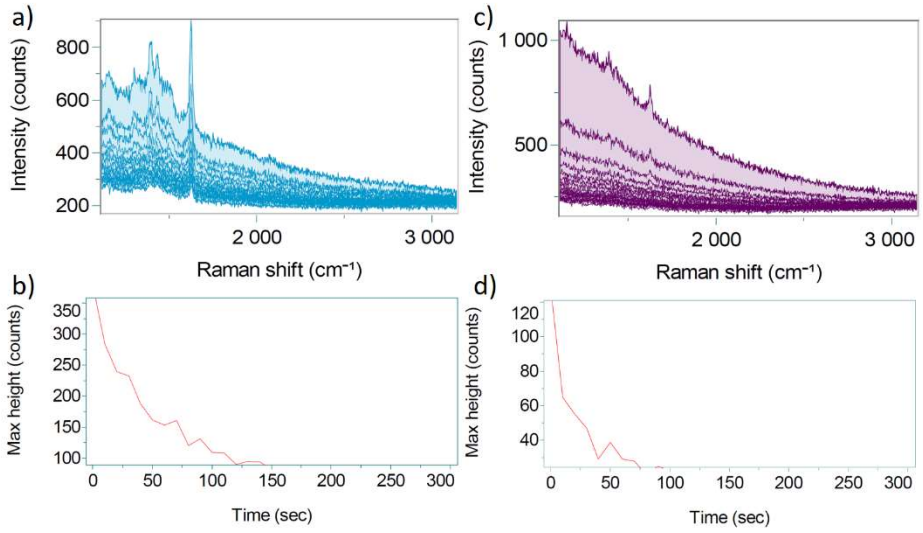

*Figure 51: Time-resolved spectra of methylene blue. **a)** Spectra from the FEBID gold pads. **b)** Slow decrease of signal intensity as a function of measurement time on the FEBID pads. **c)** Spectra from the surrounding substrate. **d)** Rapid drop in signal intensity as a function of measurement time on the substrate.*

Another indication of the enhancement on the gold pads is the temporal decrease of the signal intensity depending on whether a time-resolved measurement is performed on the FEBID structures or on the substrate (Figure 51). The methylene blue layer can be detected everywhere on the wafer (c), but due to the decrease of the signal pad vs. substrate, it can be assumed that there is a SERS enhancement (a), as the signal on the FEBID structures declines differently (b). This is because the SERS-signal is a convolution of the regular signal of the thick methylene blue layer, which is also measured next to the structures, and the enhanced signal form the first couple of molecule layers on the FEBID structure. This also shows that the structures cannot be completely covered with carbon, otherwise there would be no enhancement and at least part of the gold grains must be free.

4.4.2 Proof of Presence of 4-MBT

The detection of 4-MBT has already proven difficult in 4.3.2 for FEBID pads. For methylene blue, detection has been shown to be possible despite carbon contamination and should theoretically be possible for other molecules as well. After the “small” pads were successful, they are now also used for the detection of 4-MBT. In order to be able to pick up an evaluable SERS signal, a monolayer of 4-MBT must be formed (2.3.2) and for this, it is necessary for a part of the gold grains to be carbon-free, as otherwise no chemical bonding is possible. The gold pads that successfully detected 4-MBT are shown in Figure 52 and were purified with are 5 keV accelerating voltage, 5.6 nA beam current, 1 µs DT, 10 nm PoP, 30 Pa H_2O atmosphere at room temperature and a dose of 45 C.cm^{-2}. The corresponding Raman spectrum can be seen in Figure 53. The calculation of the enhancement factors was carried out according to 2.3.2 with the following values: I_{SERS}(1595 cm^{-1}) = 224, I_{SERS}(1078 cm^{-1}) = 209, c_{ref} = 0.5 M, μ_S = 5.3 nm^{-2}, H_{eff} = 19 µm, $A = 0.63$ and I_{Ref}(1595 cm^{-1}) = 4070, I_{Ref}(1078 cm^{-1}) = 1100.
This results in a value of **2.5*10² for the EF**, which compared to a gold sputter sample, which is always produced as a reference, with an enhancement factor of **10^5**, which makes a difference of a factor of 400 in a direct comparison without including the area difference of the signal contribution.
Together with the spectrum in Figure 53, this result is promising for several reasons. On the one hand, it was possible to detect 4-MBT to a usable extent and to determine the EF. At the same time, it proves beyond doubt that the gold grains of the pad are partially exposed and not covered by a carbon layer, otherwise no binding would have occurred and detection would not have been possible. Even if the difference to a gold sputter sample is very high, it is nothing less than a proof-of-concept and shows that FEBID structures are suitable as substrates for SERS measurements. The reason for the difference between the samples will be resolved in the next chapter.

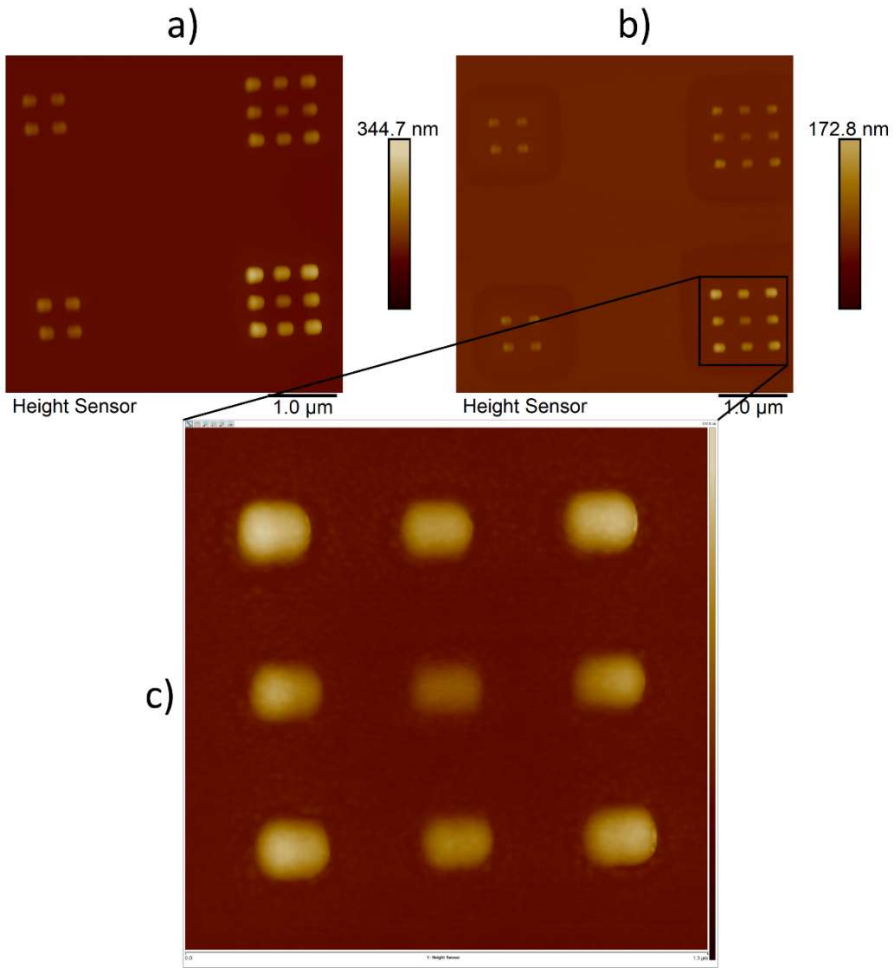

Figure 52: AFM images of FEBID gold pads to detect 4-MBT. ***a)*** *Structure as deposited by parallel patterning.* ***b)*** *Gold pads after purification.* ***c)*** *Zoom on the relevant array area from which the SERS signal in Figure 53 originates.*

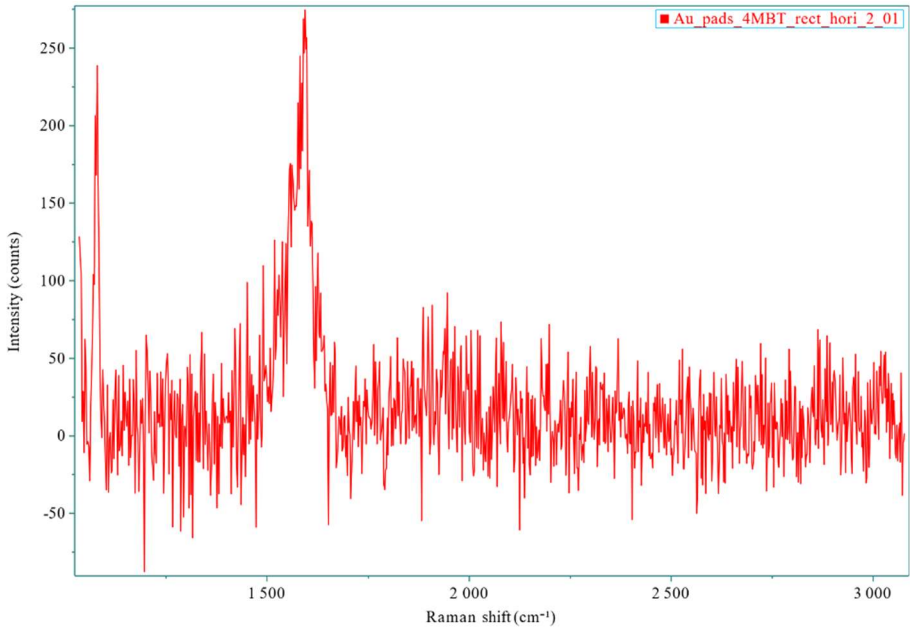

Figure 53: SERS signal of 4-MBT originating from FEBID gold pads. The signal enhancement is about 400 times weaker compared to a gold sputter sample, but still shows the principal possibility of building plasmonically active nanostructures suitable for SERS.

4.4.3 Powerful FEBID Gold Pads

In the previous chapter, it was shown that the carbon contamination plays a significant role in the signal degradation of the FEBID samples and in the work of Kuhness et al.[44] the carbon layer was directly detected by TEM examination. However, it could also be shown that the entire structure cannot be covered and that there must therefore be other reasons for the low signal yield. Since neither deposition nor purification are processes that take place in thermodynamic equilibrium, and gold in particular has a certain known mobility in terms of morphological changes, it was decided to let the samples rest in a desiccator for 20 days. The FEBID samples are the same pads that were already used in 4.3.2 and could not detect 4-MBT there. After removing the samples from the desiccator and examining them in the AFM, a drastic morphological change was observed. The individual states of the gold pads can be seen in Figure 54 and as a 3D representation in Figure 55.

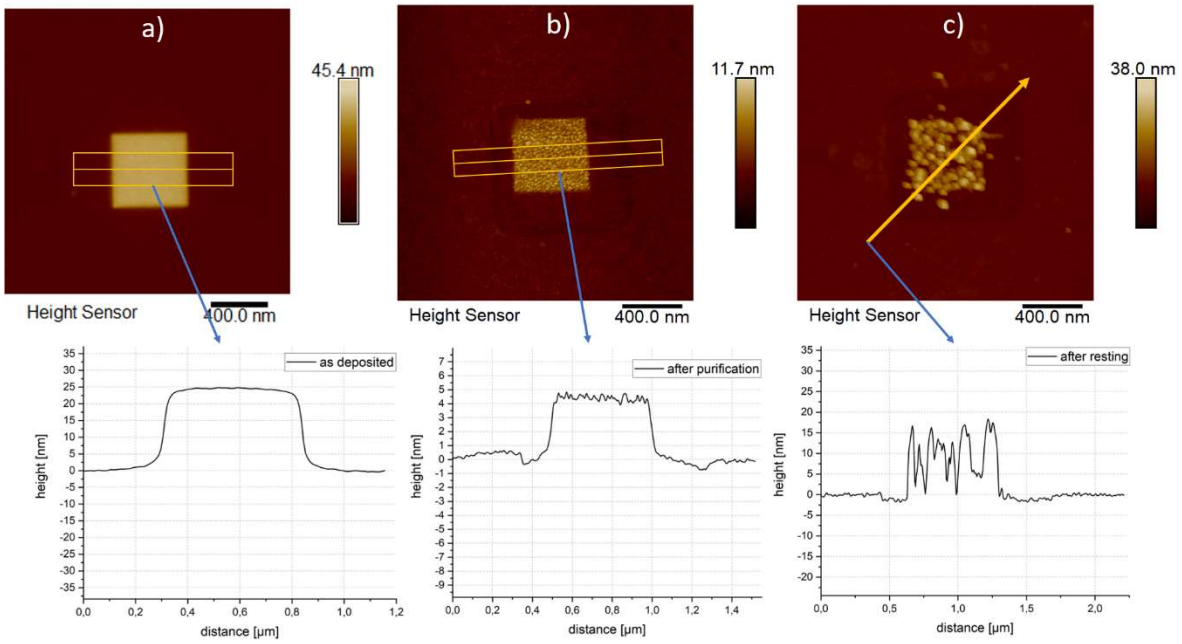

Figure 54: AFM images of "large" FEBID gold pads. Their corresponding cross sections after the various processing steps, between the end of purification and after a waiting period of 20 days there is a dramatic increase in the roughness and agglomeration of the gold islands. ***a)*** *As deposited.* ***b)*** *After purification.* ***c)*** *After 20 days of resting in the desiccator.*

Resting has led to an agglomeration of the gold islands within the FEBID pads and thus also increased their roughness (c), which in turn is similar to the morphology of gold sputter samples. A comparison of these pads and a gold sputter sample can be seen in Figure 58. The determination of the grain sizes (small single isolated grains) resulted in values of 12 to 19 nm in diameter for the FEBID sample and values of 21 to 28 nm for the sputter sample. The grain sizes of both samples are therefore similar. Since the hoped-for surface morphological change occurred, the FEBID samples were again immersed in a 10^{-4} molar solution of 4-MBT for 1 hour and then air dried. In fact, a strong SERS signal was measured for the pad with a purification dose of 50 $C.cm^{-2}$ in the subsequent Raman measurement. In Figure 56 this measurement can be seen for the mentioned sample location. The red area is the already known measurement from 4.3.2 (Figure 40) where no plasmonic response was obtained and the blue spectrum is now the SERS signal from 4-MBT after the resting transition.

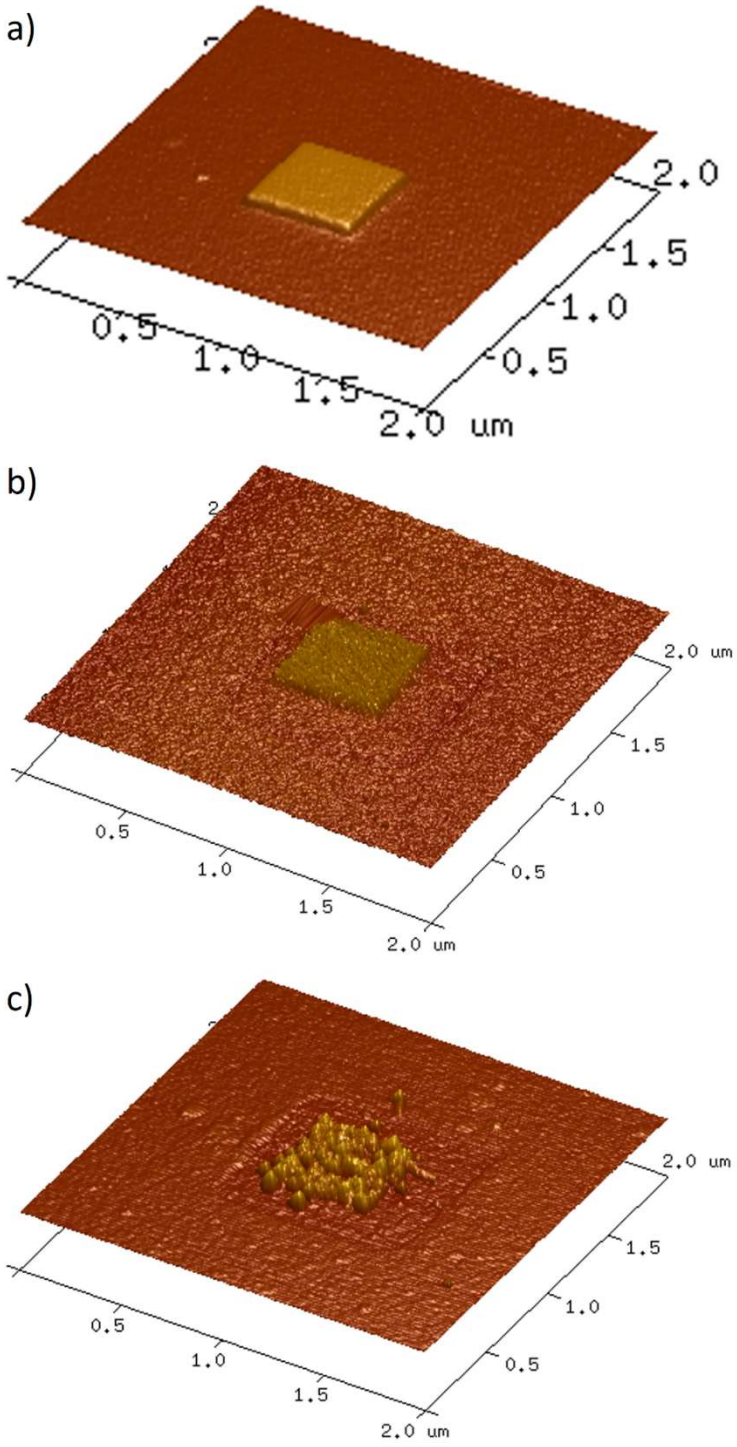

Figure 55: AFM 3D representation of the FEBID gold pads in Figure 54. ***a)*** *As deposited.* ***b)*** *After purification.* ***c)*** *After 20 days of resting in the desiccator.*

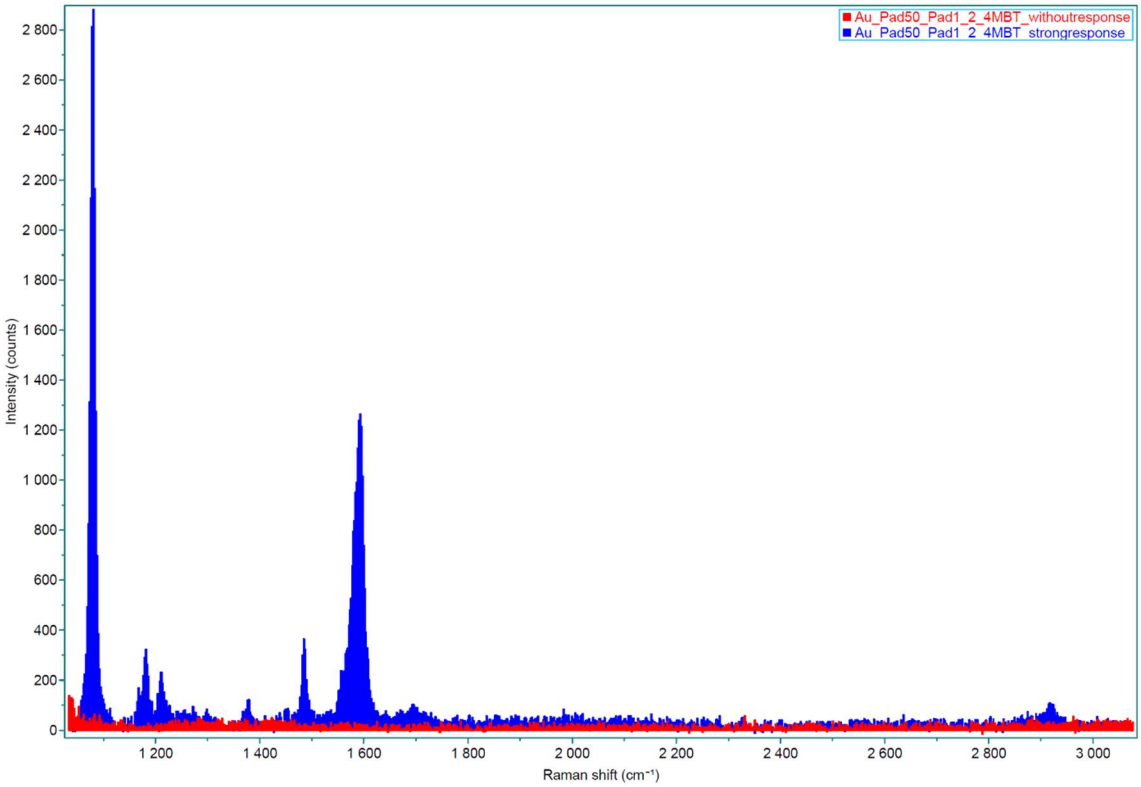

*Figure 56: Raman spectra of 4-MBT on "large" FEBID gold pads with a purification dose of 50 C.cm^{-2}. **Red curve**: Raman spectra of a FEBID gold without any amplification of 4-MBT. **Blue curve**: Raman spectra of the same pad after 20 days of sample resting now with a strong 4-MBT fingerprint.*

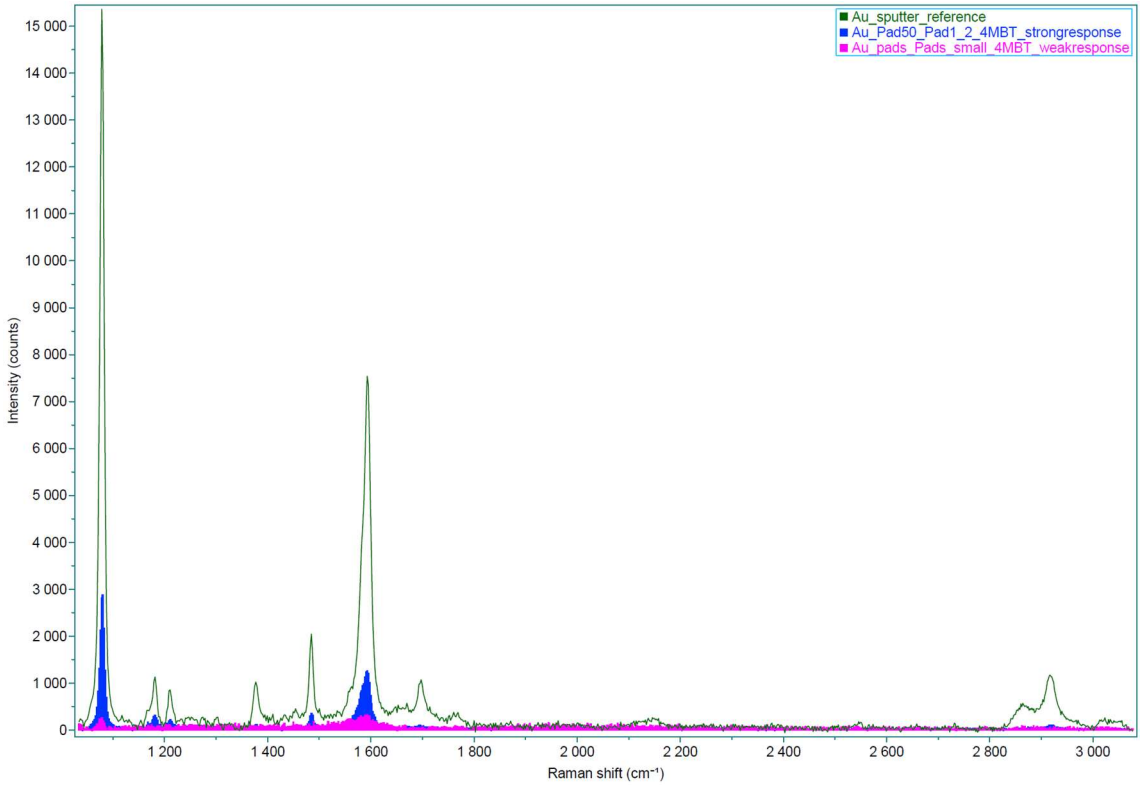

Figure 57: Comparison spectrum of 4-MBT on "large" FEBID gold pads with a purification dose of 50 C.cm^{-2} and the gold sputter sample. Green curve: sputter sample. Blue curve: Raman spectra of the FEBID gold pad after 20 days of sample resting. Magenta curve: "Small" pad with weak signal amplification from 4.4.2.

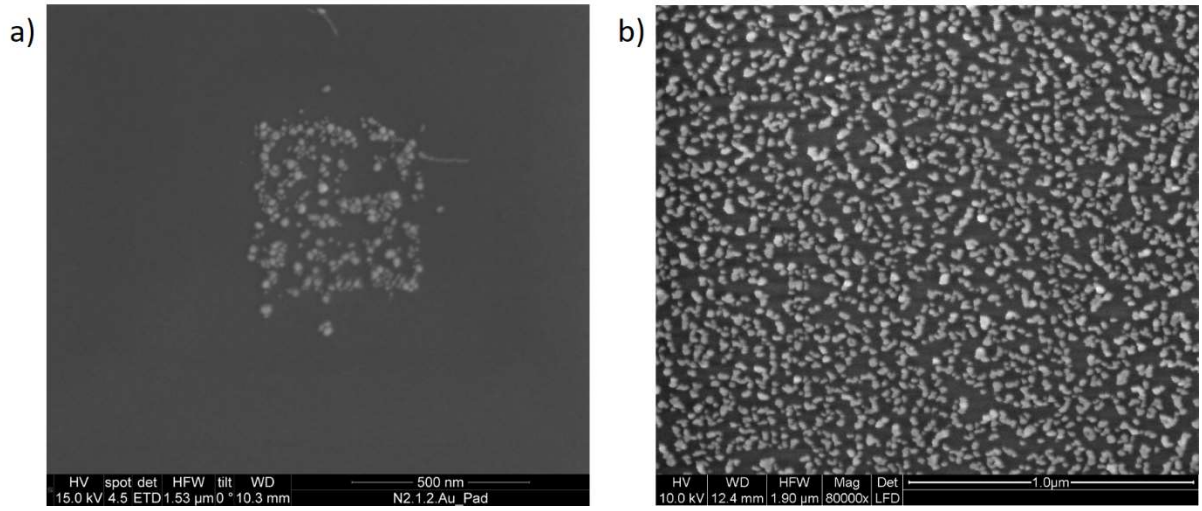

Figure 58: SEM images of gold on a silicon wafer. ***a)*** *FEBID gold pad after a resting period of 2 months.* ***b)*** *Nominally ~2 nm thick gold sputter layer.*[30]

For comparison, the reference spectrum of the sputter sample is plotted in Figure 57 (green), the successful measurements of the "large" pads (blue) and the known proof-of-concept measurement with the "small" pads from 4.4.2 (magenta). In this spectrum it can be clearly seen that the signal strength between the high yield "large" pads and the reference sputter probe differs by a factor of 5 in signal strength. However, it should be noted that the area ratio, so the area that contributes to the signal in both spectra, is 1.15 for the sputter sample and 0.19 for the FEBID sample. This means that the signal of the FEBID sample only comes from about one sixth of the area of the sputter sample and should therefore even be slightly better in a direct comparison.

The calculation of the enhancement factor with the values I_{SERS}(1595 cm^{-1}) = 1242, I_{SERS}(1078 cm^{-1}) = 1888, $A = 0.19$ and I_{Ref}(1595 cm^{-1}) = 164, I_{Ref}(1078 cm^{-1}) = 382 results in a value **1.2*10^5 for the EF** which is sensational and corresponds to the values of comparable sputter samples (**10^5**). It should be noted at this point that there was a measurement error in the determination of the reference values for ethanol, which resulted in a much lower intensity. Thus, the value calculated above does not correspond to the true EF value of the FEBID gold pad, but since the ethanol value also applies to the sputter sample, the relative values to each other remain correct, which can be confirmed by the spectra alone. Since the original assumption was that the carbon was the main cause of the low signal strength, this approach needs to be reconsidered and more attention given to the surface morphology of the samples in terms of their transformation. Carbon contamination does not play an insignificant role, as it has been detected several times and represents an additional overlay to the morphologic issues.

Despite all the problems and uncertainties, it could be proven that a FEBID gold structure is comparable to a gold sputter sample in terms of signal enhancement properties. The reproducibility of these results is a great challenge, since comparable results were only accomplished with a few pads, but the basic goal of this work was obtained. Adding a quasi-imaging component to this process is briefly explained in the last section of the results.

4.4.4 Raman Mapping of Plasmonic Activity

None of the FEBID gold pads in this thesis, whether "small" or "large" or "intermediate", are so huge that they can be seen with a light microscope. In order to find them again, the pads were always deposited in the middle of FIB frames, as mentioned several times in this work. Even here, however, it can only be guessed where they actually are. One way to visualise a plasmonic active pad is to detect the SERS signal of a molecule with the mapping function of the Raman microscope, as shown in Figure 59.

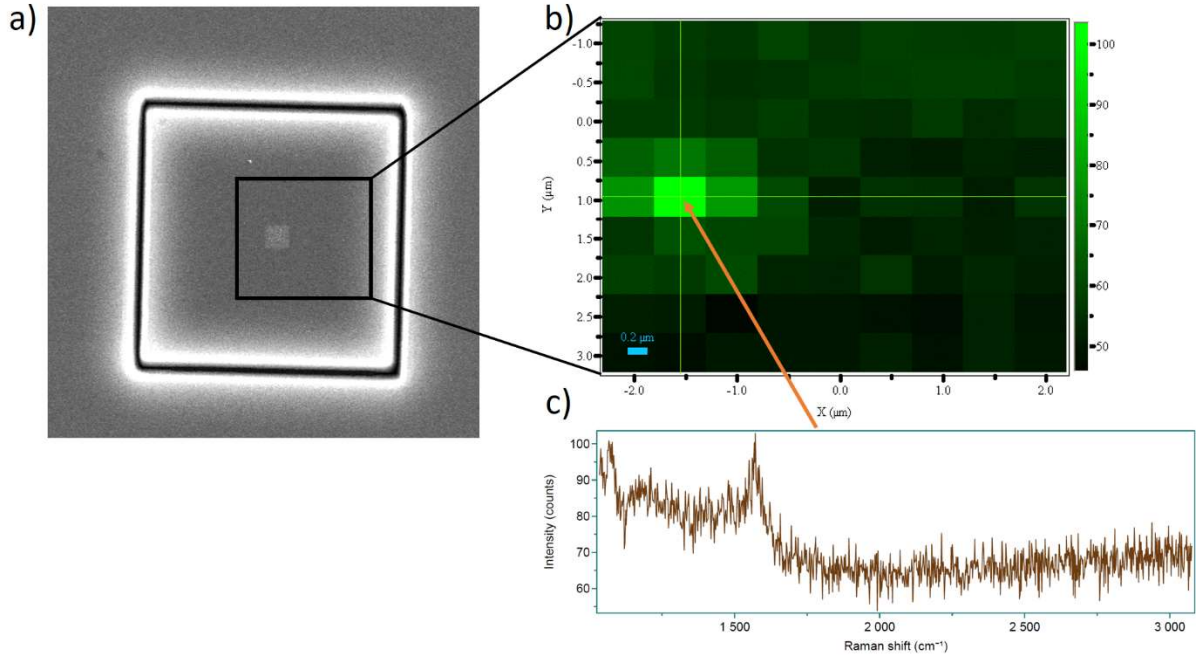

Figure 59: Raman mapping of a plasmonically active FEBID gold pad. ***a)*** *SEM image of the FIB marker and the faintly visible pad in the middle, above a black frame indicating the measurement range of the mapping.* ***b)*** *The mapping associated with the measurement range with the pad as a light green area.* ***c)*** *The corresponding spectrum from the marked area (orange arrow), which shows a clear signal of 4-MBT. Please note that the spectrum has a lower intensity due to other recording parameters and the area in the mapping is larger than the actual pad, as the laser has a diameter of 1 µm and overlaps occur.*

In the process, the laser moves over a predefined sample area (a) in a grid and records individual point spectra. The area of interest in the spectrum can be narrowed down and its intensity displayed as a coloured map (b).
With this method, the plasmonically active structure can be well distinguished from the surrounding substrate and the information obtained can be combined with SEM or light microscope images. Depending on the acquisition parameters, the signal strength can also vary, which leads to a longer mapping time with a longer acquisition time, but to an even better differentiation from the background. It would also be possible, for example, to examine several FEBID structures with the same or different geometries/morphologies for their plasmonic response and to directly recognise the position and intensity in relation to each other, through the visual feedback of the mapping.

5 Summary and Outlook

The motivation of this master thesis was the controlled fabrication of functional 2.5D nano-substrates for application as Surface Enhanced Raman Spectroscopy (SERS) substrate. For that, the additive, direct-write manufacturing technology Focused Electron Beam Induced Deposition (FEBID) was used for initial fabrication, as this technology allows site-specific fabrication of nano-structures in a single step. As FEBID materials notoriously suffer from high carbon contents, a post-growth purification step was applied, to transfer the nanostructures into pure Au materials. Such SERS elements were then evaluated on their plasmonic activity via Raman spectroscopy and iteratively improved to understand the performance limiting influences during fabrication and purification. The overriding question was, whether this new approach can compete with the traditional SERS fabrication method of gold sputtering.

In more detail, Si wafers with a 4 nm thick oxide layer on top were used throughout the study but always treated in two different ways. For FEBID structures, differently sized square deposits were fabricated from the gold precursor Me_2-Au(acac). In a second step, we applied e-beam scanning in low pressure H_2O atmospheres (80 Pa, room temperature) to remove the unwanted carbon. As reference, nominally 4 nm thick gold sputter layers were prepared via sputtering. Both substrate types were then modified by Raman active test analytes for plasmonic evaluation and mutual comparison.

In a first step, we investigated, which deposition FEBID parameters yield satisfactory and reproducible nanostructures in terms of geometry and morphology. For that, “small” FEBID gold pads (100 nm lateral size) were first deposited in larger arrays for improved SERS statistics. However, a bowl shape distribution of pad heights within the array was found, which could be traced back to surface diffusive effects, triggered by the growing pads, acting as morphological barrier. As a systematic adaption and full optimization did not give satisfactory results, the overall design was changed from small-pad-arrays to large-single-pads with footprints of 1×1 μm^2 and very homogeneous heights across the pads, as required.

In the second part, the high carbon content of more than 90 at.% after initial FEBID fabrication had to be removed. We here followed the purification approach of Geier et al.[7], where carbon is etched out with a high efficiency. Although chemical, morphological and volumetric evaluation were in agreement with previous literature, no clear plasmonic activity could be detected. A closer look on the situation revealed, that aside of overall purity, surface contamination plays an essential role. Although small in volume and thickness, such carbon layers supressed the plasmonic activity, as confirmed by purification-like treatments of sputtered high-performance substrates. Systematic studies on the purification process revealed optimum doses, where plasmonic activities could finally be detected. The performance, however, was comparable low as enhancement factors ranged around $\mathbf{10^2}$, being almost 400 times weaker than for sputtered SERS substrates. In a final step, we allowed fully purified FEBID pads to “relax” as both, initial fabrication and purification, are processes far from equilibrium. The results after 3 weeks storage in dark ambient conditions were indeed remarkable. First, the morphology changed into agglomerated structures but remained within the original footprint. Second, and even more important for this thesis, the enhancement factors of such annealed sample increased to $\mathbf{10^5}$, now being comparable to those of traditional gold sputter SERS substrates.

In conclusion, this study has demonstrated, that FEBID can be used for fabrication of SERS-like substrates. However, the current route is much more complicated than simple Au sputtering, as it requires post-growth purification to remove the unwanted carbon and an

additional annealing period in ambient conditions to reach a thermodynamic equilibrium. Consequently, this work has to be understood as proof-of-principle and starting point for further studies to optimize both processes, fabrication and purification. This is indeed important as this approach contains huge potential due to the fact, that FEBID allows fabrication on a wide range of materials (vacuum & e-beam compatible) on practically any given surface morphology (accessibility by the e-beam) with the advantages of *site specific fabrication* and *fully flexible footprint sizes / shapes*. Possibilities, classical sputtering cannot provide per concept.

References

1. Thomas, S., Thomas, R., Zachariah, A. K. & Mishra, R. K. *Spectroscopic Methods for Nanomaterials Characterization*. *Spectroscopic Methods for Nanomaterials Characterization* vol. 2 (2017).

2. Larkin, P. *Infrared and Raman Spectroscopy; Principles and Spectral Interpretation*. *Infrared and Raman Spectroscopy; Principles and Spectral Interpretation* (2011). doi:10.1016/C2010-0-68479-3.

3. Hellerer, T. CARS-Mikroskopie : Entwicklung und Anwendung. *Dissertation* (2004).

4. Ru, E. C. Le, E. Blackie, Meyer, M. & Etchegoin, P. G. SSEF.pdf. *J. Phys. Chem. C* **111**, 13794 (2007).

5. Falthansl-Scheinecker, P. Approaching Fundamental Resolution Limits of Focused Electron Beam Induced Deposition During the Fabrication of Gold Nanostructures for Terahertz Plasmonics. (2018).

6. Winkler, R. *et al.* Direct-Write 3D Nanoprinting of Plasmonic Structures. *ACS Appl. Mater. Interfaces* **9**, 8233–8240 (2017).

7. Geier, B. Rapid and Highly Compact Purification at Room Temperature for Focused Electron Beam Induced Pt-C Deposits. (2014).

8. Young, R. J. & Moore, M. V. Dual-Beam (FIB-SEM) Systems. in *Introduction to Focused Ion Beams* (2005). doi:10.1007/0-387-23313-x_12.

9. Goldstein, J. I. *et al. Scanning electron microscopy and x-ray microanalysis*. *Scanning Electron Microscopy and X-ray Microanalysis* (2017). doi:10.1007/978-1-4939-6676-9.

10. FEI. xT Nova NanoLab User s Manual. *Interface* (2004).

11. GETec. AFSEM. https://www.getec-afm.com/.

12. Courtesy of Dr. Harald Plank, Institute for Electron Microscopy and Nanoanalysis, Graz University of Technology, Austria, 2021.

13. Winkler, R. Implications of Precursor Dynamics on Nanostructures during Focused Electron Beam Induced Deposition. (2013).

14. Huth, M. *et al.* Focused electron beam induced deposition: A perspective. *Beilstein J. Nanotechnol.* **3**, 597–619 (2012).

15. Engmann, S. *et al.* Absolute cross sections for dissociative electron attachment and dissociative ionization of cobalt tricarbonyl nitrosyl in the energy range from 0 eV to 140 eV. *J. Chem. Phys.* **138**, 0–7 (2013).

16. Botman, A., Mulders, J. J. L. & Hagen, C. W. Creating pure nanostructures from electron-beam-induced deposition using purification techniques: A technology perspective. *Nanotechnology* **20**, (2009).

17. Radeschnig, U. Approaching Fundamental Resolution Limits during Focused Electron Beam Induced Gold Deposition on Bulk Substrates. (2017).

18. Winkler, R. *et al.* Toward ultraflat surface morphologies during focused electron beam

induced nanosynthesis: Disruption origins and compensation. *ACS Appl. Mater. Interfaces* **7**, 3289–3297 (2015).

19. Geier, B. *et al.* Rapid and highly compact purification for focused electron beam induced deposits: A low temperature approach using electron stimulated H2O reactions. *J. Phys. Chem. C* **118**, 14009–14016 (2014).

20. Warneke, Z., Rohdenburg, M., Warneke, J., Kopyra, J. & Swiderek, P. Electron-driven and thermal chemistry during water-assisted purification of platinum nanomaterials generated by electron beam induced deposition. *Beilstein J. Nanotechnol.* **9**, (2018).

21. García, R. *Amplitude Modulation Atomic Force Microscopy*. *Amplitude Modulation Atomic Force Microscopy* (2010). doi:10.1002/9783527632183.

22. Splinter, R. Action potential transmission and volume conduction. *Handb. Phys. Med. Biol.* **56**, 5-1-5–9 (2010).

23. Horiba. User Manual HR 800 Horiba. 1–42 (2014).

24. Horiba. What is confocal Raman microscopy? https://www.horiba.com/de/scientific/products/raman-spectroscopy/raman-academy/raman-faqs/what-is-confocal-raman-microscopy/.

25. Bruker. Confocal Raman Microscopy. https://www.bruker.com/products/infrared-near-infrared-and-raman-spectroscopy/raman/confocal-raman.html.

26. Schmid, T. & Dariz, P. Setup_Raman_Spectroscopy. *Wikipedia* https://commons.wikimedia.org/wiki/File:Setup_Raman_Spectroscopy_adapted_from_Thomas_Schmid_and_Petra_Dariz_in_Heritage_2(2)_(2019)_1662-1683.png#file.

27. Raman scattering, CC BY-SA 3.0. https://commons.wikimedia.org/w/index.php?curid=2772554.

28. Paar, A. Grundlagen der Raman Spektroskopie. https://wiki.anton-paar.com/at-de/grundlagen-der-raman-spektroskopie/.

29. Schlücker, S. Oberflächenverstärkte Raman-Spektroskopie: Konzepte und chemische Anwendungen. *Angew. Chemie* **126**, 4852–4894 (2014).

30. Fitzek, H. A new simulation method for Surface-Enhanced Raman Spectroscopy applicable to rough and highly irregular substrates. (2018).

31. Love, J. C., Estroff, L. A., Kriebel, J. K., Nuzzo, R. G. & Whitesides, G. M. *Self-assembled monolayers of thiolates on metals as a form of nanotechnology*. *Chemical Reviews* vol. 105 (2005).

32. Shun'ko, E. V. & Belkin, V. S. Cleaning properties of atomic oxygen excited to metastable state 2 s2 2 p4 (S1 0). *J. Appl. Phys.* **102**, (2007).

33. Plank, H., Haber, T., Gspan, C., Kothleitner, G. & Hofer, F. Chemical tuning of PtC nanostructures fabricated via focused electron beam induced deposition. *Nanotechnology* **24**, (2013).

34. Plank, H. *et al.* Electron-beam-assisted oxygen purification at low temperatures for electron-beam-induced Pt deposits: Towards pure and high-fidelity nanostructures. *ACS Appl. Mater. Interfaces* **6**, 1018–1024 (2014).

35. Sharma, B., Frontiera, R. R., Henry, A. I., Ringe, E. & Van Duyne, R. P. SERS: Materials, applications, and the future. *Mater. Today* **15**, 16–25 (2012).

36. Amendola, V., Bakr, O. M. & Stellacci, F. A study of the surface plasmon resonance of silver nanoparticles by the discrete dipole approximation method: Effect of shape, size, structure, and assembly. *Plasmonics* **5**, 85–97 (2010).

37. Sun, X. & Li, H. Gold nanoisland arrays by repeated deposition and post-deposition annealing for surface-enhanced Raman spectroscopy. *Nanotechnology* **24**, (2013).

38. Song, X. *et al.* Density functional theory study of NEXAFS spectra of 4-methylbenzenethiol molecule. *Chem. Phys. Lett.* **645**, 164–168 (2016).

39. Seo, K. & Borguet, E. Potential-induced structural change in a self-assembled monolayer of 4-methylbenzenethiol on Au(111). *J. Phys. Chem. C* **111**, 6335–6342 (2007).

40. Ikeda, K., Suzuki, S. & Uosaki, K. Enhancement of SERS background through charge transfer resonances on single crystal gold surfaces of various orientations. *J. Am. Chem. Soc.* **135**, 17387–17392 (2013).

41. Fitzek, H. Accurate Near-Field Simulations of the Real Substrate Geometry□A.pdf.

42. Camargo, P. H. C., Au, L., Rycenga, M., Li, W. & Xia, Y. Measuring the SERS enhancement factors of dimers with different structures constructed from silver nanocubes. *Chem. Phys. Lett.* **484**, 304–308 (2010).

43. Rycenga, M. *et al.* Surface-enhanced raman scattering: comparison of three different molecules on single-crystal nanocubes and nanospheres of silver. *J. Phys. Chem. A* **113**, 3932–3939 (2009).

44. Kuhness, D. *et al.* High-Fidelity 3D-Nanoprinting of Plasmonic Gold Nano-Antennas. *ACS Appl. Mater. Interfaces* **submitted**, (2020).

45. Hirt, L., Reiser, A., Spolenak, R. & Zambelli, T. Additive Manufacturing of Metal Structures at the Micrometer Scale. *Advanced Materials* vol. 29 (2017).